MECHANISMS OF THE $^{64}Zn(d,^{6}Li)^{60}Ni$ REACTION AT E_{lab} = 16.4 MeV

by

James E. Bowsher

A dissertation submitted to the faculty of the University of North Carolina in partial fulfillment of the requirements for the degree of Doctor of Philosophy in the Department of Physics and Astronomy.

Chapel Hill

1989

Approved by :

Thomas B. Clegg Advisor

W. J. Thompson Reader

Julius Wenneff Reader

Abstract

JAMES E. BOWSHER. Mechanisms of the $^{64}Zn(d,^{6}Li)^{60}Ni$ Reaction at E_{lab} = 16.4 MeV. (Under the direction of Thomas B. Clegg.)

Cross-sections, A_y, A_{yy}, and A_{xx} for the $^{64}Zn(d,^{6}Li)$ reaction forming the ground and first excited states of ^{60}Ni were measured in 5° steps from θ_{lab} = 25° to 80° using an E_{lab} = 16.4 MeV beam of vector and tensor polarized deuterons. These data include the first measurement of A_{xx} and A_{yy} for the $(d,^{6}Li)$ reaction on a medium to heavy target nucleus. The A_y measurement is also among the first for $(d,^{6}Li)$ reactions. Also measured were excitation functions of $d\sigma/d\Omega$ for the $(d,^{6}Li)$ reactions on ^{36}Ar, ^{40}Ca, and ^{64}Zn and angular distributions of $d\sigma/d\Omega$ for $^{60}Ni(^{6}Li,^{6}Li)$ scattering at E_{lab} = 14.8 MeV and of $d\sigma/d\Omega$, A_y, A_{yy}, and A_{xx} for $^{64}Zn(d,d)$ scattering at E_{lab} = 16.4 MeV.

The ^{6}Li ground state and seven other wave functions, each representing ^{6}Li continuum states of a given spin, I, and internal orbital angular momentum, l, $l \leq 2$, were included in coupled-channels (CC) calculations of $^{60}Ni(^{6}Li,^{6}Li)$ elastic scattering and finite-range, coupled-channel Born approximation (CCBA) calculations for the $^{64}Zn(d,^{6}Li)$ reaction forming the ^{60}Ni ground state. This analysis is the first to consider the influence of ^{6}Li continuum states on the $(d,^{6}Li)$ reaction. The ^{6}Li-^{60}Ni interactions were generated using a cluster folding model. Both the folding model and the CC and CCBA calculations were performed by the code FRESCO. [Tho88]

For the $^{64}Zn(d,^{6}Li)$ reaction, CCBA calculations demonstrated that α transfers forming the 3^+ state of ^{6}Li affect $d\sigma/d\Omega$ and A_y very strongly. However, the calculations predicted predominantly positive values of A_y, whereas the measured values of A_y are predominantly negative. To a lesser degree, transfers forming the other ^{6}Li continuum states also influenced the predicted $(d,^{6}Li)$ cross-sections and analyzing powers.

Acknowledgments

To three professors, I wish to express special thanks; to Drs. Tom Clegg and Ed Ludwig for teaching the basics, guiding my research, working the experiments, and reading numerous drafts of this dissertation; and to Dr. Jeff Tostevin for his considerable contributions to the basic ideas underlying our analysis of the (d,^{6}Li) reaction and for his guidance throughout and efforts on behalf of that analysis. I am also much indebted to Dr. Hugon Karwowski for the criticisms and suggestions as well as the long hours he contributed to the (d,^{6}Li) measurements and to Dr. Bill Thompson for reading this dissertation and for the knowledgeable and indispensable advice he has provided on many crucial decisions concerning this project. To Dr. Chandra Bhat, I am grateful for his hard work on the (d,^{6}Li) experiments and for many helpful suggestions and discussions. I thank Dr. Heinz Clement, who has been visiting for only a couple of months, for reading this dissertation and for the interest he has shown and the insights he has provided regarding this project. I have also enjoyed the opportunity to work with Drs. Bennett Karp, David Kopf, and Mark Schneider.

I greatly appreciate the friendship and generous assistance that many of my fellow graduate students have provided. I am particularly grateful to David Abbott, Roy Fauber, Tim Mooney, Ken Nash, and Tom Spencer for the hours and the ideas they contributed to the (d,^{6}Li) experiments.

I gratefully acknowledge the indispensable role that the nuclear reaction code FRESCO played in this project, and I thank its author, Dr. Ian Thompson, for the modifications he installed and the checks he performed on our behalf. His assistance was always prompt and generous. Thanks to Drs. Ana Eiro and Ian Thompson and particular thanks to Dr. Robert Varner for their help in installing FRESCO at TUNL.

Paul Carter, Sidney Edwards, Pat Mulky, Bob Rummel, and Chris Westerfeldt deserve much credit for their success in keeping the lab running and in accommodating the needs of a diversity of research projects. The efforts of Mr. Mark Boyd, Dr. Chris Gould, and Dr. Russel Roberson are also gratefully acknowledged. I appreciate the support given this project by Dr. Ed Bilpuch. I thank Dr. Eugen Merzbacher and the University of Surrey for supporting my visit to that institution, and I appreciate the hospitality of Jeff and Lena Tostevin and other members of the physics department at Surrey.

Funding for this project was provided in part by the Department of Energy.

Finally, I dedicate this thesis to my parents, Fred and Juanita Bowsher, and to my sisters, Jenny and Janet, and thank them for the support they have provided over many years.

TABLE OF CONTENTS

LIST OF TABLES

LIST OF FIGURES

Chapter 1

Introduction

1.1 Studies of the (d,^{6}Li) Reaction

The (d,^{6}Li) reaction has been investigated extensively, primarily by cross-section measurements utilizing a wide range of targets and incident beam energies and by one-step, distorted-wave Born approximation (DWBA) analyses of these data. These analyses have often focussed on extracting target α-particle spectroscopic factors from the data. [Coo84, Ume84, Jan80, Ful79, Chu78] Other studies have examined the dependence of DWBA calculations on optical model parameters and on the interactions and wave functions describing the bound states of ^{6}Li and the target. [Coo84, Coo83, Jan80] Multistep analyses of the (d,^{6}Li) reaction have been few in number. Palla and Oelert [Pal84] utilized the coupled reaction channels formalism to study the effects of couplings to excited states of the target and the residual nucleus for the ^{24,26}Mg(d,^{6}Li)^{20,22}Ne reactions at E_d = 80 MeV. To our knowledge, no previous analyses of the (d,^{6}Li) reaction have considered excited states of the ^{6}Li nucleus.

Some ($\vec{d}$,^{6}Li) data, acquired utilizing polarized beams, also exist. Cross-sections and vector analyzing powers (VAPs) have been measured for ^{24}Mg,^{40}Ca($\vec{d}$,^{6}Li) at E_d = 45.5 MeV [Jac79] and for ^{12}C,^{16}O($\vec{d}$,^{6}Li) at E_d = 51.7 MeV [Yam85a,Yam85b]. Data for the ^{24}Mg,^{40}Ca($\vec{d}$,^{6}Li) reactions to the ground states of ^{20}Ne and ^{36}Ar were fairly well reproduced by one-step, zero-range, DWBA calculations. One-step, finite-range, DWBA calculations provided excellent reproductions of the ^{12}C,^{16}O($\vec{d}$,^{6}Li)^{8}Be(gs),^{12}C(gs) data. Hence, one-step analyses of ($\vec{d}$,^{6}Li) data acquired at $E_d \approx 45$ - 50 MeV have shown no

evidence of (but do not exclude the possibility of) multistep processes in (d,^{6}Li) reactions forming the ground states of residual nuclei.

Cross-sections, VAPs, and all three tensor analyzing powers (TAPs) have been measured for $^{16}O(\vec{d},^6Li)$ at E_d = 22 MeV and for $^{12}C(\vec{d},^6Li)$ at E_d = 18 and 22 MeV. Some of the cross-section and VAP angular distributions were fairly well reproduced by one-step, finite-range, DWBA calculations. In general, the calculated TAPs compared very poorly with the data, even when a ^{6}Li D-wave admixture was included in the calculations. [Tag87] These analyses suggest that mechanisms other than a direct, one-step transfer of an α-particle make substantial contributions in these reactions.

For the present work, differential cross-sections, VAPs, and the TAPs A_{xx} and A_{yy} for the $^{64}Zn(\vec{d},^6Li)$ reaction to the ground and first excited states of ^{60}Ni have been measured using a 16.4 MeV beam of polarized deuterons. The data, shown in Figures 1.1.1, 4.2.1, and 4.2.2, were taken in 5° steps from θ_{lab} = 25° to 80°. The $^{64}Zn(d,^6Li)^{60}Ni(gs)$ data were analyzed using finite-range, coupled-channels, Born approximation (CCBA) calculations that allowed for α transfers forming the ground and excited states of ^{6}Li and for coupling between these states. Two considerations motivated the inclusion of ^{6}Li excited states.

First, the predominantly negative VAP data are not readily reproduced by one-step DWBA calculations. Such calculations correspond to the solid arrow of Figure 1.1.2. All three curves in Figure 1.1.1 were generated by one-step DWBA calculations. However, we show in Chapter 6 that one-step α transfers forming the $I^\pi = 3^+$, 2.185 MeV resonance in ^{6}Li (long-dashed arrow of Figure 1.1.2) have strongly negative VAPs. These results suggest that calculations allowing for transfers forming the ^{6}Li ground and 3^+ states and for coupling between these states (all three arrows of Figure 1.1.2) might yield predominantly negative VAPs.

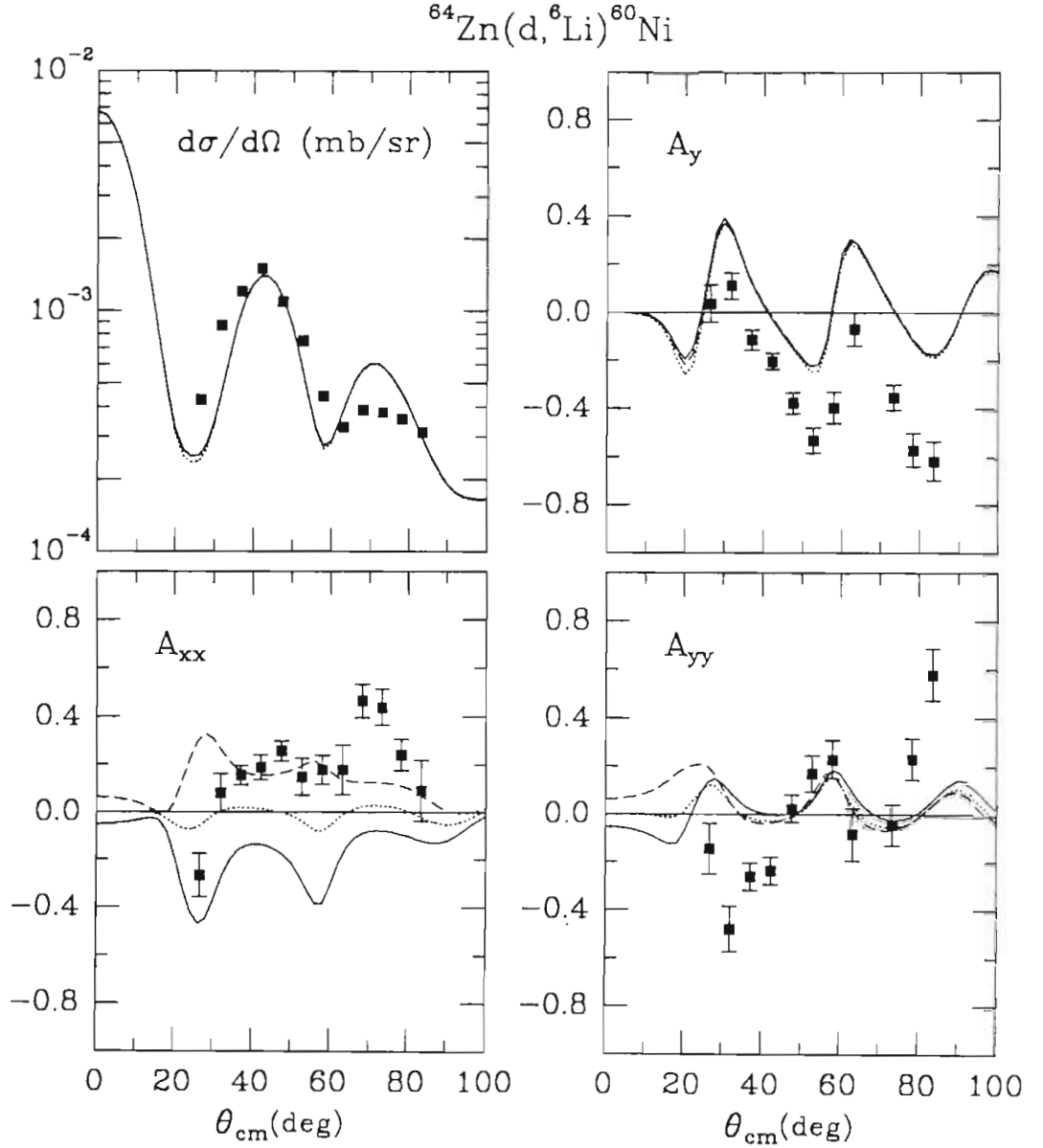

Figure 1.1.1 : Finite-Range, DWBA Calculations of Cross-sections and Analyzing Powers for the ^{64}Zn(d,^{6}Li)^{60}Ni(gs) Reaction at E_{lab} = 16.4 MeV. The dotted, solid, and dashed curves were generated using the code Ptolemy [Mac78] and assuming D_2 values of 0.0 fm^2, +0.085 fm^2, and -0.085 fm^2, respectively. A more detailed description of the calculations is given in Section 1.3.

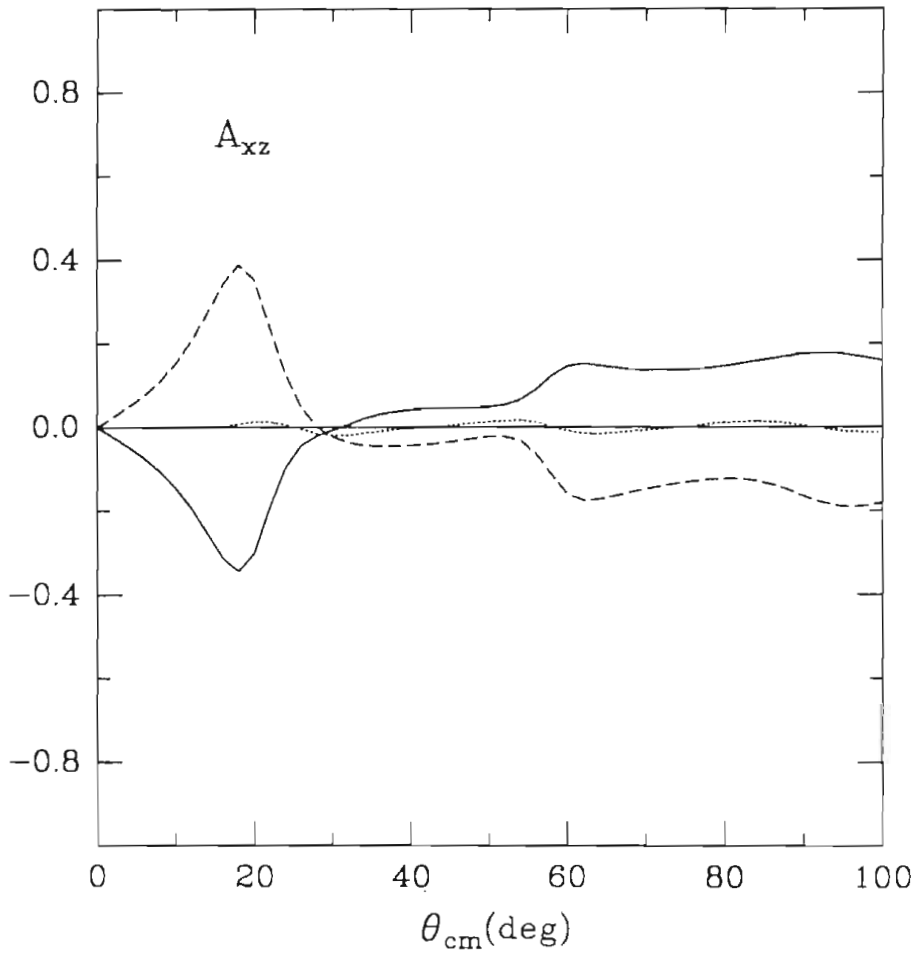

Figure 1.1.1 (continued)

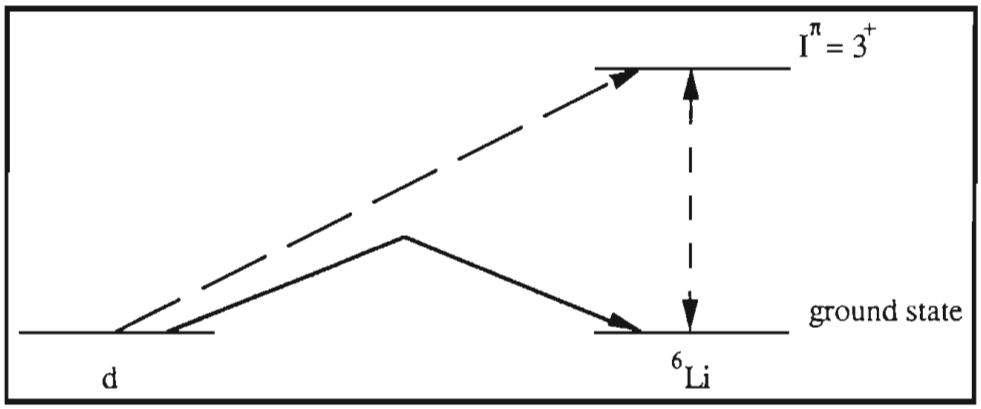

Figure 1.1.2 : Schematic Diagram of α Transfers and Couplings Involving the Ground and 3^{+} States of ^{6}Li.

Second, ^{6}Li elastic scattering is strongly influenced by projectile excitation. For example, studies of cross-section data for ^{6}Li elastic scattering at incident energies ranging from 12 MeV to 170 MeV and on targets with mass numbers between 12 to 208 have shown that the excitation and breakup of ^{6}Li reduce the effective, single-channel, real, ^{6}Li-target, central interaction in the surface region by a factor of about 0.6. [Sak87, Sak86, Gom85] Also, projectile excitation has been identified as the dominant source of non-zero VAPs in ^{6}Li elastic scattering on ^{58}Ni at E_{cm} = 12.7, 18.1, and 20.7 MeV. [Ohn84, Nis84, Nis82] Therefore, one might also expect substantial contributions to (d,^{6}Li) reactions from α transfers forming excited of states of ^{6}Li.

These α transfers are influenced by and thus probe the d-α structure of ^{6}Li. Hence, this structure is both an ingredient in our calculations and an object of study. In Section 1.2, the basics of this structure are presented. Several possible implications of CCBA analyses of ($\vec{d}$,^{6}Li) data are discussed in Section 1.3.

1.2 The Structure of ^{6}Li

A level diagram for the ^{6}Li system is shown in Figure 1.2.1. [Ajz88]

Ground State of ^{6}Li

The spin and parity of the ^{6}Li ground state are $I^\pi = 1^+$. Since d and α have $I^\pi = 1^+$ and 0^+, respectively, the orbital angular momentum of the d-α component of the ^{6}Li ground state must be $l = 0$ or 2. Hence, the d-α component of the ground state wave function can be expanded as :

$$\varphi^{1\sigma}(gs,\mathbf{r}) = b_0\, \varphi^{1\sigma}_{01}(gs,\mathbf{r}) + b_2\, \varphi^{1\sigma}_{21}(gs,\mathbf{r}), \qquad (1.2.1)$$

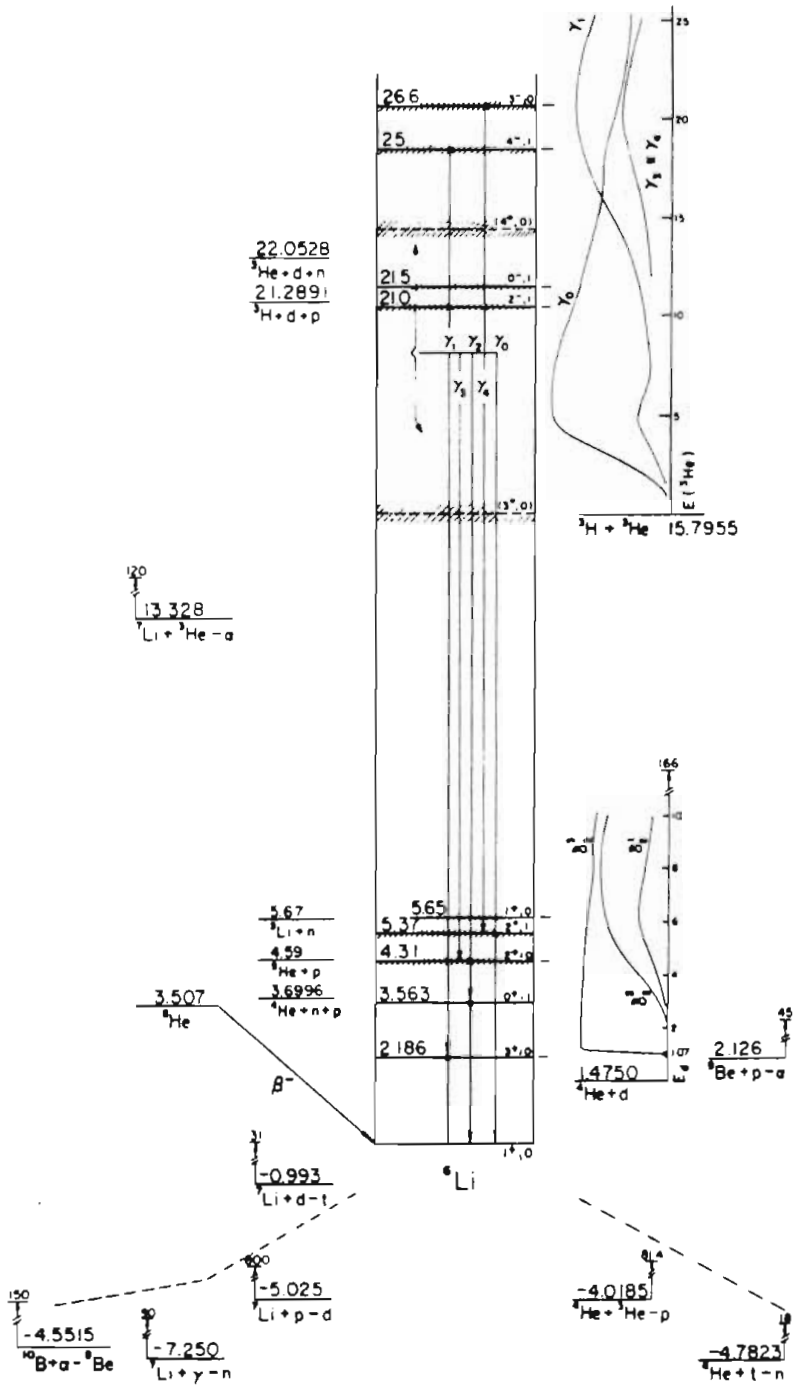

Figure 1.2.1 : A Level Diagram for the ^{6}Li System. [From Ajz88.]

where b_0 and b_2 are the S- and D-wave spectroscopic amplitudes and are subject to the condition $b_0^2 + b_2^2 = 1$. The wave functions on the right-hand side of (1.2.1) may in turn be expanded as :

$$\varphi_{l1}^{1\sigma}(gs,\mathbf{r}) = \sum_{\lambda\sigma^d} (\, l\,\lambda\, 1\, \sigma^d \mid 1\, \sigma\,)\, u_l^1(gs,r)\; Y_{l\lambda}(\,\hat{\mathbf{r}}\,)\, S_d^{1\sigma^d} \qquad (1.2.2)$$

The various 1's of equations (1.2.1) and (1.2.2) represent the spin of either ^{6}Li or d. Projections of these spins are given by σ and σ^d. The projection of l is given by λ. In this cluster model, d and α are treated as point particles with spin, meaning that wave functions describing these particles depend on spin coordinates only. Furthermore, calculations need not include a function describing the α-cluster spin, as it is zero. Hence, $S_d^{1\sigma^d}$ is the only function that depends on internal coordinates of d or α. The separation of d and α is given by $\mathbf{r}$. The radial and angular components of the d-α relative motion wave functions are $u_l^1(gs,r)$ and $Y_{l\lambda}(\,\hat{\mathbf{r}}\,)$, respectively. Angular momentum coupling is specified by the Clebsch-Gordan coefficient.

The $u_0^1(gs,r)$ and $u_2^1(gs,r)$ were calculated from the Schrodinger equation using the Woods-Saxon geometry of Kubo and Hirata [Kub72], assuming one node in $u_0^1(gs,r)$ and zero nodes in $u_2^1(gs,r)$.

The Woods-Saxon geometry of Kubo and Hirata was obtained as follows. Gammel *et al.* [Gam60] folded α-N optical model potentials over a deuteron wave function to obtain an effective interaction between d and α. Phase shifts of d-α scattering below E_{cm} = 6.7 MeV were well reproduced by this potential. Hasegawa and Nagata employed resonating group theory to generate a d-α interaction for the ^{6}Li ground state. [Has67] The potential of Hasegawa and Nagata is similar in shape and depth to the central potential of Gammel *et al.* Kubo and Hirata found that a Woods-Saxon potential of the form :

$$V_{d\alpha}(r) = \frac{-V_{d\alpha}}{1 + \exp\left(\frac{r - R_0}{a_0}\right)} \qquad (1.2.3)$$

with radius $R_0 = 1.9$ fm and diffuseness $a_0 = 0.65$ fm accurately reproduced the shape of both interactions. [Kub72]

The number of nodes in the $l = 0$ wave function, one, is well established. This number, N, can be obtained from the harmonic-oscillator energy-conservation relation :

$$2N + l = \sum_{i=1}^{2} (2n_i + l_i) , \qquad (1.2.4)$$

where n_i and l_i are the number of nodes and the orbital angular momentum of the shell model orbital of the i^{th} nucleon outside of an α-particle core. More significantly, α-n-p models of ^{6}Li predict one node for the S-wave [Par84], and analyses of ^{6}Li(e,e'd)^{4}He data have confirmed the single-node character of this wave function. [Ent86]

The number of nodes in $u_2^1(gs,r)$ is less certain. Equation (1.2.4) indicates no nodes for the D-wave. However, the α-n-p models of Lehman and Rajan predict a node when tensor forces are included in the n-p interaction. [Leh82] Zero nodes are assumed for the ground state $l = 2$ wave functions utilized in this work.

The well depth, $V_{d\alpha}$, was adjusted to reproduce the ground-state binding energy, giving $V_{d\alpha} = 77.05$ MeV for the S-wave and $V_{d\alpha} = 92.75$ MeV for the D-wave. The wave functions $r \cdot u_0^1(gs,r)$ and $r \cdot u_2^1(gs,r)$ obtained from these calculations are shown in Figure 1.2.2. Also shown are the interactions $V_{d\alpha}(r)$.

Three-body, α-n-p models of ^{6}Li yield an S-wave spectroscopic amplitude of $b_0 \approx 0.77$. [Par84] Determinations of a more experimental nature include $b_0 = 0.85 \pm 0.05$ from the ^{6}Li(e,e'd)4He reaction [Ent86] and $b_0 = 0.76 \pm 0.01$ from a distorted-wave impulse approximation analysis of the ^{6}Li(p,pα) reaction at $E_{lab} = 100$ MeV. [Roo77]

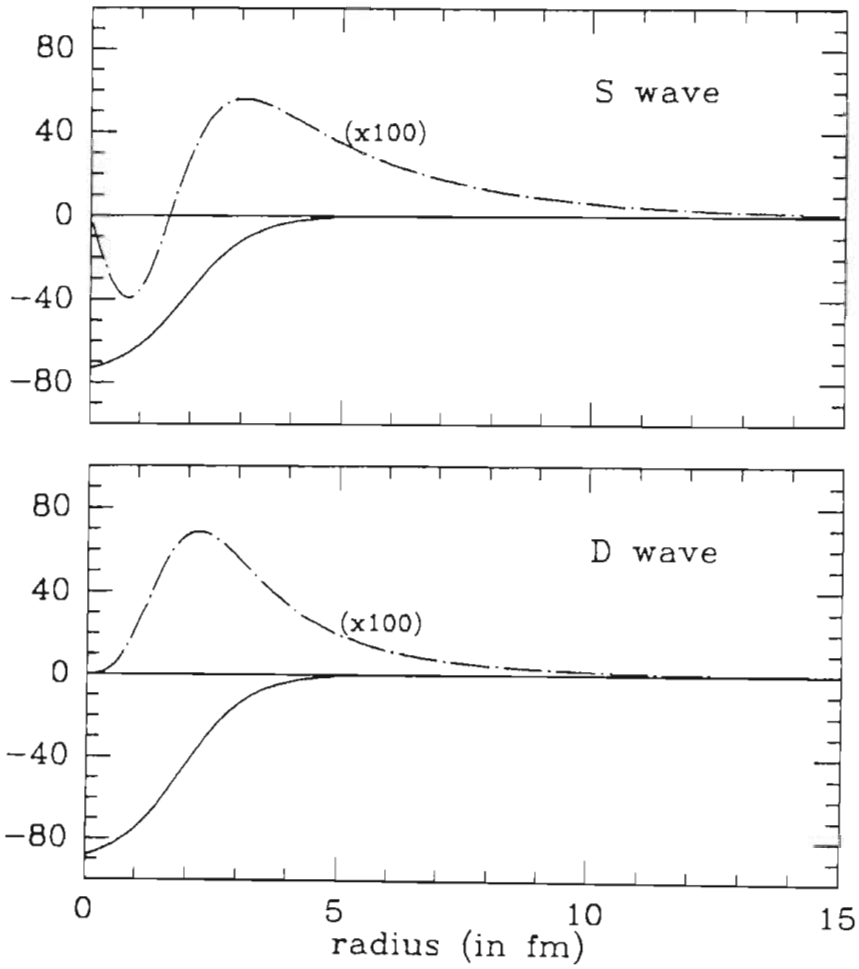

Figure 1.2.2 : Interactions and Wave Functions for the S- and D-wave Components of the ^{6}Li Ground State. The wave functions $r \cdot u_0^1(r)$ and $r \cdot u_2^1(r)$ are plotted by the dash-dot curves. The solid curves indicate the potentials $V_{d\alpha}(r)$ in which the $u_l^1(r)$ were generated.

Hence, the ^{6}Li ground state has a considerable S-wave component. In contrast, the D-wave spectroscopic amplitude is thought to be very small. The D-wave admixture should account for the difference between the quadrupole moments of ^{6}Li and d. These quadrupole moments therefore provide one means of determining the sign and magnitude of b_2/b_0. Nishioka *et al.* estimate $b_2/b_0 \approx -0.08$. In our convention, $\varphi^{1\sigma}_{01}(gs,\mathbf{r})$ and $\varphi^{1\sigma}_{21}(gs,\mathbf{r})$ are both positive as $r \rightarrow \infty$. The negative sign therefore indicates that the S- and D-waves are of opposite sign in the asymptotic region. [Nis83]

In general, the ratio b_2/b_0 is not useful for comparison between theory and experiment, because theories typically generate different model wave functions $u^1_0(gs,r)$ and $u^1_2(gs,r)$ from those employed in extracting b_0 and b_2 from experimental data. However, at values of r greater than the range of $V_{d\alpha}(r)$, the shapes of $u^1_0(gs,r)$ and $u^1_2(gs,r)$ are model independent. [Mer70, Bla52] Hence, if the (d,^{6}Li) reaction is primarily sensitive to the amplitudes of $u^1_0(gs,r)$ and $u^1_2(gs,r)$ at large r, a model-independent determination of the ratio of these amplitudes may be possible. Two quantities that compare amplitudes at large r are η and D_2.

If Coulomb interactions are ignored, $u^1_0(gs,r)$ and $u^1_2(gs,r)$ must, at large r, have the form of spherical Hankel functions. [Mer70, Bla52] Specifically :

$$\lim_{r\rightarrow\infty} b_0\, u^1_0(gs,r) \rightarrow C_0 \sqrt{\frac{\mu}{2\pi}}\ \frac{e^{-\mu r}}{r}, \text{ and} \qquad (1.2.5a)$$

$$\lim_{r\rightarrow\infty} b_2\, u^1_2(gs,r) \rightarrow C_2 \sqrt{\frac{\mu}{2\pi}}\ \frac{e^{-\mu r}}{r}\ \left[\, 1 + \frac{3}{\mu r} + \frac{3}{\mu^2 r^2}\,\right]. \qquad (1.2.5b)$$

The C_0 and C_2 are referred to as asymptotic normalization constants, and :

$$\eta = \lim_{r\rightarrow\infty} \frac{b_2\, u^1_2(gs,r)}{b_0\, u^1_0(gs,r)} = \frac{C_2}{C_0} \qquad (1.2.6)$$

is termed the asymptotic D- to S-state ratio.

The quantity usually reported in determinations of D-wave admixtures is D_2. It is defined as [Leh85, Knu75, Joh71] :

$$D_2 \equiv \frac{-1}{15} \frac{b_2 \int_0^\infty dr\, r^4\, u^1_2(gs,r)}{b_0 \int_0^\infty dr\, r^2\, u^1_0(gs,r)} \,. \qquad (1.2.7)$$

The r^4 in the numerator and the r^2 in the denominator imply that D_2 is primarily sensitive to amplitudes at large r. However, Lehman and Park have shown that D_2 is sensitive to the location of the node in $u^1_0(gs,r)$. [Leh85] An evaluation of the integrals in equation (1.2.7) assuming the wave functions of Figure 1.2.2 yields $D_2 = -1.53(b_2/b_0)$.

Definitions of the $u^1_l(gs,r)$ differ somewhat for various computer codes that calculate nuclear reaction observables. For example, some codes include a factor of i^l in these definitions. Using the plane wave approximation, Tostevin [Tos86] has calculated analytically the TAPs for the ^{64}Zn(d,^{6}Li) reaction as a function of b_2/b_0. The results of these calculations were compared with the results of plane wave calculations performed using the code Ptolemy. [Mac78] This comparison indicated that the negative values of b_2/b_0 quoted here and in [Nis84] correspond to positive values of b_2/b_0 in Ptolemy.

Unbound States of ^{6}Li

Only the ground state of ^{6}Li is bound. For energies greater than 1.47 MeV above the ground state, the d-α system forms a continuum of unbound states. Spin, parity, and asymptotic momentum characterize these states. The asymptotic momentum, k, is the relative d-α momentum when these particles are infinitely far apart and thus do not interact. It is related to the energy, ε_k, of the continuum state by :

$$\varepsilon_k = \frac{\hbar^2 k^2}{2\mu} , \qquad (1.2.8)$$

where μ is the reduced mass of the d-α system. As with the ground state, these states are not necessarily eigenstates of l^2. Table 1.2.1 lists possible values of l for several I^π states.

We point out in later chapters that low-lying resonances of the d-α system may be of particular importance in the (d,^{6}Li) reaction. Since d and α are isospin-0 clusters, resonances with a d-α structure must have isospin-0. Below ε_k = 15 MeV, only three isospin-0 resonances have been identified. These resonances have $I^\pi = 3^+, 2^+$, and 1^+ and are predominantly $l = 2$. [Jen83] Relevant information on these resonances is given in Table 1.2.2. The branching ratios, $\frac{\Gamma_d}{\Gamma}$, indicate that these resonances have considerable d-α components.

A state of given I and l is described by :

$$\varphi^{I\sigma}_{l1}(k,r) = \sum_{\lambda\sigma^d} (l\,\lambda\; 1\; \sigma^d \mid I\,\sigma)\, u^I_l(k,r)\; Y_{l\lambda}(\hat{r})\, S^{1\sigma^d}_d . \qquad (1.2.9)$$

Terms in (1.2.9) have definitions analogous to those of terms in equation (1.2.2). However, because these states are unbound, the radial wave functions of (1.2.9) obey different boundary conditions. As $r \to \infty$, these functions must satisfy :

$$u^I_l(r) \to \sqrt{\frac{2}{\pi}}\, \sin (kr - \eta \ln(2kr) - \frac{1}{2} l\pi + \xi_l + \delta_{Il}) / r , \qquad (1.2.10)$$

where ξ_l is the Coulomb phase shift, δ_{Il} is the nuclear phase shift, and η is the Coulomb parameter,

$$\eta = \frac{\mu Z_1 Z_2}{k} , \qquad (1.2.11)$$

where Z_1 and Z_2 are the charges of d and α. [Mer70]

	Positive parity states			Negative parity states		
I^{π}	1^+	2^+	3^+	0^-	1^-	2^-
l	0,2	2	2,4	1	1	1,3

Table 1.2.1 : Possible l Values for Several I^{π} States of the d-α System.

I^{π}	ε_{res} (MeV)	E_x(MeV)	Width (MeV)	Γ_d / Γ	Reference
3^+	0.711 ± 0.002	2.185	0.020 ± .003	---	[Ajz88]
2^+	2.89 ± 0.04	4.36	1.32 ± 0.04	0.967	[Jen83]
1^+	3.8 ± 0.1	5.3	1.9 ± 0.1	0.74	[Jen83]

Table 1.2.2 : Energies, Widths, and Branching Ratios of the Low-Lying $l = 2$ Resonances. The ε_{res} is the center-of-mass energy of the resonance in the d-α system. The energy of the resonance above the ^{6}Li ground state is given by E_x, which equals ε_{res} + 1.474 MeV.

l	2			1			0
I^{π}	3^+	2^+	1^+	2^-	1^-	0^-	1^+
V_0 (MeV)	85.02	73.05	65.02	81.05	73.05	69.05	77.052

Table 1.2.3 : Depths of Woods-Saxon Potentials for Various Values of I and l. The geometry of equation (1.2.3) with $R_0 = 1.9$ and $a_0 = 0.65$ was employed for all values of I and l.

The $u_l^I(r)$ were calculated from the Schrodinger equation using the interaction geometry of Kubo and Hirata, equation (1.2.3) with $R_0 = 1.9$ fm and $a_0 = 0.65$ fm. Well depths were assumed to be energy-independent and to depend on I and l as :

$$V_{d\alpha} = V_0 + (l \cdot S)\, V_{SO}, \qquad (1.2.12)$$

where :

$$l \cdot S = \frac{1}{2}[\, I\,(I+1) - l\,(l+1) - S\,(S+1)\,]. \qquad (1.2.13)$$

For the $l = 0$ component of the ground state, $V_{d\alpha} = 77.05$ MeV was determined as discussed above. A $V_{d\alpha}$ of 85.02 MeV was required to reproduce the excitation energy of the narrow, $I^\pi = 3^+$ resonance. These two well depths were utilized to obtain $V_0 = 77.05$ and $V_{SO} = 8.0$ MeV. Well depths for the remaining $l = 0$, 1, and 2 states were then calculated using equation (1.2.12) and are listed in Table 1.2.3. (McIntyre and Haeberli utilized a similar approach to describe the low-lying resonance structure of ^{6}Li. [McI67]) In Figures 1.2.3, phase shifts calculated using these potentials are plotted against those determined by Schmelzbach *et al.* [Sch72].

In Chapter 7, we discuss a procedure by which the continuum states $\varphi_{l1}^{I\sigma}(k,\mathbf{r})$ are binned to form a single wave function for each value of I and l, $l \leq 2$. A purely $l = 0$ ^{6}Li ground state wave function and these seven continuum bin wave functions are then employed in coupled-channels analyses of ^{60}Ni(^{6}Li,^{6}Li) and ^{64}Zn($\vec{d}$,^{6}Li) data measured at TUNL.

1.3 Importance of the (d,^{6}Li) Reaction

The (d,^{6}Li) Reaction as a Case Study of Transfers Involving Light Heavy-Ions

The aforementioned strong coupling between the ground and excited states of ^{6}Li has also been observed in the elastic scattering of ^{7}Li [Sak86, Nis84] and ^{9}Be [Sat79] over

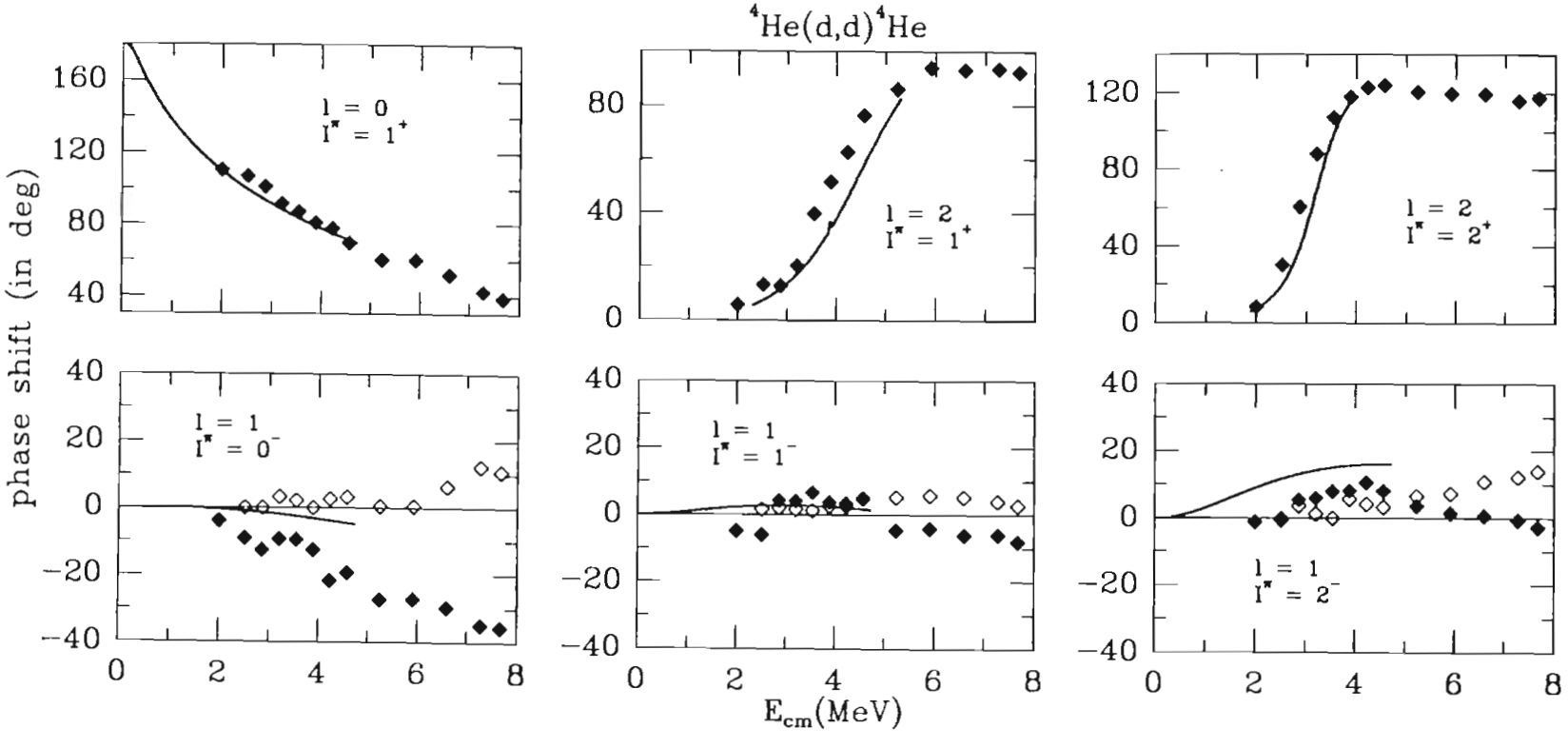

Figure 1.2.3 : Phase Shifts for ^{4}He(d,d)^{4}He Elastic Scattering. The solid diamonds represent real phase shifts determined from analyses of ^{4}He(d,d)^{4}He data. Also, $l = 1$ imaginary phase shifts are indicated by empty diamonds. [Sch72] The curves show the purely real phase shifts calculated assuming the real, central interactions specified by equation (1.2.3) and Table (1.2.3). The energy ranges of the curves correspond to those of the continuum bins discussed in Chapter 7.

a wide range of targets and incident beam energies and in the elastic scattering of ^{12}C for beam energies greater than 120 MeV. [Sak86] Furthermore, spin flip probabilities for ^{13}C inelastic scattering, asymmetries in reactions involving ^{15}N ejectiles, and cross-sections for (^{19}F,^{16}O) reactions have allowed phenomenological determinations of the spin-orbit interactions of ^{13}C, ^{15}N, and ^{19}F. These phenomenological interactions are much larger than those obtained from folding models, perhaps because of projectile excitations. [Nis84] Hence, projectile excitation may be a prominent feature in many reactions involving light, heavy-ions.

The (d,^{6}Li) reaction provides a good case for studying the effects of projectile excitation on transfer reactions. High intensity, polarized deuteron beams are available at a wide range of accelerator energies, thus allowing measurements of (d,^{6}Li) analyzing powers; analyzing powers often provide considerable information regarding reaction mechanisms. Also, deuteron elastic scattering is well understood, at least in comparison to that of heavier ions, so that uncertainties associated with distortion effects in the entrance channel are minimized. [Cle85, Tag85, Dae80] For ^{6}Li elastic scattering, cross-sections, VAPs, and TAPs have been studied extensively. These data have been well reproduced by ^{6}Li-target interactions obtained from folding models [Sak87, Nis84, Ohn84, Nis83, Coo82a] and by global, phenomenological optical model potentials. [Nad89, Coo82b]. The sparseness of isospin-0 ^{6}Li excited states make the inclusion of projectile excitation effects in (d,^{6}Li) calculations more tractable, and the d-α structure of ^{6}Li has been widely studied. [Leh86, Mer85, Jen83]

Models of ^{6}Li and Measurement of the D-wave Admixture

The curves of Figure 1.1.1 are the results of finite-range, one-step DWBA calculations performed using the code Ptolemy. Optical model interactions for the d-^{64}Zn and ^{6}Li-^{60}Ni channels were taken from the global parameterizations of Daehnick *et al.*

[Dae80] and Cook [Coo82]. A wave function for the $^{64}Zn \rightarrow {}^{60}Ni + \alpha$ bound state was generated using the Woods-Saxon geometry of equation (1.2.3) and the parameters R_0 = 4.68 fm and a_0 = 0.65 fm. [Coo84] The well depth of this interaction was adjusted to reproduce the binding energy. Also utilized were the $^6Li \rightarrow d + \alpha$ ground state wave functions $\varphi_{01}^{1\sigma}(gs,\mathbf{r})$ and $\varphi_{21}^{1\sigma}(gs,\mathbf{r})$ discussed in Section 1.2. The dotted, solid, and dashed curves were generated assuming D_2 = 0.0 fm^2, +0.0852 fm^2, and -0.0852 fm^2, respectively. Lehman and Parke obtained the value D_2 = +0.0852 fm^2 from their "full-repulsive, 4% tensor" model. [Leh85] Figure 1.1.1 indicates that the TAPs A_{xx} and A_{xz} are quite sensitive to the sign and magnitude of D_2, assuming the $^{64}Zn(d,{}^6Li)$ reaction is predominantly one-step. The disagreement between predicted (solid curve) and measured values of A_{xx} suggests that other mechanisms contribute to the reaction, though a determination of D_2 may still be possible if these mechanisms are eventually understood. Such a determination would provide a useful test for nuclear structure models of ^6Li.

The most sophisticated treatments of ^6Li are perhaps provided by three-body, α-n-p models. The primary assumption of these models is that, within ^6Li, the ^4He nucleus is never excited and does not break-up. For low-lying states of ^6Li, this assumption is reasonable, because ^4He has no excited states or breakup channels below 19.8 MeV and because the ^3He-^3H breakup channel of ^6Li lies at 15.8 MeV. [RAI75, Fia73] These models solve the Schrodinger equation for the α-n-p system using Fadeev methods, which utilize two-body interactions between the three particles, that is, n-p interactions and α-N interactions, where N stands for either n or p. The models have been utilized to calculate electromagnetic form factors of ^6Li, the magnetic moment of the ^6Li ground state, the ^6He β-decay rate, the binding energy of ^6Li, the ^6Li Coulomb energy, the resonance structure of the low-lying states of ^6Li, and observables for d-α scattering below the ^3He-^3H threshold. [Esk88, Leh86, Leh82]

Of particular relevance to the (d,^{6}Li) project are α-n-p studies of the d-α structure of the ^{6}Li ground state. These models have predicted values for the ^{6}Li → d + α momentum distribution, the effective S- and D-wave functions u_0^1(gs,r) and u_2^1(gs,r), the percentage d-α components (b_0^2 and b_2^2), the asymptotic normalization constants (C_0 and C_2), and the parameter D_2. [Leh85,Leh82,RAI75] Lehman and Park note that "the strong model dependence of D_2 makes it a good measure of the validity of the three-body model of ^{6}Li. Its successful extraction from experiment would serve as a valuable test of the subtle aspects of the three-body physics". [Leh85] For instance, the n-p tensor interaction influences the S-wave only weakly but has strong effects on the D-wave. Measurement of D_2 would thus test the role of tensor effects within the model. [Leh82] Also, it is not known whether the $S_{1/2}$ α-N interaction is "attractive-projected" or repulsive. Since predictions of D_2 depend strongly on which alternative is chosen, the measurement of D_2 might improve our understanding of this interaction, which plays a crucial role in α-N-N models and in our understanding of few-body nuclei in general. [Par84]

Measurement of α-Particle Spectroscopic Factors in Target Nuclei

If the (d,^{6}Li) reaction proceeds by a direct, one-step transfer of an α particle, S_α, the α-particle spectroscopic factor of the target nucleus, may be defined by :

$$\left(\frac{d\sigma}{d\Omega}\right)_{Exp} = S_\alpha\, b_0^2 \left(\frac{d\sigma}{d\Omega}\right)_{DWBA},$$

where b_0 is the spectroscopic amplitude of the ^{6}Li ground state. The spectroscopic factor specifies the resemblance of the target state to the wave function of an α particle orbiting the residual nucleus. Measurements of S_α provide important tests of the shell model. [Ful79,Chu78] Much work has been done on extracting values of S_α from (d,^{6}Li) reactions as well as from other α transfer reactions. [Coo84,Ume84,Jan80] Such efforts are hampered by uncertainties regarding ^{6}Li optical model parameters, the bound state

wave functions of ^{6}Li and the target, and the (d,^{6}Li) reaction mechanism. An explication of the effects of projectile excitation in (d,^{6}Li) reactions (and in other α transfer reactions) would be helpful.

Chapter 2

Target Selection

We used ^{64}Zn as the target nucleus for the ($\vec{d}$,^{6}Li) experiments. Strong compound nucleus effects were seen when lighter target nuclei were tried, and DWBA calculations indicated that for energies available with the TUNL accelerator, the Coulomb barrier between ^{6}Li and the residual nucleus strongly suppresses the (d,^{6}Li) cross-section for heavier targets. Below, these issues are discussed in more detail.

Two extreme classifications for nuclear reactions are compound and direct. In compound nuclear reactions the energy of relative motion between target and projectile becomes associated with many degrees of freedom. Because of the large available energy, nucleons from the projectile and target rearrange themselves into a state that bears essentially no resemblance to the initial state of the system. The two nuclei lose their separate identities and form a highly excited state of a compound nucleus. After a period of typically 10^{-20} seconds this excited state decays by emission of one or more particles, such as neutrons, protons, α particles, or ^{6}Li nuclei. In direct reactions most of the beam energy remains associated with the degrees of freedom describing the separation of projectile and target, although some may be shared with a few degrees of freedom within the projectile or target. For example, a few MeV may go into exciting a collective mode within the target, or a nucleon or α cluster may be transferred between target and projectile.

Our analysis of the ($\vec{d}$,^{6}Li) data (presented in later chapters) assumes that this reaction is purely direct. Therefore, the influence of compound nucleus formation on (d,^{6}Li) cross-sections and analyzing powers must be small compared to the effects of the ^{6}Li ground-state D-wave admixture and of couplings to ^{6}Li excited states. We do not know quantitatively the extent of compound nuclear contributions in (d,^{6}Li) reactions for various targets and energies available at TUNL. We do know qualitatively from excitation functions and from density-of-states considerations that compound nuclear effects are probably unacceptably large for ^{36}Ar and ^{40}Ca targets and are significantly smaller for a ^{64}Zn target.

Excitation functions, in which data are taken at a series of incident beam energies, can be used to detect compound nuclear contributions. In direct reactions the cross-section generally varies smoothly with energy, whereas for reactions strongly influenced by compound nucleus formation it will, in some cases, fluctuate. At a particular excitation energy, the effect of a given compound nuclear state on the cross-section depends primarily on the spin, I, and parity, π, of that state. Consider states of a particular I^π distributed at various excitation energies in the compound nucleus. If the average width of these states is comparable to or less than their average separation, cross-sections fluctuate with beam energy because the number of I^π states populated varies with beam energy. On the other hand, if the average width of these states is much greater than their average separation, many states are simultaneously populated at each beam energy. Fractional variations in the number of states populated are small, and the cross-section has a smoother energy dependence. Hence, excitation functions can detect compound nuclear contributions from states of a given I^π only if the average width of these states is comparable to or less than their average separation.

We have measured excitation functions of (d,^{6}Li) cross-sections for ^{36}Ar, ^{40}Ca, and ^{64}Zn targets. These data are plotted in Figures 2.1 through 2.3. In Appendix A, the

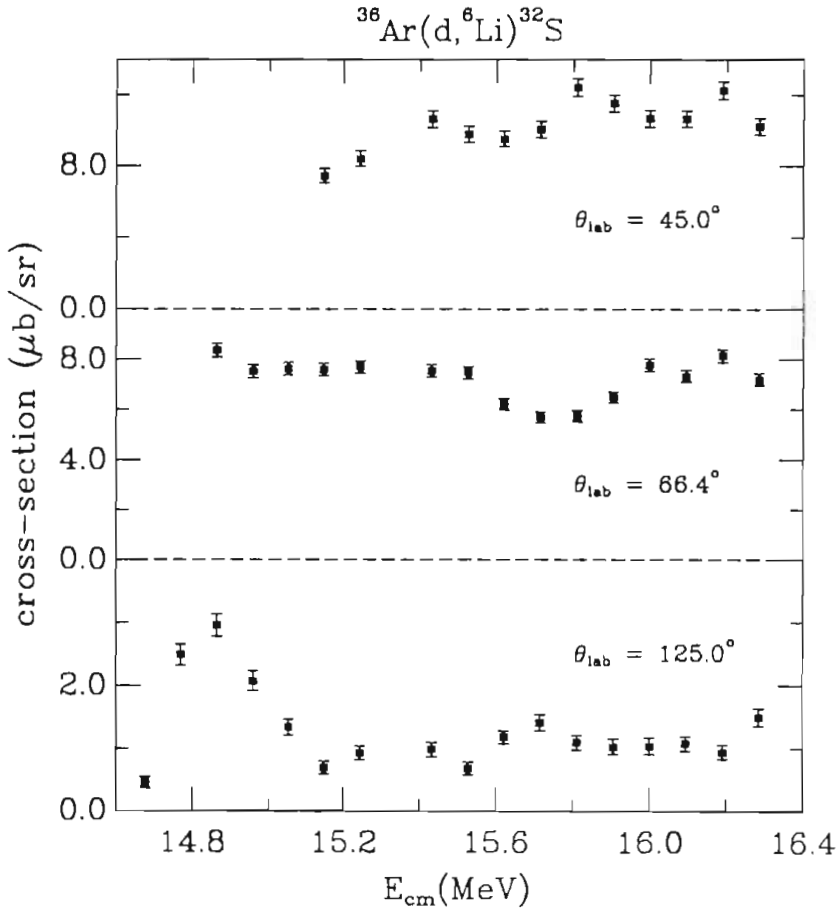

Figure 2.1 : Excitation Functions of $^{36}Ar(d,^{6}Li)^{32}S$ Cross-sections as Measured at TUNL in April, 1984.

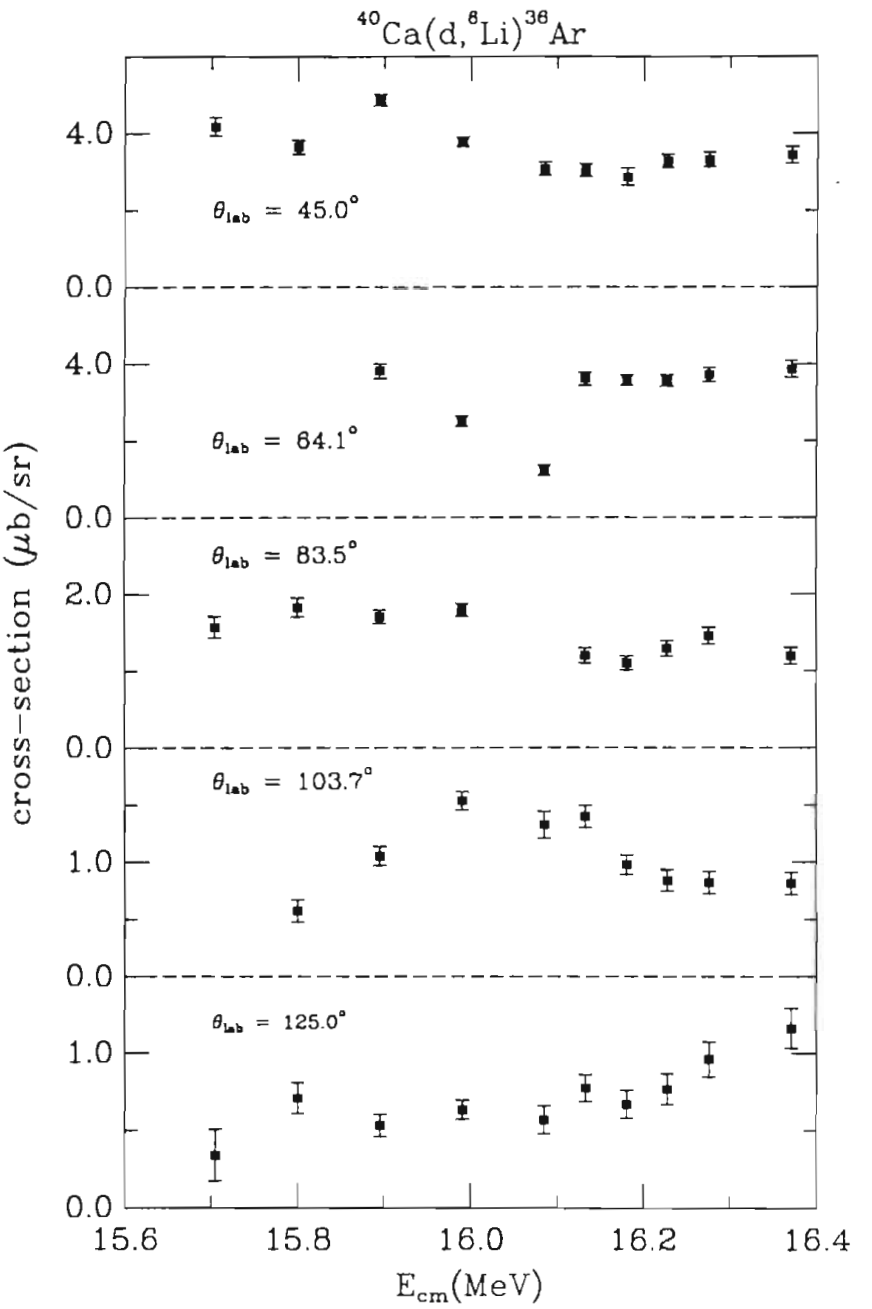

Figure 2.2 : Excitation Functions of ^{40}Ca(d,^{6}Li)^{36}Ar Cross-sections as Measured at TUNL in December, 1983.

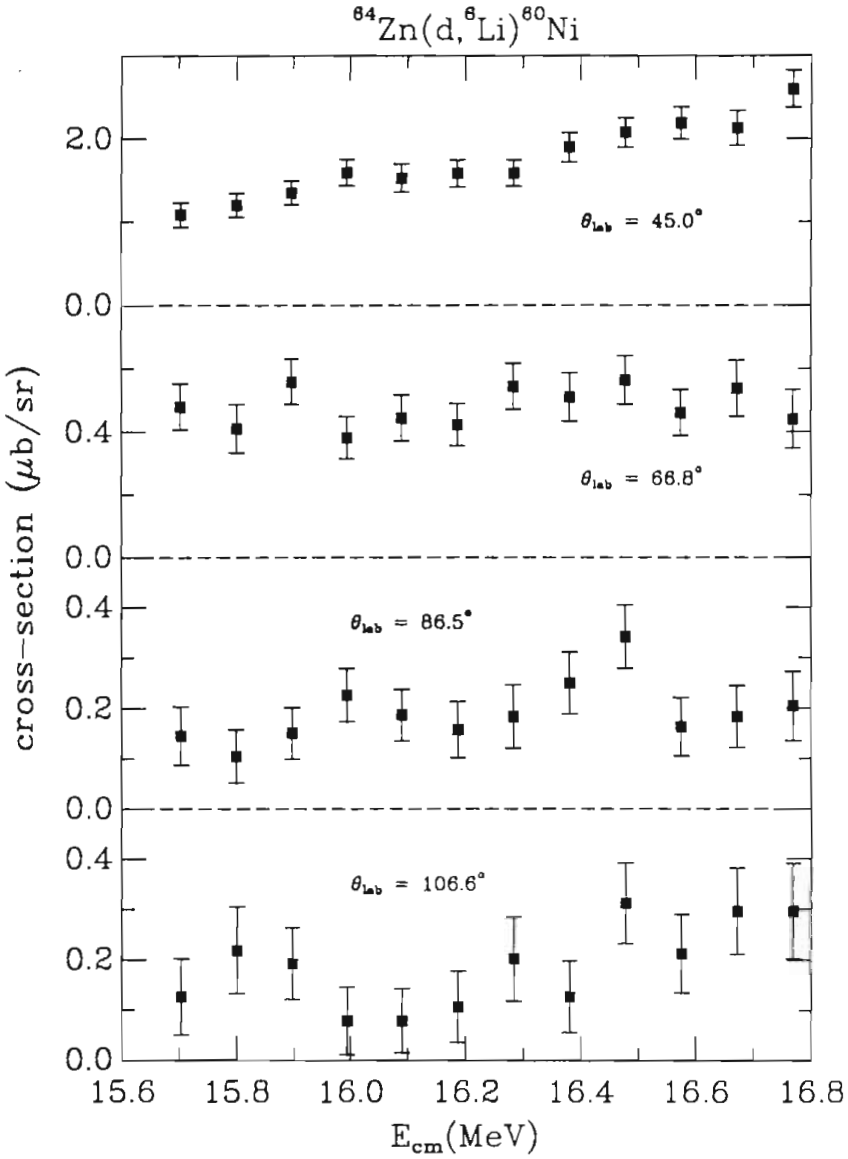

Figure 2.3(a) : Excitation Functions of ^{64}Zn(d,^{6}Li)^{60}Ni(gs) Cross-sections as Measured at TUNL in April, 1984.

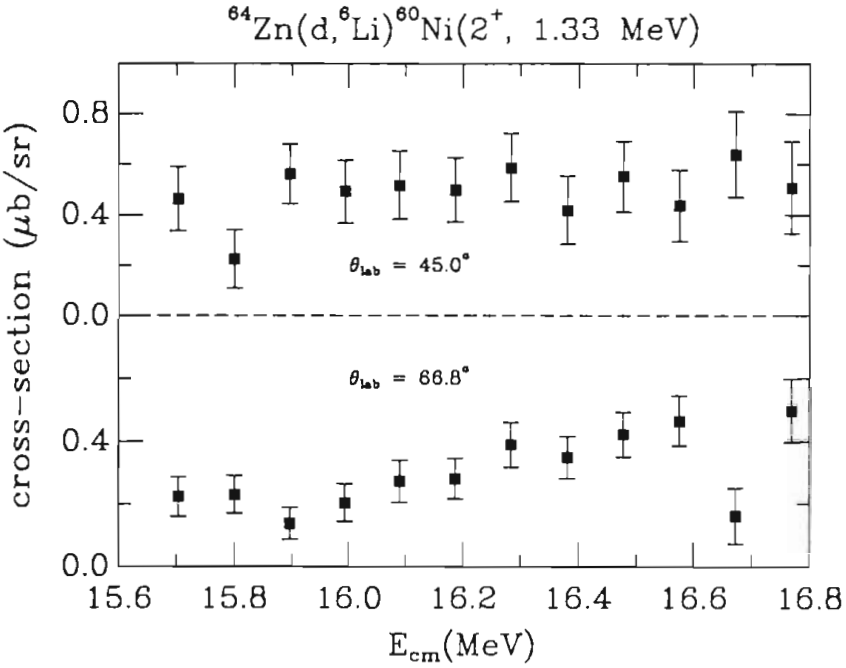

Figure 2.3(b) : Excitation Functions of ^{64}Zn(d,^{6}Li)^{60}Ni(2^{+}, 1.33 MeV) Cross-sections as Measured at TUNL in April, 1984.

data acquisition procedures are described and the data are tabulated. The ^{36}Ar and ^{40}Ca data show considerable fluctuations, indicating the presence of compound nuclear mechanisms. In contrast, apart from statistical fluctuations, the ^{64}Zn data vary smoothly with energy and thus show no evidence of compound nuclear contributions. The $^{64}Zn(d,^{6}Li)$ excitation function does not demonstrate the absence of contributions from I^{π} states whose average width greatly exceeds their average separation. Also, fluctuations that are significantly smaller than the statistical errors in these data cannot be seen. Hence, the smooth energy dependence implies only a (quantitatively unknown) upper limit on the compound nuclear amplitude.

Density-of-states arguments also suggest that compound nuclear contributions are much less important for $^{64}Zn(d,^{6}Li)$ than for $^{40}Ca(d,^{6}Li)$ and $^{36}Ar(d,^{6}Li)$. The probability that a compound nucleus decays to any one state varies inversely with the total number of states to which decay is allowed. Only states at or below a particular excitation energy, E_{max}, in each nearby nucleus are energetically accessible. One can calculate the total number of accessible states by summing up the numbers of such states in all nearby nuclei. This number increases rapidly with beam energy and target mass, and thus, the compound nuclear contribution to any one channel decreases rapidly. Gilbert and Cameron predict the density of states at a given excitation energy to be [Gil65] :

$$\rho = \frac{\sqrt{\pi}}{12} \frac{e^{2\sqrt{aU}}}{a^{1/4}\, U^{5/4}} \frac{1}{\sqrt{2\pi}\,\sigma}, \qquad (2.1)$$

where :

$U = E - P(z) - P(n)$ (in MeV),

E = excitation energy of the nucleus (in MeV),

$a = [\,(0.00917)\,(S(z)+S(n)\,) + 0.142\,]\,(A)$ (in MeV^{-1}),

A = mass number of the nucleus, and

$\sigma = 0.1111\ (aU)^{1/2}\ A^{2/3}$.

The parameters P(z), P(n), S(z), and S(n) account for variations arising from pairing and shell effects and are tabulated by Gilbert and Cameron. This formula is expected to be valid at excitation energies above :

$$E_x = 2.5 + 150/A + P(z) + P(n). \qquad (2.2)$$

Typically, E_x is between 5 and 10 MeV.

Deuterons impinging on ^{64}Zn at $E_{lab} = 16.0$ MeV produce ^{66}Ga with an excitation energy of 26.4 MeV. In nearby nuclei, E_{max} falls between 13 and 24 MeV. The number of accessible states in each nearby nucleus can be obtained by integrating equation (2.1) over energies from zero to E_{max}. These numbers are tabulated below, where the nearby nucleus is specified by the particle emitted when ^{66}Ga decays to that nucleus. The same numbers are presented for the decay of ^{42}Sc, which is excited to 25.6 MeV by 16.0 MeV deuterons bombarding ^{40}Ca. In nuclei near ^{42}Sc, E_{max} is between 10 and 22 MeV.

Table 2.1 indicates that the number of energetically accessible decay states is greater for ^{66}Ga than for ^{42}Sc by about two orders of magnitude. We thus expect the (d,^{6}Li) compound nuclear cross-section to be about two orders of magnitude smaller with ^{64}Zn than with ^{40}Ca and the compound nuclear amplitude to be about one order of magnitude smaller. This gain is offset somewhat because, as indicated by the excitation functions, the ^{64}Zn(d,^{6}Li) amplitude is less than that of ^{40}Ca(d,^{6}Li) by a factor of two or three. Even so, density-of-states considerations imply that compound nuclear effects are much less prominent in ^{64}Zn(d,^{6}Li) than in ^{40}Ca(d,^{6}Li).

Ejectile	^{42}Sc	^{66}Ga	Ratio
n	12,770	6,100,000	480
p	1,717,000	109,600,000	64
d	9,370	559,000	60
α	463,800	62,640,000	135
^{6}Li	171	6,430	381
Total	2,203,111	178,905,430	81

Table 2.1 : The Numbers of Energetically Accessible Decay States for ^{42}Sc and ^{66}Ga Nuclei Formed by Beams of E_{lab} = 16.0 MeV Deuterons Bombarding ^{40}Ca and ^{64}Zn Targets.

The excitation functions and density-of-states considerations suggest that compound nuclear contributions are small in the ^{64}Zn(d,^{6}Li) reaction initiated by E_{lab} = 16.4 MeV deuterons. However, some doubt certainly remains, and a target heavier than ^{64}Zn would be desirable. However, the use of these targets is not feasible at energies presently available with the TUNL accelerator because the Coulomb barrier for ^{6}Li strongly suppresses the cross-section. In the ^{64}Zn(d,^{6}Li) reaction at 16.4 MeV, the ^{6}Li nucleus emerges just above the Coulomb barrier. Also, ^{64}Zn has the least negative Q-value for the (d,^{6}Li) reaction of any nearby nucleus. Hence, for slightly heavier nuclei, we expect that the (d,^{6}Li) cross-section is significantly lower, and with considerably heavier nuclei, the Coulomb barrier suppresses the cross-section very strongly. If current questions regarding the approximate nature of the (d,^{6}Li) reaction mechanism are resolved, a ($\vec{d}$,^{6}Li) experiment at higher energies and perhaps also on a heavier target could be performed at another laboratory (or at TUNL after an energy upgrade) and might be important in assuring that compound nuclear effects are not undermining the information we hope to obtain by studying ($\vec{d}$,^{6}Li) data.

Chapter 3

Acquisition of the $^{64}Zn(\vec{d},^{6}Li)$ Data

The $^{64}Zn(\vec{d},^{6}Li)$ data were obtained during two week-long runs, one in February, 1986 and one in May, 1986. These experiments will subsequently be referred to as FEB86 and MAY86 and are described in detail in Section 3.1. Background reduction was a necessary and difficult aspect of the experiments. In Section 3.2, the electronic signal processing employed for these runs is specified, with an emphasis on how background arose within those electronics and on the strictly electronic aspects of background reduction. A more complete treatment of the background problem is provided in Section 3.3, where electronic effects are summarized and integrated with other considerations, such as how different types of background affected various regions of the spectra and the relative importance of different noise reduction techniques.

3.1 Experimental Procedures

Polarized Beam

A polarized deuteron beam was produced at the TUNL Lamb-shift polarized ion source. [Cle74] The polarization of such beams with respect to their spin-symmetry axis is completely described by P_z and P_{zz}, which are respectively referred to as the vector and tensor beam polarizations. They are defined as :

$$P_z = N_+ - N_-, \text{ and} \qquad (3.1.1a)$$

$$P_{zz} = 1 - 3N_0. \qquad (3.1.1b)$$

When discussing the polarization of the entire beam, N_+ (N_-) is the fraction of D^- ions whose nuclear spins are aligned with (opposite to) the magnetic field in the argon charge-exchange canal of the Lamb-shift source, and N_0 is the fraction whose nuclear spins have zero projection onto this axis. When considering the polarization of a particular D^- ion, N_+ is the probability of finding that deuteron with its nuclear spin aligned to the argon canal magnetic field, and so on.

Detailed discussions of the polarizations available from the Lamb-shift source are given in [Hae67] and [Ton80]. The ($\vec{d}$,^{6}Li) data were acquired utilizing states 1 and 2 with the so-called "strong field" in the argon canal. A D^- ion in state 1 has $P_z = P_{zz} = +1.0$ for all magnetic field values, implying a unit probability for finding that ion's spin aligned with the magnetic field. In the strong field, state-2, D^- ions have $P_z \approx 0$ and $P_{zz} \approx -2$, that is, a near unit probability for finding their spins with no projection onto the magnetic field axis. A large fraction of the deuteron beam was unpolarized, meaning that many ions had $N_+ = N_- = N_0$. Beam polarizations were measured immediately downstream from the ^{64}Zn target, and results of these measurements are listed in Table 3.1.1.

The spin direction of the beam was said to be "up" when the argon canal magnetic field pointed along the beam direction and "down" when this field was anti-parallel to the beam direction. Immediately downstream from the source, the deuteron spin symmetry axis was precessed through 90° into a vertical orientation using a Wien filter. The spins of spin-up, state-1 deuterons then pointed up toward the ceiling of the laboratory while the spins of spin-down, state-1 deuterons pointed toward the floor.

The ^{64}Zn($\vec{d}$,^{6}Li) data were obtained as prescribed by Tonsfeldt's mode-1 measurement scheme [Ton80]. This scheme required taking data with each of the eight possible combinations of beam spin direction, either up or down, beam spin state, either 1 or 2, and scattering chamber orientation either horizontal or vertical. (The significance of

the two scattering chamber orientations was that the beam spin symmetry axis was perpendicular to the scattering plane for the horizontal configuration and parallel for the vertical configuration.) The four steps of data associated with each chamber orientation were acquired "simultaneously". Specifically, the spin state was switched about every seventy seconds, and the spin direction was generally flipped once an hour. This "simultaneous" acquisition increased the similarity of conditions under which different steps of data were taken and was useful in averting potential systematic errors.

Changes in the beam spin state were accomplished as follows. The beam spin state was determined by the DC magnetic field within the spin filter of the Lamb-shift source. A potentiometer used as a programming resistance for the magnet power supply determined the value of this field. The potentiometer was set to produce the magnetic field for state 2. This field was slightly higher than that required for state 1. By connecting a much larger resistor in parallel with the potentiometer, the overall programming resistance could be lowered to produce state-1 deuterons. Electronic circuitry switched this parallel resistor in or out. Two signals were sent from this circuitry to the VAX 11-780 interface. One was utilized by event analysis (EVAL) codes to sort detector signals and scalers according to beam state; the second was connected to the interface crate inhibit to stop data acquisition during the roughly 1 second interval required to change state.

Following the polarized-ion source and the Wien filter, the deuterons were accelerated to 16.4 MeV by the TUNL FN tandem Van de Graaff electrostatic accelerator [News74], and this beam was then deflected 52° into the rotatable scattering chamber.

Scattering Chamber

In the region of the scattering chamber, the beam trajectory was constrained by slits S_1 and S_2 of Figure 3.1.1. Slit widths are given in Table 3.1.3. The distances L_1 and L_2 of Figure 3.1.1 were 20 cm and 101 cm, respectively. Beam was centered on S_1 by a set

Experiment	$P_{zz}^{(1)} = P_{z}^{(1)}$	$P_{zz}^{(2)}$
FEB86	0.671 ± 0.015	-1.131 ± 0.016
MAY86	0.536 ± 0.012	-1.215 ± 0.015

Table 3.1.1 : Beam Polarizations for the $^{64}Zn(\vec{d},^{6}Li)^{60}Ni$ Experiments.

Run	Chamber	Hours	State Changes	Spin Flips
FEB86	H	37	1900	39
	V	29	1500	29
MAY86	H	26	1350	26
	V	52	2650	23

Table 3.1.2 : Hours of Data Acquisition and Numbers of Spin State Changes and Spin Direction Flips for the $^{64}Zn(\vec{d},^{6}Li)^{60}Ni$ Experiments.

Experiment	S_1 (mm)	S_2 (mm)
FEB86	6.35 x 6.35	2.54 x 2.54
MAY86	8.89 x 8.89	2.54 x 2.54

Table 3.1.3 : Beam Collimation in the Region of the Scattering Chamber for the $^{64}Zn(\vec{d},^{6}Li)^{60}Ni$ Experiments. The labels S_1 and S_2 refer to Figure 3.1.1.

Experiment	Label	^{64}Zn	Al	Cu	C
FEB86	G44	368	4	-	1.5
MAY86	X	595	-	3	1.0

Table 3.1.4 : Target Thicknesses for the $^{64}Zn(\vec{d},^{6}Li)^{60}Ni$ Experiments. All thicknesses are in $\mu g/cm^2$. Measurements of the ^{64}Zn thicknesses are described in the text. The aluminum and copper thicknesses were measured immediately after their evaporation, while the carbon thicknesses were provided by [ARI01].

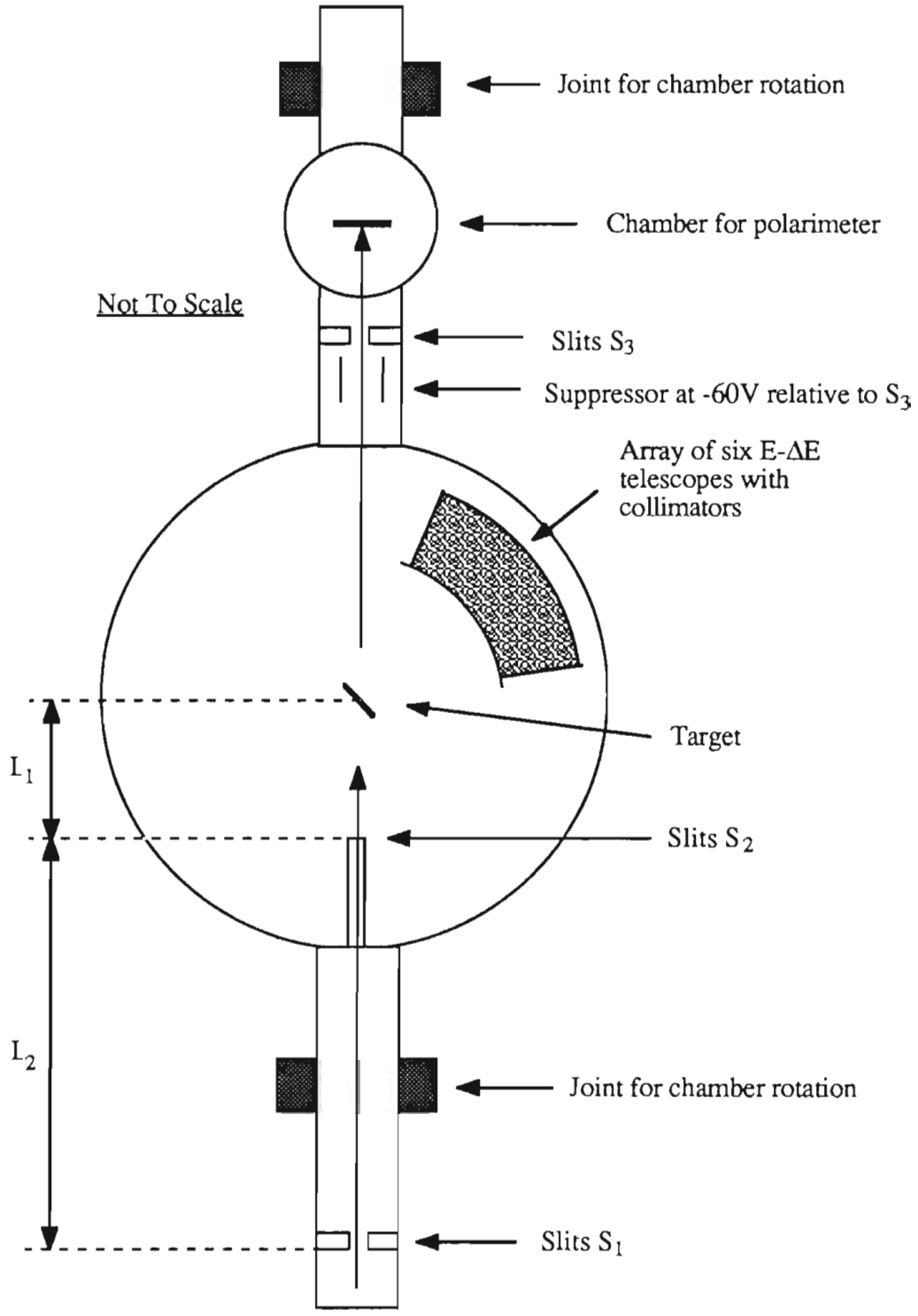

Figure 3.1.1 : Scattering-Chamber Setup for the $^{64}Zn(\vec{d},^{6}Li)$ Experiments.

Table 3.1.5 : Telescope Collimation for the $^{64}Zn(\vec{d},^{6}Li)^{60}Ni$ Experiments. Slits for the 25° to 50° telescopes were rectangular. The 55° to 80° telescopes used circular slits, whose diameters are given below. All back slits were 15.88 cm from the target. The solid angles and angular acceptances of the 60°-80° telescopes include 15% and 7% downward adjustments, respectively, as discussed in the text.

Table 3.1.5(a) : Collimators for the February, 1986 ($\vec{d}$,^{6}Li) Run.

angle	solid angle (msr)	ang. accept. (degrees)	back slits (cm)	front slits (cm)
30°	3.20	± 1.15	1.270 x 0.635	1.270 x 0.635
40°	3.20	± 1.15	1.270 x 0.635	1.270 x 0.635
50°	3.20	± 1.15	1.270 x 0.635	1.270 x 0.635
60°	4.90	± 2.27	1.346 diam	1.346 diam
70°	4.90	± 2.27	1.346 diam	1.346 diam
80°	4.90	± 2.27	1.346 diam	1.346 diam

Table 3.1.5(b) : Collimators for the May, 1986 ($\vec{d}$,^{6}Li) Run.

angle	solid angle (msr)	ang. accept. (degrees)	back slits (cm)	front slits (cm)
25°	3.20	± 1.15	1.270 x 0.635	1.270 x 0.476
35°	3.20	± 1.15	1.270 x 0.635	1.270 x 0.635
45°	3.20	± 1.15	1.270 x 0.635	1.270 x 0.635
55°	3.85	± 2.01	1.111 diam	1.346 diam
65°	4.90	± 2.27	1.346 diam	1.346 diam
75°	4.90	± 2.27	1.346 diam	1.346 diam

of horizontal and vertical steerers 6 meters upstream from S_1. These steerers were controlled by electronic circuitry and by signals indicating the amount of beam on the left, right, up, and down segments of S_1. Similar feedback steering was available for centering the beam on slits S_3. However, feedback steering for S_3 was not utilized in either $(\vec{d},^6Li)$ experimental run because we found that it markedly lowered beam current on target.

Measurements of Beam Polarization and Intensity

Beam polarization was determined using the $^3He(d,p)^4He$ reaction. A polarimeter primarily composed of three scintillators and a gas cell containing ^3He was placed in a 20.3 cm diameter scattering chamber centered 61.0 cm downstream from the center of the main scattering chamber. The polarimeter is described in detail by Tonsfeldt. [Ton80] However, since the writing of Tonsfeldt's thesis, the polarimeter has been modified. [Pie85] The original NaI scintillators were replaced by CsI scintillators. These provided much larger light pulses for incident charged particles, raising the signals of protons from the $^3He(d,p)$ reaction well above nearly all noise. Also, longer light pipes for coupling the scintillators to photomultiplier tubes were employed so that these tubes could be completely removed from the scattering chamber vacuum. Formerly, the vacuum seal had been made around the photomultiplier tubes rather than the light pipes. The new arrangement allowed for easier replacement of bad tubes and was probably conducive to longer tube lifetimes. Finally, slits which had been attached to the polarimeter were replaced by slits S_3 of Figure 3.1.1.

The beam current on target was taken to be the sum of the current that struck slits S_3 and the current that passed through these slits to strike the polarimeter. Spurious currents consisting of electrons knocked off the slits by the deuteron beam were eliminated by an aluminum cylinder aligned coaxially with the beam, placed just upstream from the slits, and biased to approximately -60 volts relative to the slits. Similar spurious currents

from the polarimeter were suppressed by biasing the polarimeter to about +45 volts relative to its surroundings. The total current and the current that struck only the polarimeter were separately monitored in the control room.

Targets

Targets were prepared by first evaporating a thin layer of either aluminum or copper onto carbon-foil slides. These slides were obtained commercially [ARI01] and consisted of a thin layer of carbon deposited on a layer of NaCl, which was in turn deposited on a 2.54 cm by 7.62 cm glass slide. Next, 99.69% isotopically pure ^{64}Zn was evaporated onto the aluminum or copper. The resulting thin film comprised of carbon, aluminum or copper, and ^{64}Zn was marked into squares about 1.3 cm on a side and released from the glass slide by dissolving the NaCl in distilled water. The 1.3 cm squares were mounted on stainless steel or aluminum rings 1.9 cm in outer diameter and 1.0 cm in inner diameter. The layer of aluminum or copper was included to help Zn atoms stick during evaporation, while the carbon was required to prevent the other two layers from breaking, perhaps because of surface tension.

Two different measurements yielded target thicknesses which differed by a factor of about two. The target thicknesses that we believe were correct and which we used to calculate the ^{64}Zn(d,^{6}Li) cross-sections are listed in Table 3.1.4. The different methods of establishing target thicknesses and our reasons for believing the values of Table 3.1.4 are detailed in Appendix B.

Detectors

Scattered ^{6}Li nuclei were detected using six E-ΔE telescopes placed on the right side of the beam at 10° intervals from 30° to 80° during the FEB86 run and from 25° to 75° during the MAY86 run. For the FEB86 run, veto detectors were placed behind the E

detectors in the 30°, 50°, and 80° telescopes. All detectors were Ortec silicon surface-barrier detectors with 150 mm^2 of active area. [Ort83] The ΔE detectors were totally depleted Ortec D-series detectors with thicknesses ranging from 18.6 μ to 30.7 μ. These thicknesses were sufficiently thin to allow ^{6}Li ions scattered from the ground and first excited states of ^{60}Ni to pass through the ΔE detector and still deposit at least 1 - 2 MeV in the E detector. All E detectors were 150 μ thick except those at 75° and 80°, which were 75 μ thick. These detectors were chosen because they were thick enough to stop all ^{6}Li ions and were less expensive than thinner or thicker detectors. The veto detectors were 300 μ thick. All detectors were operated at room temperature.

The telescopes included collimators mounted on the target side of and immediately in front of each ΔE detector. Each collimator consisted of a hollow, aluminum cylinder 1.3 cm in diameter and 5.1 cm long, capped at each end by a circular disc with a slit in the middle. Slit sizes are listed in Table 3.1.5. The slit closer to the target was referred to as the front slit while that closer to the ΔE detector was termed the back slit. For all telescopes, the back slit was 15.88 cm from the target. Slit sizes were chosen so that the back slit determined the angular acceptance and solid angle of the telescope. However, we later discovered that for the 60°-80° telescopes, the angular acceptances and solid angles were in fact limited by the 150 mm^2 active area of the E detectors, which were 17.48 cm from the target. This effect reduced solid angles by 15% and angular acceptances by 7%. Front slits were included to eliminate charged particles scattered from sources other than the target, and small magnets mounted above and below the collimators turned electrons away from the detectors.

General Experimental Considerations

Maximizing the (d,^{6}Li) count rate was the primary motivation for placing all telescopes on one side of the beam. As illustrated in Figure 3.1.2, this configuration increased the count rate in two ways.

First, placing all telescopes on one side allowed the target to be oriented so that its normal was at 45° with respect to the beam direction. This orientation increased the number of target nuclei exposed to the beam by a factor of 1/cos(45°).

Second, target thickness effects dominated the energy resolution of the ^{64}Zn(d,^{6}Li) peaks. Placing all detectors on one side and rotating the target to 45° nearly minimized the energy spread for a given target thickness and thus allowed thicker targets to be used. Those ^{6}Li nuclei formed at the upstream edge of the target traversed the entire target on their way to the telescopes and lost several hundreds of keV, whereas ^{6}Li nuclei formed at the downstream edge left no energy in the target. Thus, the energy spread of a ^{6}Li peak equaled the average energy loss of ^{6}Li nuclei traversing the entire target. (By comparison, the approximately 10 keV contributions of deuteron energy losses to peak widths were negligible.) For a given telescope, the maximum distance traversed by exiting ^{6}Li ions was $(\text{target thickness})\left(\frac{1}{\cos(\varphi)}\right)$, where φ was the difference between the telescope's angle and the target angle. Our goal of resolving the first two ^{60}Ni excited states in all telescopes required that this product be ≤ 1 mg/cm^2 for each telescope. The telescope with the largest value of φ limited the target thickness. With telescopes placed symmetrically about the beam, small values of φ could not have been obtained at all scattering angles.

With the above techniques for increasing the count rate, and assuming 120 nA of beam and a 500 ug/cm^2 target, two to three days were needed to obtain an average of 300 ^{6}Li counts per telescope in each of the eight steps prescribed by the Tonsfeldt measurement scheme. In practice, about five days were needed to obtain three days of beam on target.

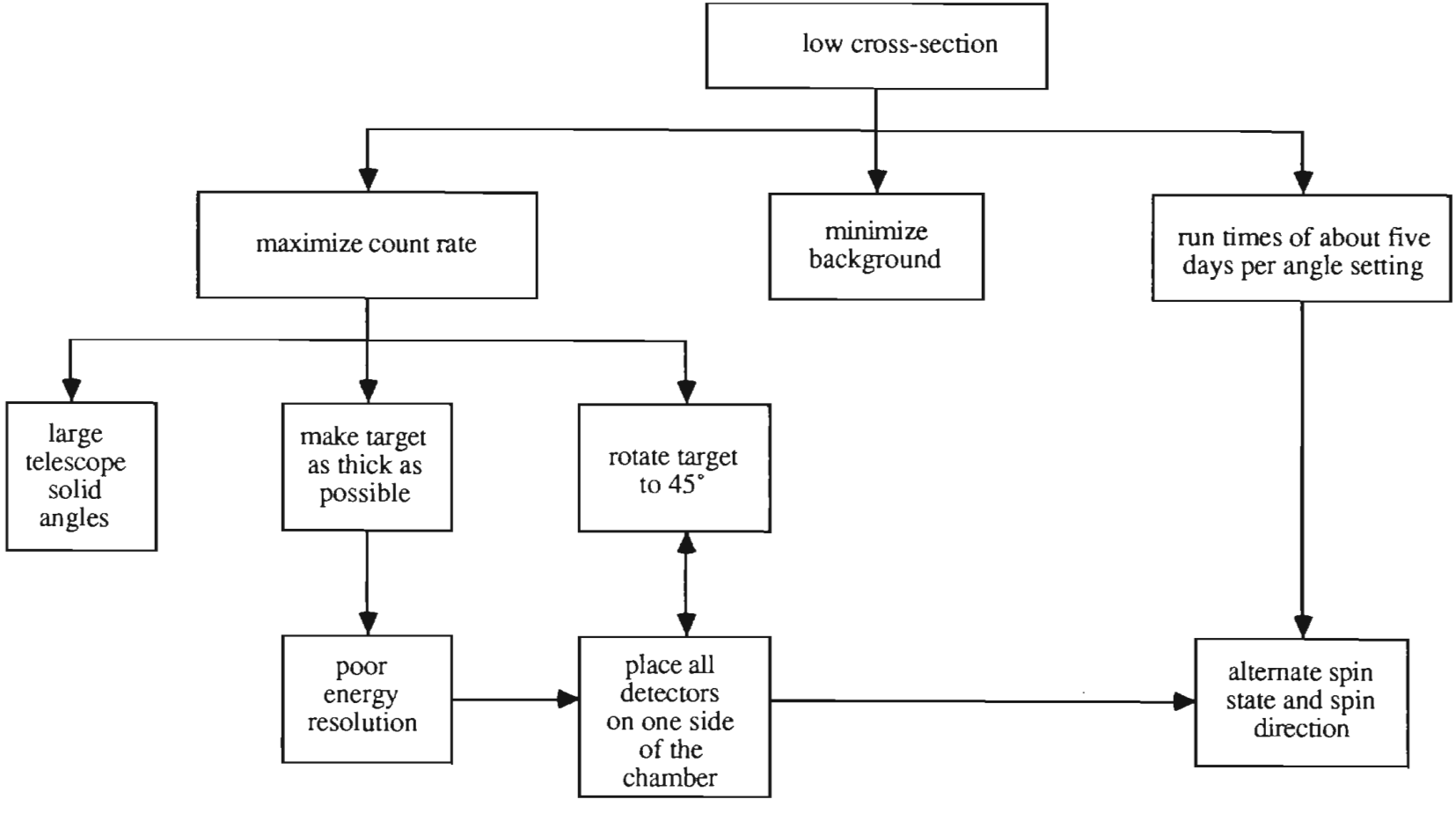

Figure 3.1.2 : The Effects of Low Cross-section on the $^{64}Zn(\vec{d},^{6}Li)$ Experiments.

The long run times and the lack of symmetrically placed telescopes increased the susceptibility of the (d,^{6}Li) experiment to systematic error. The "simultaneous" acquisition of data from different beam spin states and spin directions was adopted to reduce this susceptibility.

Another deleterious effect of the low (d,^{6}Li) cross-section was that background became a serious problem. Understanding the sources of background and methods of curtailing it requires a detailed discussion of the electronic processing of energy and timing signals from the E, ΔE, and veto detectors. This discussion appears in Section 3.2.

Software Sorting of Telescope Signals

For each of the six telescopes, signals whose amplitudes were proportional to the energy deposited in the E and ΔE detectors emerged from the electronics. For the MAY86 run, a third (TAC) signal with an amplitude proportional to the temporal separation of events in the E and ΔE detectors was also obtained. These signals were digitized by Northern analog-to-digital converters (ADCs). Because only six of these ADCs were available, each had to process E or ΔE signals from two different telescopes during the FEB86 run and E, ΔE, or TAC signals from three different telescopes during the MAY86 run. The E, ΔE, and TAC signals were digitized to values between 0 and 511, thus tying up the first nine bits of these 16-bit-output ADCs. Binary signals indicating the beam spin direction, the beam spin state, the telescope, and the status of the router pile-up bit (see Section 3.2) were attached to the higher output bits of the E ADC.

Signals from the ADC outputs entered the TUNL VAX 11-780 computer and were sorted, displayed, and analyzed using the TUNL data acquisition system XSYS. [Gou83] Specifically, the 16-bit ADC words were sent to VAX buffers via CAMAC modules and an MBD-11. Data were sorted from these buffers into FORTRAN arrays, henceforth

referred to as data areas or spectra, according to sorting algorithms specified by user-written event-analysis-language (EVAL) codes.

A two-dimensional (2-D) data area was allocated for each telescope. For each event in a given telescope, a particular element (or channel) of the 2-D data area was incremented by one, with that channel's ordinate and abscissa determined by the ΔE and E amplitudes, respectively. Thus, a 2-D histogram, such as that of Figure 3.3.6(b), was formed. For a given E signal, more highly-charged particles had larger ΔE signals, since the energy deposited in a thin layer of silicon increases with the charge of the penetrating particle. Particles of different charge thus fell into different bands, such as the α particle and ^{6}Li bands of Figure 3.3.6(b). The E-ΔE method produced a more modest separation of particles having the same charge but different mass, such as ^{3}He and α, but this mass splitting cannot be seen in Figure 3.3.6(b) and was not relevant to the detection of ^{6}Li nuclei, since any ^{7}Li nuclei that might have been produced were considerably less energetic than the ^{6}Li ions. Gates such as that shown in Figure 3.3.6(b) were placed around the ^{6}Li band.

For each telescope, four "cumulative" 1-D data areas were allocated corresponding to the four possibilities of spin direction, either up or down, and spin state, either 1 or 2. Also associated with each telescope were two "1-run", 1-D data areas, corresponding to the two spin states. For events falling within the ^{6}Li 2-D gate, a total energy was obtained by adding the E and ΔE amplitudes, and the channel corresponding to this total energy was incremented in one of the cumulative data areas and in one of the 1-run data areas. (Figure 3.3.6(c)) The target data areas were determined using the beam spin direction and beam spin state information attached to the 16-bit output of the E ADC.

As discussed earlier, the spin state was changed every 70 seconds, and the spin direction was flipped about once an hour. At the end of these "runs", during which data

were acquired with a particular spin direction, all 1-run data areas were written to a file and then cleared; the spin direction was then flipped. A series of such runs, during which the cumulative data areas were not cleared and the chamber orientation was not changed, was termed a "sequence". Several sequences of data were taken for both chamber orientations, and these data were later summed up to produce the final spectra for each orientation.

During the MAY86 run, TAC signals were sorted into 1-D data areas allocated for each telescope. Each TAC spectrum contained a large peak of true events typically 20 ns wide superimposed on a uniform background of accidental coincidences. A second set of 2-D, cumulative 1-D, and 1-run 1-D spectra were allocated. A gate was set about the TAC peak, and only events within this gate were sorted into this second set of spectra. The dotted and solid curves of Figure 3.3.6(c) show a 1-D spectrum before and after requiring the TAC gate coincidence.

Polarimeter Signal Processing

Signals from the three polarimeter photomultiplier tubes were processed through Ortec preamplifiers and transmitted to the TUNL control room on 90 Ω cables. The signals were further amplified and shaped by spectroscopic amplifiers and linear gate and stretcher modules. These signals were not summed; they were instead digitized at three different inputs of a twelve-input LeCroy ADC. Timing-single-channel-analyzers employed the spectroscopic amplifier bipolar outputs to generate logic pulses associated with each polarimeter event. Logic pulses from the three detectors were summed onto a single line and used to gate the twelve LeCroy ADC, which shared a common gate. Signals indicating the beam spin state and spin direction were digitized at two other LeCroy inputs. Varner has diagramed a very similar electronics arrangement utilized for measuring the polarization of proton beams. [Var86] As with the telescopes, four cumulative 1-D data areas were allocated corresponding to the four possibilities of spin

direction, either up or down, and spin state, either 1 or 2, and two additional 1-run 1-D data areas were allocated for the two possible spin states. Sorting of polarimeter events into these spectra was directed by EVAL codes.

Scalers and Dead Time Corrections

The total beam current and the current striking the polarimeter only were digitized by Brookhaven Instrument Corporation and Ortec 439 digital current integrators, respectively. Both strings of output pulses were counted by two LeCroy 3610 scalers. Also counted by these scalers were a 10 Hz clock and an approximately 100 Hz pulser. One of the two scaler boxes was inhibited during acquisition of the state-2 data while the other counted for both spin states.

The output of the 100 Hz pulser was also sent through the same electronic and computer signal processing as the detector pulses. Dead times were measured by comparing the number of pulses stored in the 1-D spectra with the number counted by the scalers.

3.2 Telescope Electronics

In general, scattered ^{6}Li nuclei were distinguished from α particles and other light nuclei by the large ^{6}Li ΔE signals. Large, bogus ΔE signals often created noise around the ^{6}Li peaks. Detector pile-up and router pile-up allowed ΔE signals from two ^{3}He or α particles to fuse into a single, large ΔE signal. Accidental coincidences with events in the E detector allowed many bogus ΔE signals into the spectra. Here, we describe the signal processing for the E, ΔE, and veto detectors. We explicate how pile-up and accidental coincidences arose within these electronics and detail some electronic means of curtailing this noise.

The E, ΔE, and veto signals were processed through Ortec 142A or 142B charge-sensitive preamplifiers. These preamplifiers were mounted outside of the target chamber and provided energy and timing outputs. The three darkened boxes of Figure 3.2.1 represent these preamplifiers.

The amplitudes of signals at each energy output varied linearly with the energy deposited in the depletion region of the detector. These signals had fast rise times (20 ns) but very long (500-1000 μs) exponential tails. They were transmitted via 90Ω cables to the TUNL control room. The exponential tails were undesirable because pulses from subsequent events frequently piled-up on these tails and because such pulse shapes resulted in a substantially less than optimal signal-to-noise ratio. [Leo87] Hence, Ortec 572 spectroscopic amplifiers were employed to shape these pulses into approximate Gaussians with FWHM ≈ 4.4 τ. [Ort83] Here $0.5\ \mu s \leq \tau \leq 10.0\ \mu s$ is the adjustable shaping time; it is related to the time constants of various internal differentiating and integrating circuits. Longer shaping times implied less susceptibility to noise. However, two preamplifier pulses separated by a time much less than the shaping time were blended into a single approximate Gaussian with an amplitude proportional to the sum of the two signals. Two steps were taken to reduce sharply the number of "detector pile-up" events. First, the minimum shaping time, 0.5 μs, was utilized, thus limiting the overlap of output Gaussians. Second, prior to the shaping process, which strongly attenuated both low and high frequency components, pulses contained sufficient information for signals separated by more than a few ns to be discriminated. The Ortec 572 amplifiers included circuitry which inspected for the occurrence of a second pulse during the period beginning with the rise of the first input pulse and ending when that pulse fell below a discriminator level. On the occurrence of a second pulse, this circuitry generated a logic signal at the "INH" output

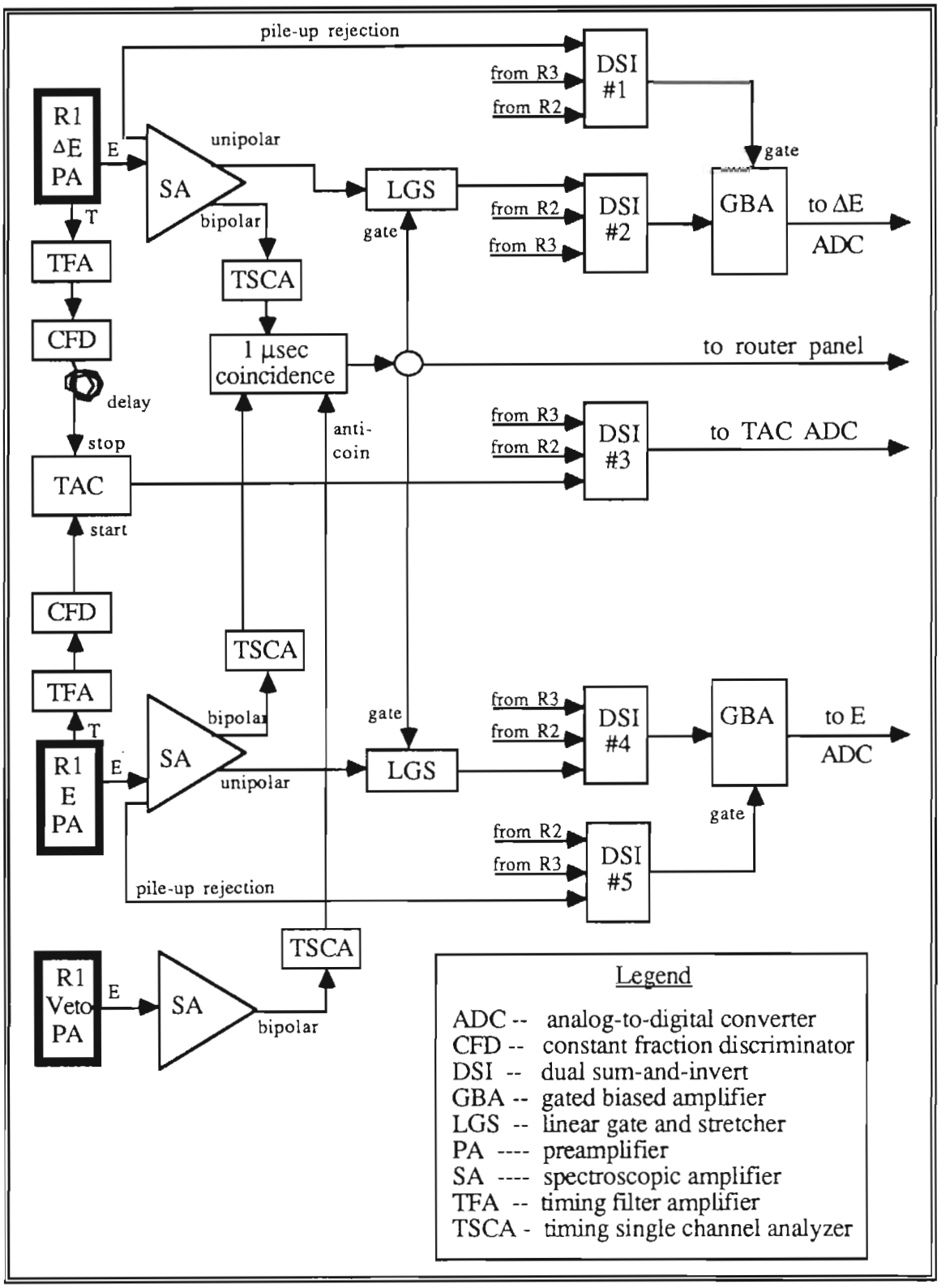

Figure 3.2.1 : Electronics for the $^{64}Zn(\vec{d},^{6}Li)$ Experiments.

of the 572, and as discussed shortly, this INH output was employed to eliminate most detector pile-up. Signals from the E and ΔE detectors were further shaped at Ortec 542 linear gate and stretcher (LGS) modules.

The E and ΔE signals were then fit to be digitized using Northern analog-to-digital converters (ADCs). As discussed in Section 3.1, during the FEB86 run each ADC had to process signals from either two E detectors or two ΔE detectors, while during the MAY86 run, each ADC had to process signals from either three E detectors, three ΔE detectors, or three time-to-amplitude converters (TACs). This feat was accomplished by summing two or three E signals onto the same line using Ortec dual sum-and-invert (DSI) boxes. The ΔE and TAC signals were likewise summed onto single lines. Summed TAC signals were then sent directly to ADCs. Signals from E and ΔE detectors were sent to ADCs via Ortec gated biased amplifiers (GBAs). The gate on these biased amplifiers was closed on the occurrence of an INH output from the 572 amplifiers, thus rejecting events subjected to detector pile-up.

Because signals from different telescopes were summed onto one line, a means for identifying the source telescope of each signal was needed. Bipolar outputs of E and ΔE spectroscopic amplifiers were fed into Ortec 551 timing single-channel analyzers (TSCAs). These TSCAs generated pulses which were subsequently examined by an Ortec coincidence module. This coincidence module produced an output logic pulse provided that during a 1 μs period pulses were received from both the E and ΔE TSCAs. The coincidence box outputs of the two or three telescopes sharing the same set of ADCs were sent separately to a locally constructed, 8-input router at the VAX 11-780 interface. Three binary outputs associated with this router indicated the router input at which a given gate arrived, hence specifying the source telescope.

Summing of E (ΔE) signals from two or more telescopes at DSI box 2 (4) of Figure 3.2.1 allowed for a second type of pile-up, known as router pile-up. If the time separating two signals exceeded the average 1-2 μs width of the signals, the summed signals appeared as shown in Figure 3.2.2(a). Once the GBA detected a maximum in the first signal, it blocked the input of all subsequent signals until the first signal fell below a discriminator level near ground and until the GBA had finished generating an output associated with the first signal. The GBA thus prevented the second signal from piling-up with first. However, if the temporal separation of the two signals was less than their average width, the summed signals appeared as in Figure 3.2.2(b). The GBA did not sense a maximum during period X and instead generated an output whose amplitude was proportional to the voltage during period Y of Figure 3.2.2(b).

Closely spaced coincidence box output pulses were associated with any two closely spaced E or ΔE signals. Output for the in-house, 8-input router included a "pile-up" bit which was zero except when two coincidence box pulses arrived within 1 μs. Software sorting codes rejected all events for which this bit equaled one. Hence, router pile-up could be curtailed using this bit, provided the widths of the LGS output signals were limited to 1 μs.

The LGS modules were gated by the coincidence box output, so that E and ΔE signals were terminated if, for any reason, a coincidence pulse did not occur. Two different background reduction procedures utilized this gating. First, lower level discriminators on all ΔE TSCAs were raised so that TSCA output pulses were not generated for proton, deuteron, triton, ^{3}He, or α ΔE signals. Consequently, no coincidence pulse was produced and the E and ΔE signals associated with these events were blocked at the LGS modules. This technique provided a second means of eliminating router pile-ups. Second, coincidence pulses were not generated for events that included a

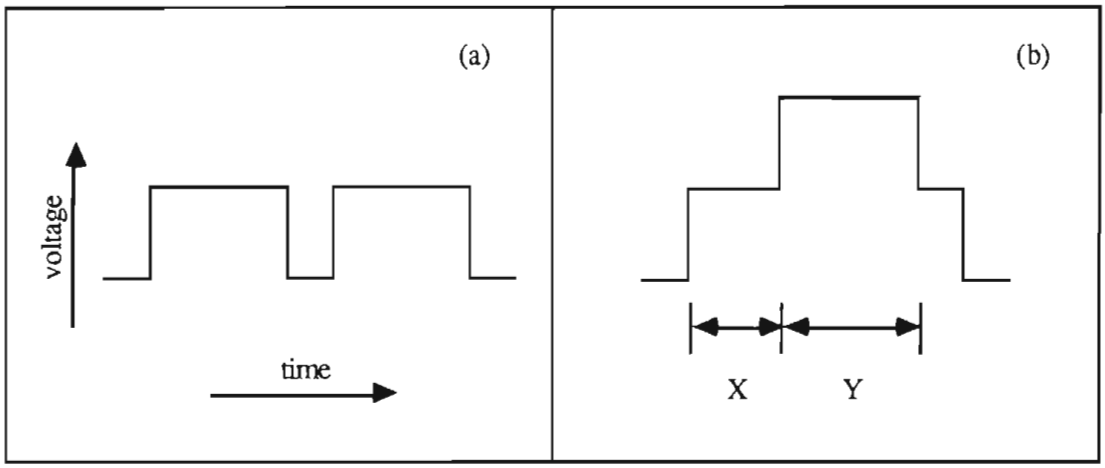

Figure 3.2.2 : Sample Outputs for Dual-Sum-and-Invert Boxes 2 and 4. Part (b) illustrates router pile-up.

TSCA output pulse for the veto detector. Types of background eliminated by this anti-coincidence requirement are discussed in Section 3.3.

The electronic and software processing of the data had to keep track of which E and ΔE signals were associated with each event. This task was accomplished primarily by the coincidence box, which required E and ΔE signals to arrive within 1 μs of each other and which, via the LGS gate, terminated all other signals. However, when two events arrived within 1 μs, the ΔE signal from one pulse sometimes became associated within the E signal from another pulse. Such occurrences were referred to as accidental coincidences.

The number of accidental coincidences could be reduced by narrowing the time window during which a coincidence was required to occur. During the MAY86 run, signals from the preamplifier timing outputs were transmitted to the TUNL control room via 50Ω cables and were processed through Ortec 474 fast timing filter amplifiers and through constant fraction discriminators (CFDs). The CFDs produced narrow pulses, and TACs generated a signal whose amplitude was proportional to the temporal separation of these pulses. As discussed in Section 3.1, the TAC outputs were sorted into data areas. All good events, whether ^{6}Li nuclei, α particles, or lighter particles, sorted into a sharp peak. For accidental coincidences, the sources of E and ΔE signals were uncorrelated, so these events were evenly distributed throughout the data area. A software gate was placed around the peak, and events whose TAC signals fell outside this gate were rejected. The time per channel in these data areas was calibrated by delaying the ΔE timing signal by a known amount and noting the shift in the TAC peak. Temporal widths of the TAC software gates were then be determined to be 17, 11, 37, 20, 51, and 29 ns for the 25° to 75° telescopes, respectively. These coincidence windows were thus about a factor of 50 narrower than the 1 μs window provided by the "slow" coincidence box. We found that full biasing of detectors to compensate for voltage drops due to leakage currents was

critical to obtaining good time resolution in the TAC spectra, probably because full biasing decreased the rise time, and therefore the spread in rise time, of signals in these detectors. For the same reason, use of detector cooling and, in some cases, higher quality detectors might have helped. During the FEB86 run, similar "fast" timing circuits were employed for the 30° and 70° telescopes. However, the TACs and the subsequent software sorting of TAC outputs were replaced by Ortec fast coincidence modules. The temporal resolutions for these two telescopes are not known. The use of TACs and software gating was superior to the use of fast coincidence modules because the TAC data areas offered a clear picture of the timing characteristics of each telescope. Optimal locations and widths of the TAC gates were easily identified, and problems, such as poor time resolution or timing shifts, were readily detected. Also, event mode storage of the data allowed one to re-sort the data with different TAC gates during the analysis following the experiment.

3.3 Background Reduction

The E-ΔE particle identification (PID) method was a background reduction technique. It discriminated against an enormous number of protons, deuterons, tritons, ^{3}He and α particles which would have otherwise overwhelmed the ^{6}Li nuclei. In practice, background was present even with the E-ΔE PID system, mainly because signals from two lighter particles combined to simulate one ^{6}Li signal. More specifically, protons, deuterons, tritons, ^{3}He and α particles all produced E signals comparable to those of ^{6}Li. The ^{6}Li nuclei deposited about twice as much energy in the ΔE detectors as did ^{3}He or α particles, and they deposited far more energy than the protons, deuterons, or tritons. Thus, all noise in the region of the ^{6}Li peaks involved large, bogus ΔE signals. The 2-D spectrum of Figure 3.3.1 includes an abundance of such noise, and Figure 3.3.2 illustrates how severe this background can be in the corresponding 1-D spectra. Figures 3.3.3 and 3.3.4 show 1-D spectra from the last two (d,^{6}Li) experiments and demonstrate the effectiveness of our efforts to attenuate background.

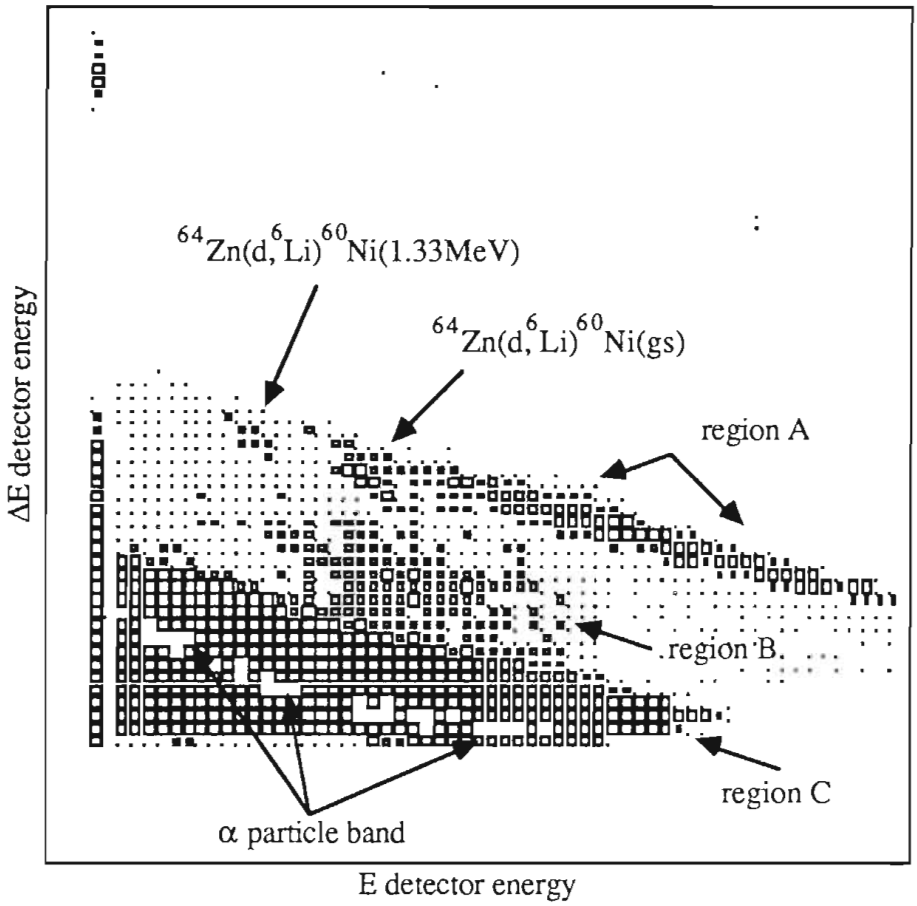

Figure 3.3.1 : Regions of Background in the E-ΔE Spectra. Events in region A resulted from pile-up of two α particles, both of which entered the E and ΔE detectors. Pile-ups of an α particle stopped in the ΔE detector with an α particle entering both detectors populated region B, as did accidental coincidence events. The pile-up of α particles with protons, deuterons, or tritons produced counts in region C. The proton, deuteron, and triton bands were excluded from this spectrum by lower-level discriminators on the ΔE TSCAs.

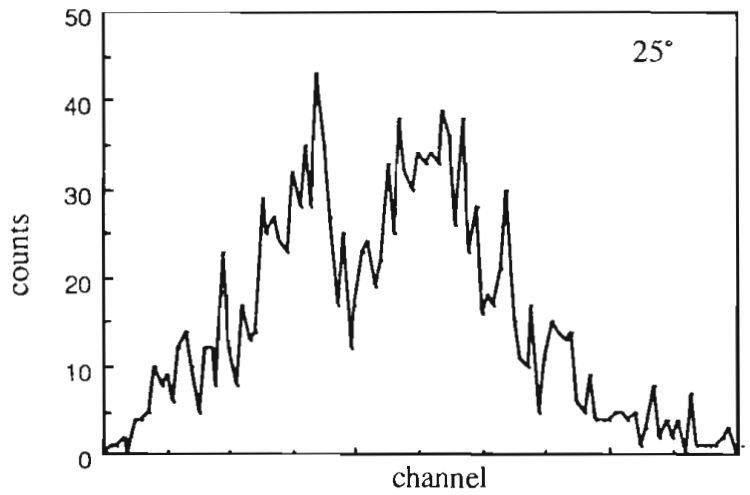

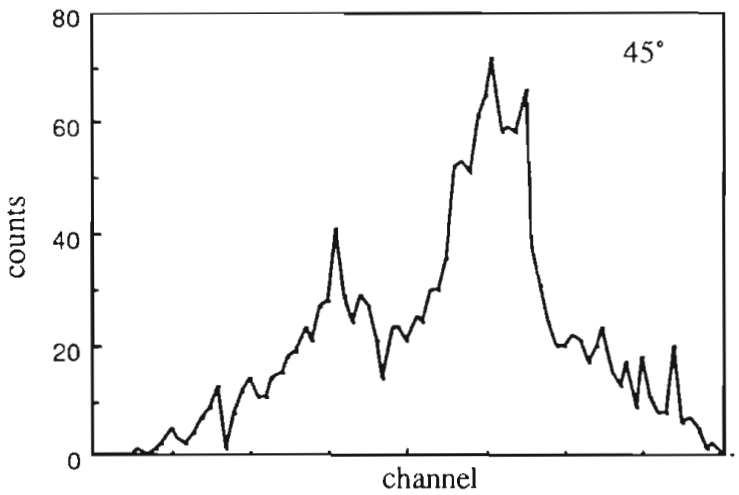

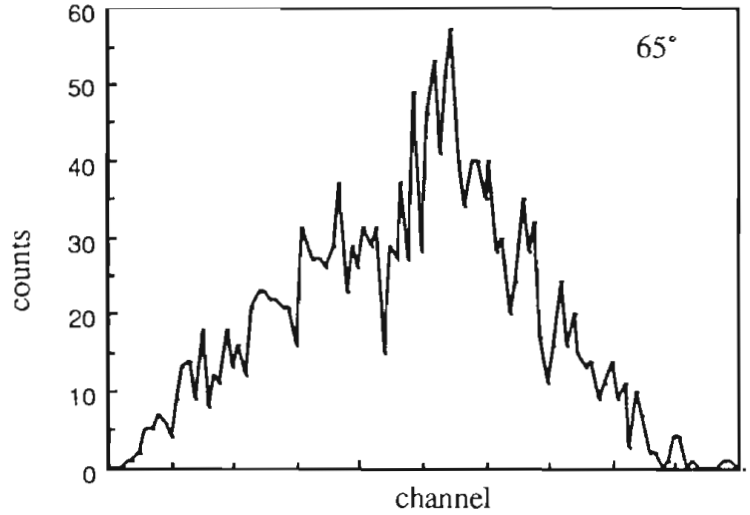

Figure 3.3.2 : Spectra, Taken in August, 1985, Illustrating the Severity of Background Prior to the Implementation of Background Reduction Techniques. Each spectrum includes peaks corresponding to the $^{64}Zn(d,^{6}Li)$ reaction forming the ground and first excited states of ^{60}Ni. The hump shape of the background resulted from the 2D gates, which included many channels corresponding to the average energy within the gate but very few channels corresponding to the extreme higher and lower energies.

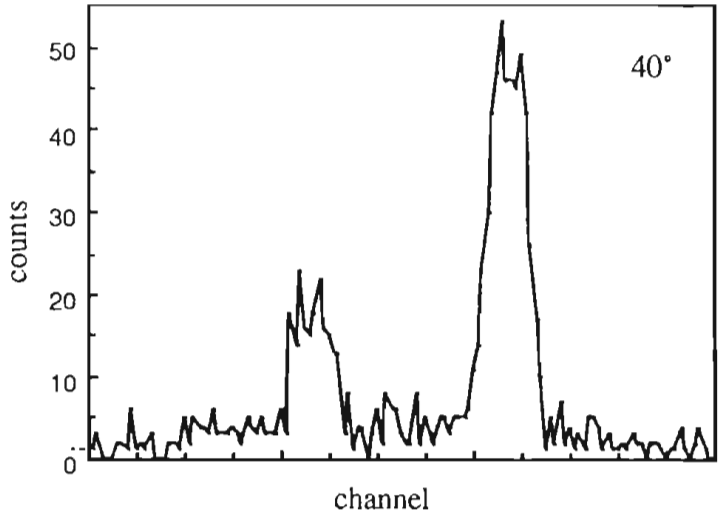

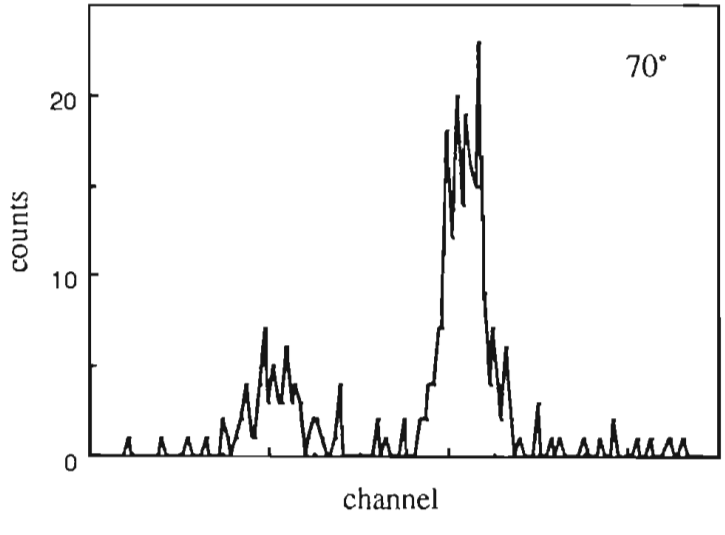

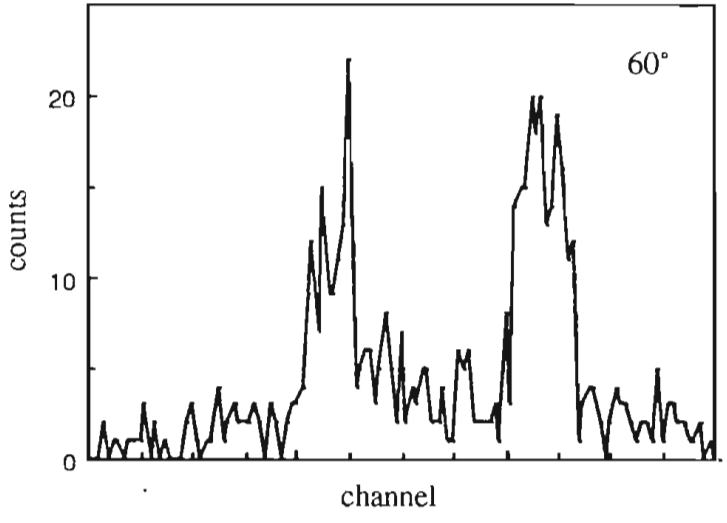

Figure 3.3.3 : Spectra from the February, 1986 $^{64}Zn(\vec{d},^{6}Li)$ Experiment. The two peaks correspond to the $^{64}Zn(d,^{6}Li)$ reaction forming the ground and first excited states of ^{60}Ni. Fast coincidence was utilized at 70° but not at 40° or 60°.

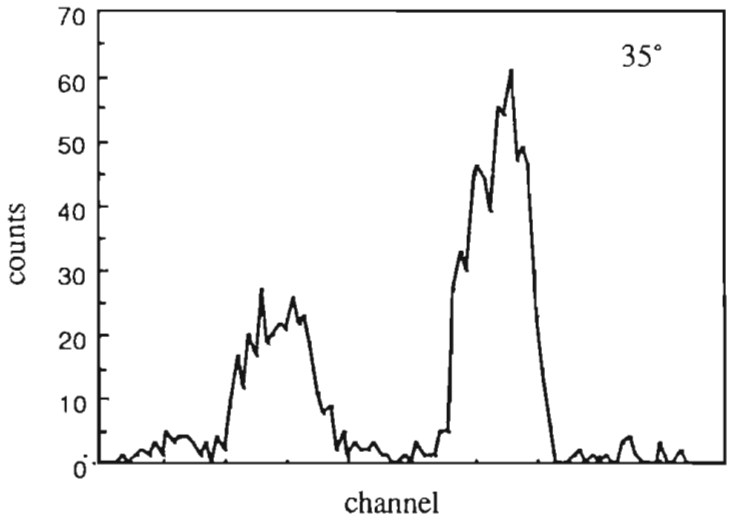

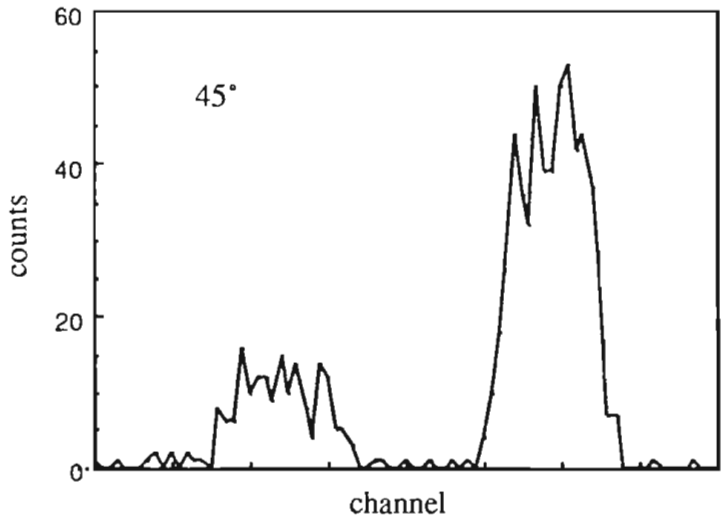

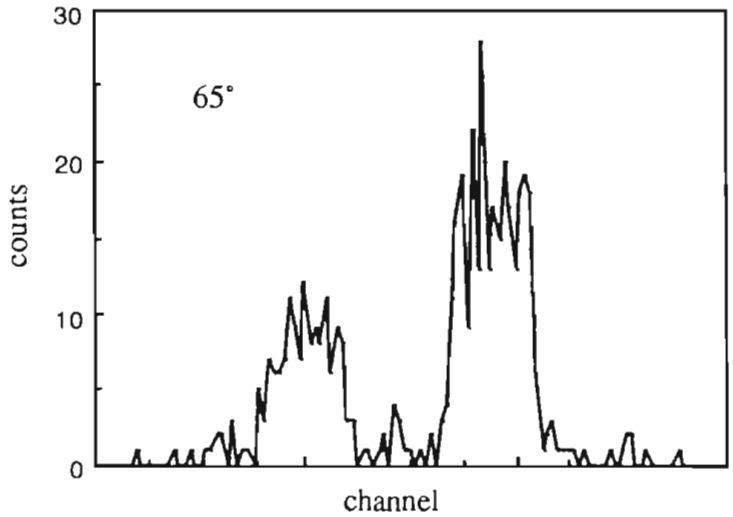

Figure 3.3.4 : Spectra from the May, 1986 $^{64}Zn(\vec{d},^{6}Li)$ Experiment. The two peaks correspond to the $^{64}Zn(d,^{6}Li)$ reaction forming the ground and first excited states of ^{60}Ni. Fast coincidence was applied at all angles. A spectrum for the 25° telescope is shown with the solid line of Figure 3.3.6(c).

Types of Background

As discussed in Section 3.2, pile-up involved summing ΔE and/or E signals from two different events and was therefore a possible source of large, bogus ΔE signals. Detector pile-up occurred when two particles entered the same telescope at nearly the same time and the corresponding signals fused at the spectroscopic amplifiers. Router pile-up resulted when two events occurred in different telescopes and their signals fused at dual sum-and-invert modules.

In the 2-D spectra, the pile-up of E and ΔE signals from two α particles† resulted in a band of noise parallel to the α band, as in region A of Figure 3.3.1. Consider the following argument. The α band is crudely a line segment. Let m be the slope of this line segment and b the ΔE intercept. Let two α events generate signals (E',ΔE') and (E",ΔE"). Each pair of signals is required to fall on the α band.

$$\Delta E' = m E' + b \qquad (3.3.1a)$$

$$\Delta E'' = m E'' + b \qquad (3.3.1b)$$

When pile-up occurred in both detectors, the summed ΔE and E signals were subject to the restriction :

$$(\Delta E' + \Delta E'') = m (E' + E'') + 2b,$$

or :

$$\Delta E_{pu} = m E_{pu} + 2b, \qquad (3.3.2)$$

---

† The "α particle" bands of the 2-D spectra also included ^{3}He events. In general, ^{3}He particles contributed to background by the same mechanisms as did α particles. For brevity, we refer to the α particles only.

where $\Delta E_{pu} = \Delta E' + \Delta E''$ and $E_{pu} = E' + E''$. This band paralleled the α band but was displaced outward twice as far along either axis. In Figure 3.3.1, region A stands in just such a relation to the α band.

What about the case in which one α was stopped in the ΔE detector? The ΔE signal of the stopped α could lie anywhere between zero and ΔE_{max}. The maximum energy that the α could deposit in the ΔE detector was determined by the detector's thickness. The E and ΔE signals from the α that entered both detectors were still restricted by equations (3.3.1). To this ΔE signal, the stopped α added an energy somewhere between zero and ΔE_{max}. Hence, such pile-up events sorted into the region above the line segment of equation (3.3.1). Many of the events in region B of Figure 3.3.1 were probably detector pile-ups of two α particles, one of which was stopped in the ΔE detector. Router pile-up should not have populated region B. A coincidence box pulse should not have been generated for the stopped α, since it lacked an E signal, and its ΔE signal should therefore have been blocked at the LGS module.

Region C contains pile-ups between one α and one proton, deuteron, or triton. These events did not create background in the region of the ^{6}Li peaks.

Router pile-up was nearly eliminated by use of the "pile-up" bit at the router panel. This bit was zero except when timing pulses from two or more telescopes arrived at the router within 1 μs. EVAL codes read this bit and rejected events for which the bit equaled one. Figures 3.3.5 (a) and (b) illustrate the effectiveness of this technique. The spectrum in 3.3.5(a) was acquired without utilizing the router pile-up bit. Figure 3.3.5(b) displays a spectrum acquired under nearly identical conditions, except that the router pile-up bit was employed. In region A of these Figures, use of the pile-up bit eliminated 93% of the events, indicating that this region had been dominated by router pile-up and that the pile-up bit was effective against this type of background. The number of events in region B was

not significantly reduced, suggesting that, as expected, router pile-up did not populate this region. Router pile-up was also reduced by raising lower level discriminators on the ΔE TSCAs so that ΔE TSCA outputs were not produced for α particles and lighter particles. The E and ΔE signals for these particles were thus blocked at the LGS boxes. These two methods of eliminating router pile-up were, of course, redundant.

The spectroscopic amplifiers inspected for detector pile-up prior to pulse shaping, which discarded the information needed to discern a pile-up. Occurrence of a pile-up was indicated by a logic signal at the amplifier's INH output, and this output was employed to terminate the event at the gated biased amplifier. We have no direct test of the effectiveness of this detector pile-up rejection scheme. However, detector pile-up rejection was employed in the two runs associated with Figures 3.3.5. It apparently worked well, since once router pile-up events were also eliminated, little background remained in region A.

The telescope collimators forced charged particles to traverse the detectors in a direction roughly perpendicular to the detector surface. Along such a direction, α particles and lighter nuclei could not produce ΔE signals which rivalled those of ^{6}Li. However, these charged particles may have interacted with protons or α particles in the detector, knocking them sideways through the silicon and thus producing a sizable ΔE signal. Also, neutrons and γ-rays may have penetrated the telescope collimation system and knocked protons or α particles sideways through the ΔE detector. These mechanisms did not produce E signals, and the ΔE signals were usually eliminated by the requirement that an E and ΔE pulse arrive at the coincidence box within one μs. However, in some cases an accidental coincidence occurred between a large, bogus ΔE signal and an uncorrelated E signal. Accidental coincidences may have also enabled ΔE pile-up events (that were not eliminated by other means) to survive the E-ΔE coincidence requirement.

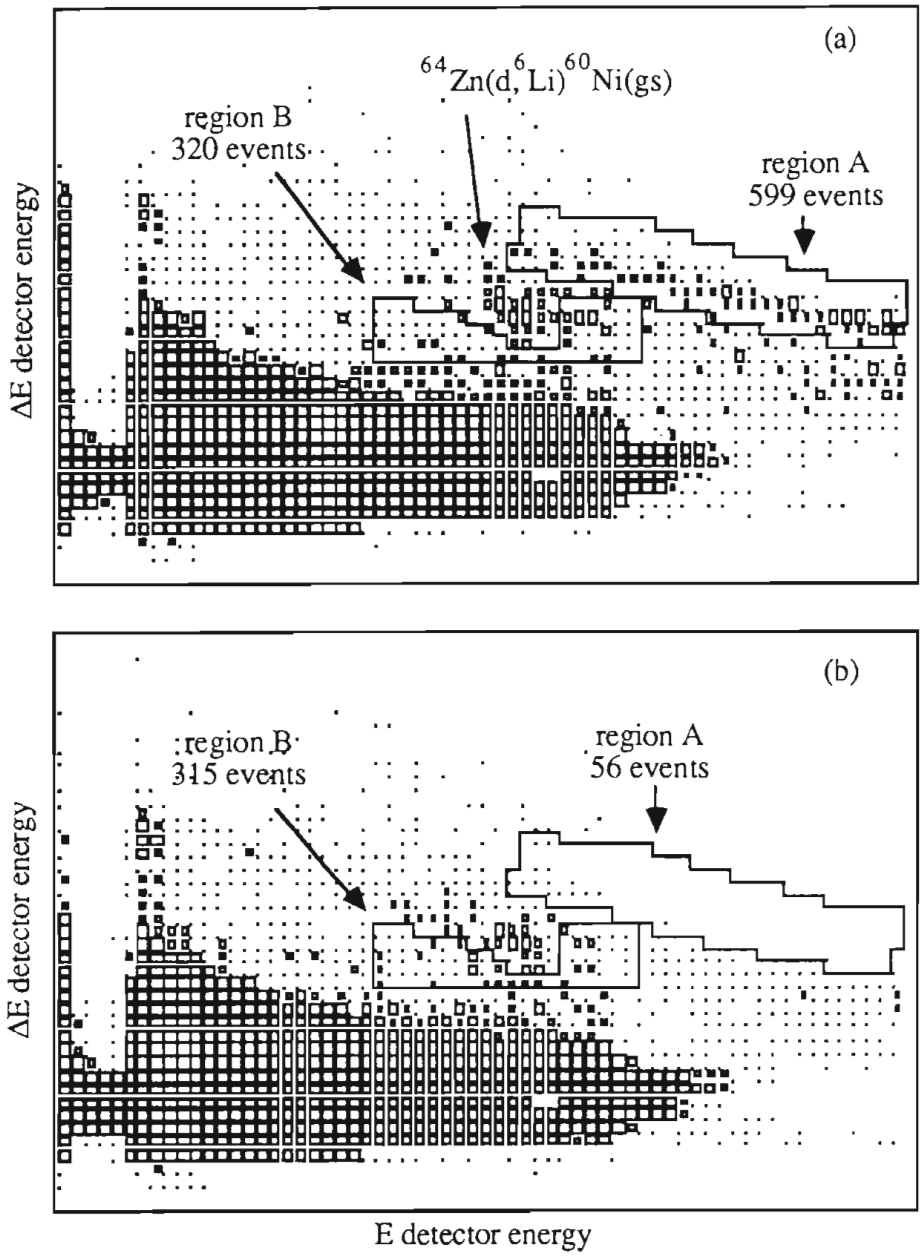

Figure 3.3.5 : Reduction of Router Pile-up Using the Router Pile-up Bit. Parts (a) and (b) are plotted on the same scale and display data obtained under nearly identical conditions, except that the router pile-up bit was employed while acquiring the data of 3.3.5(b). Use of this bit eliminated 93% of the events in region A but did not affect the count rate in region B. The data were taken at $\theta_{lab} = 45°$ in October, 1985.

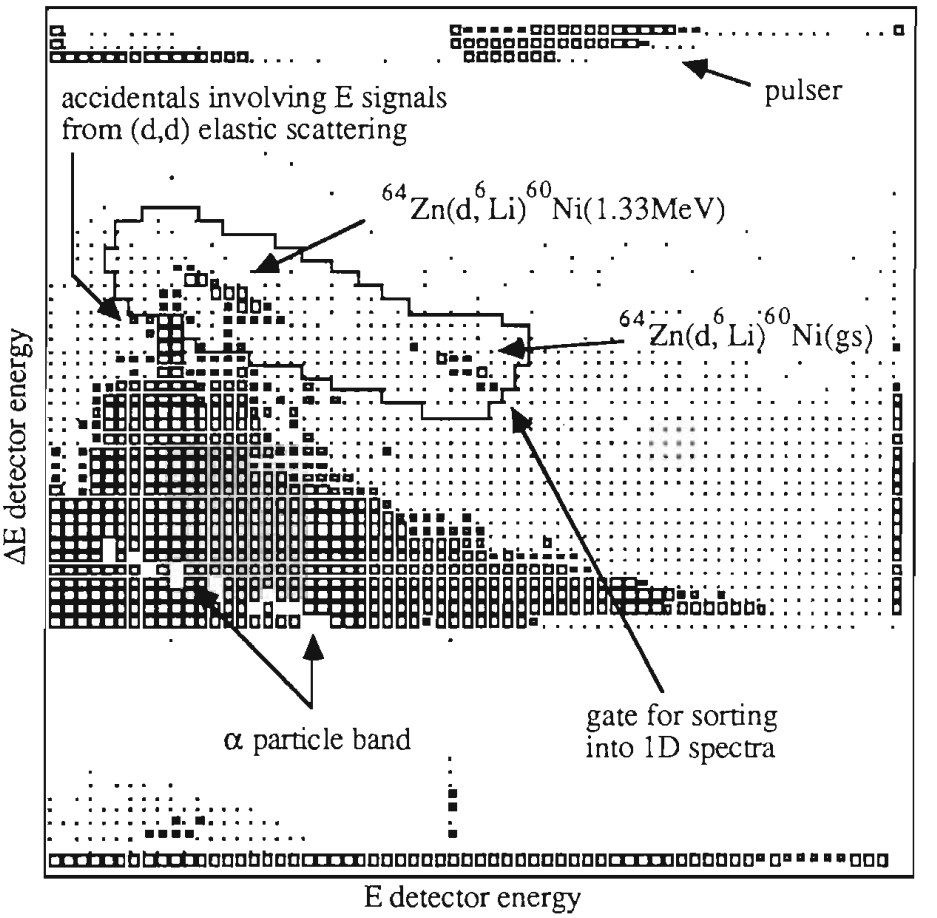

Figure 3.3.6(a) : The Effects of Fast Coincidence Timing. Shown above is the E-ΔE spectrum of the MAY86 25° telescope before imposing a 17 ns coincidence requirement on the E and ΔE signals. A vertical band of accidental coincidence events involving E signals from (d,d) elastic scattering can be seen just below the ^{64}Zn(d,^{6}Li)^{60}Ni(1.33 MeV) peak. Other background events appear above and to the right of the α particle band. All events within the gate shown were sorted into one-dimensional spectra, one of which is displayed with the dotted curve of Figure 3.3.6(c).

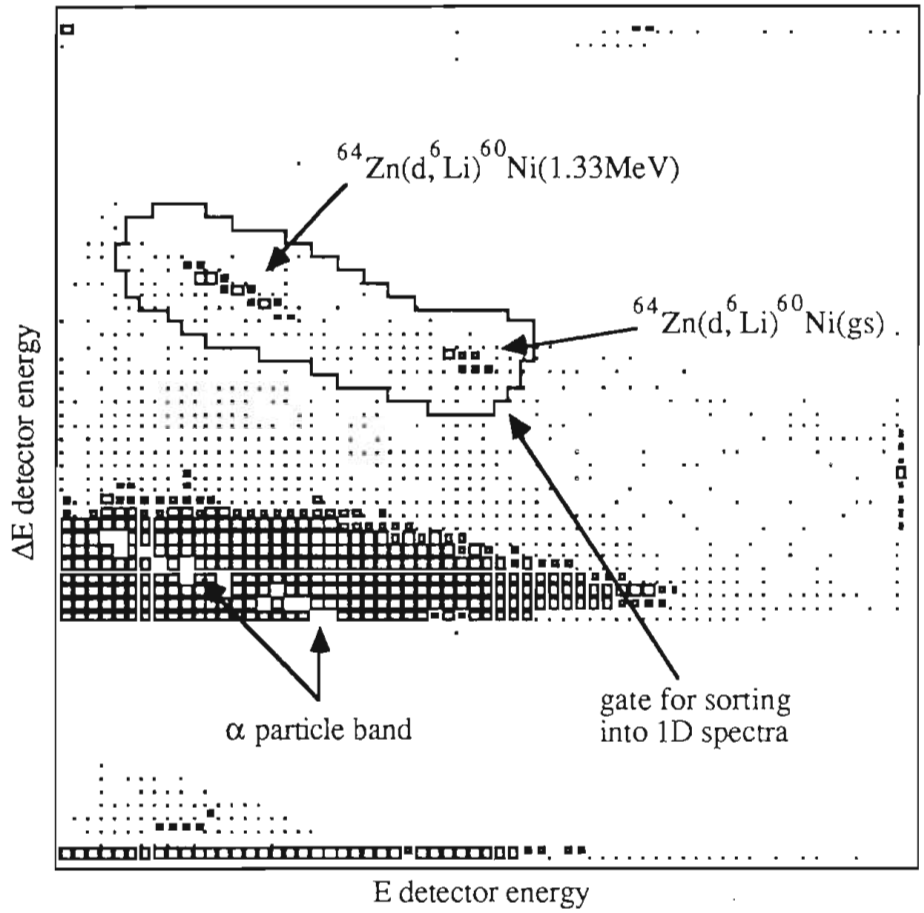

Figure 3.3.6(b) : The same data plotted on the same scale as in Figure 3.3.6(a), except that events were rejected if their E and ΔE signals were separated by more than 17 ns. The gate above is the same as that of Figure 3.3.6(a), and a resulting one-dimensional spectrum is shown with the solid line of Figure 3.3.6(c). (The region of strong background extending to the right of the α particle band was created by detector pile-up of E signals. To reduce dead time, the lower level discriminator on the E pile-up rejector had been set above the level for E signals from elastically scattered deuterons.)

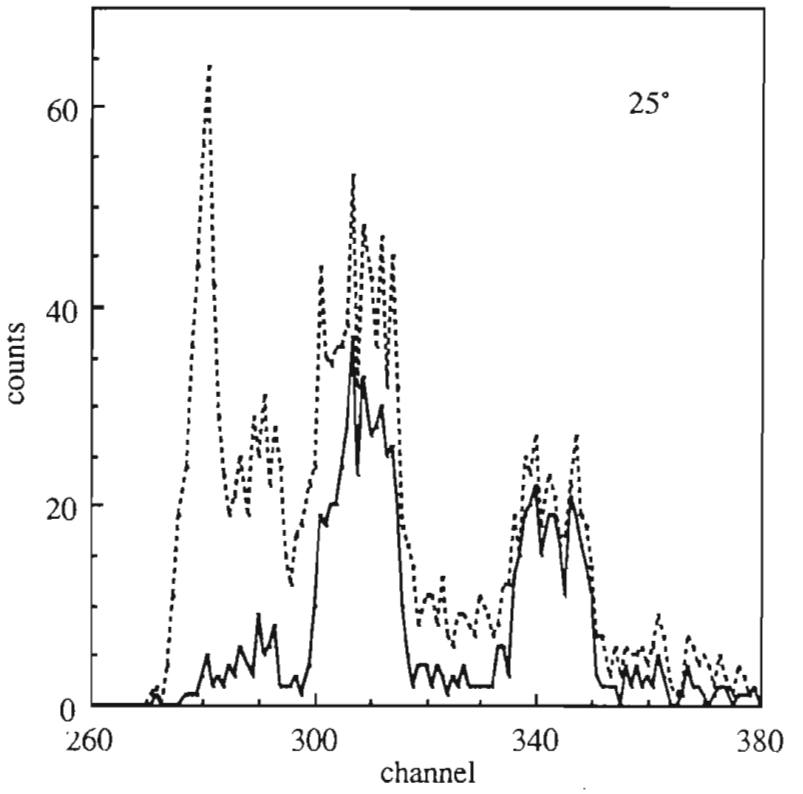

Figure 3.3.6(c) : The dotted and solid lines are one-dimensional spectra associated with the 2D gates of Figures 3.3.6 (a) and (b), respectively.

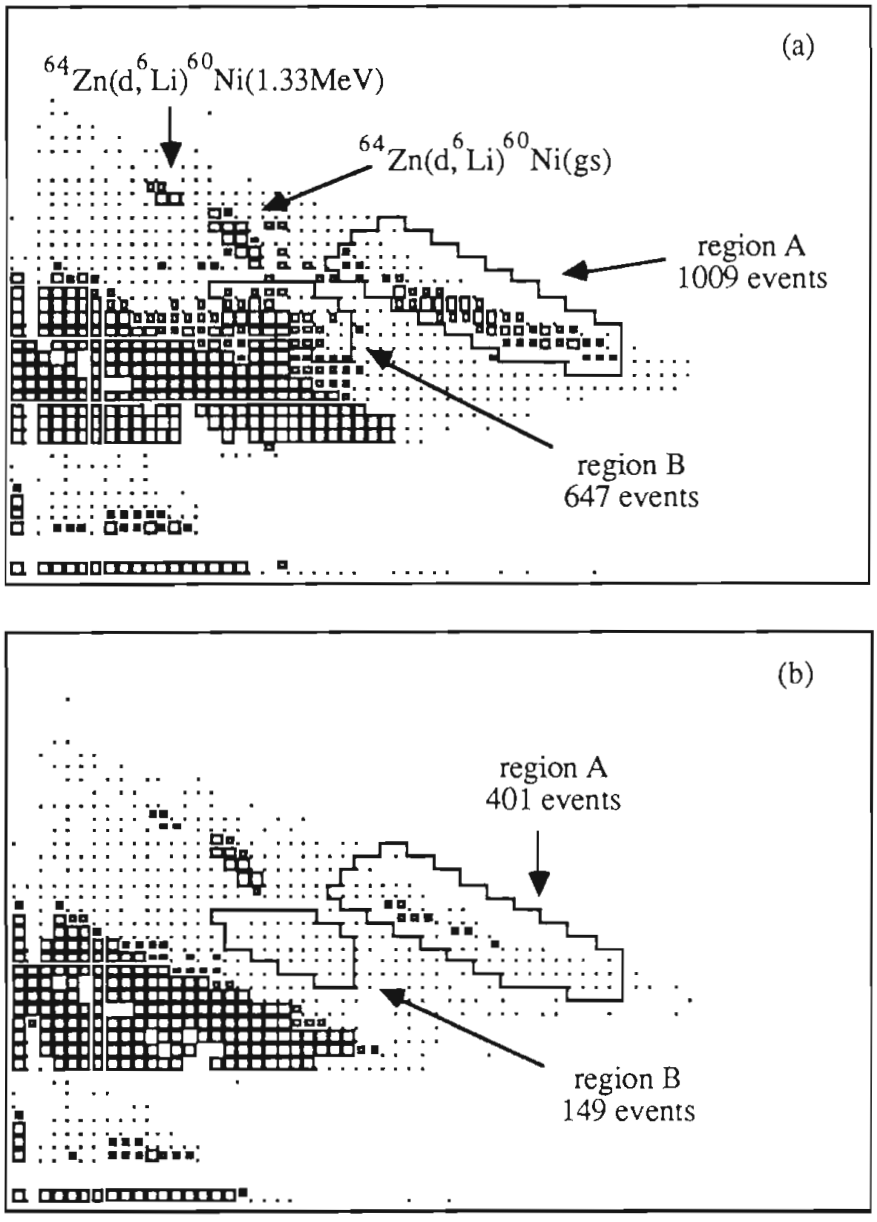

Figure 3.3.7 : The Influence of Fast Coincidence Timing on Pile-up. The spectra are from the MAY86 75° telescope before and after application of a 29 ns coincidence requirement between E and ΔE detectors. This coincidence requirement apparently attenuated pile-up, removing 60% and 73% of the events from regions A and B, respectively.

Because sources of E and ΔE signals were uncorrelated, accidental coincidences should have produced rectangular regions of background whose boundaries were parallel to the E and ΔE axes of the 2-D spectra. Region A of Figure 3.3.1 does *not* have such a shape but instead has a contour similar to that of the α band, suggesting that accidentals did not contribute strongly to this region. Many regions of Figure 3.3.6(a) do have a more nearly rectangular shape. Very prominent is a band of background extending upward toward the second ^{6}Li peak. The E signals for this background were from elastically scattered deuterons. The ΔE signals may have resulted from pile-ups of two α particles.

Also because the sources of E and ΔE signals were uncorrelated, the number of accidentals could be reduced by shortening the time window during which both signals were required to arrive. The spectrum of Figure 3.3.6(a) was obtained with the requirement that E and ΔE signals arrive within one μs of each other. Figure 3.3.6(b) shows a spectrum of the same data after a 17 ns coincidence window had been superimposed. The 1-D spectra corresponding to each of the 2-D data areas are shown by the dotted and solid lines of Figure 3.3.6(c). Noise was dramatically reduced by the 17 ns coincidence requirement.

After the experiment, the data were resorted using wider coincidence windows. This analysis confirmed that the 17 ns window had not thrown away any true ^{6}Li events.

Figures 3.3.7 (a) and (b) display a 2-D spectrum from the MAY86 75° telescope before and after application of a 29 ns coincidence requirement.. The shape of region A implies that it was dominated by pile-ups. Furthermore, this telescope's ΔE pile-up rejector was not functioning, and such background did not occur in the same region of the other five telescopes, which had working ΔE pile-up rejectors. Also, region B, where the 75° telescope had much worse background than any other telescope, may have been dominated by pile-ups. The fast coincidence requirement removed 60% and 77% of the

events in regions A and B, respectively. This was an interesting effect, since one might not expect a coincidence requirement between E and ΔE detectors to reduce detector (or router) pile-ups. However, pile-ups may have shifted the timing of pulses and thus allowed the fast coincidence circuitry to discriminate against them.

Clean Targets

Because the above types of noise depended on two uncorrelated particles striking detectors in coincidence, the number of background events should have decreased quadratically with the number of particles produced in the scattering chamber. This principle was tested by halving the beam current, and we found that background was reduced by a factor of about four. Hence, limiting the production of α particles and other light particles was a very effective method of background attenuation. The production of lighter particles was minimized by limiting the presence in the target of nuclei other than ^{64}Zn. The spectra of Figure 3.3.2 were obtained with a target containing 640 μg/cm^2 of ^{64}Zn, 75 μg/cm^2 of Al, and 4 μg/cm^2 of C. (Layers of C and Al were required to produce durable targets.) Though these layers were thin compared to the ^{64}Zn layer, C and Al have much higher (d,α) cross-sections. Crude measurements indicated that C and Al were producing half of the α particles, suggesting that removing these layers would reduce background by 75%! As detailed in Section 3.1, thicknesses of C and Al (or Cu) were greatly reduced in the targets utilized to acquire the data of Figures 3.3.3 and 3.3.4, and this reduction of extraneous materials was the primary reason for the improved quality of these spectra.

Veto Detectors

In our early efforts to understand and control background, we studied the use of veto detectors. During the FEB86 run, veto detectors were employed at 30°, 50°, and 80°. These detectors were not used for the MAY86 run.

Veto detectors sat in the telescope immediately behind the E detectors. The veto TSCA was connected in anti-coincidence to the 1-μs coincidence box, so that when a particle struck the veto detector, no coincidence box output was generated. The E-ΔE pair of detectors stopped all ^{6}Li nuclei but allowed many lighter particles to reach the veto detector. For example, a 27μ ΔE and 30μ E pair of detectors would not stop α particles with energies greater than 8.5 MeV or protons with energies greater than 2.2 MeV. The veto system reduced background to the extent that events including these more energetic light particles constituted the background.

Veto detectors might have removed some of the pile-up that populated regions A and B of the 2-D spectra, but not that near the ^{6}Li peaks. Consider again a 27μ ΔE detector. In such a detector, ^{6}Li particles from the ^{64}Zn(d,^{6}Li) reaction at E_d = 16.4 MeV deposited about 10 MeV. Alphas that were just energetic enough to penetrate the ΔE generated the maximum α particle ΔE signal, about 5 MeV. However, for the pile-up of two α particles to have been vetoed, at least one of the particles had to also penetrate the E detector and enter the veto detector. This more energetic α would have produced a ΔE amplitude well below 5 MeV, and the piled-up ΔE signal would have fallen short of the ^{6}Li region. In general, veto detectors were ineffectual against the largest (and therefore most troublesome) ΔE pile-up signals. Of course, for an experiment with different kinematic and energy loss considerations, these detectors might help.

In the case of accidental coincidences, E and ΔE signals were derived from different particles. Probable sources of large ΔE signals were enumerated above, and none of these sources were likely to have created veto pulses. However, the veto system was an effective means of removing E signals comparable to those of ^{6}Li. The pre-fast-coincidence 25° spectrum of Figure 3.3.6 apparently includes many accidentals, such as those involving the E signal from (d,d) elastic scattering. A veto detector might have

retrenched this noise. Such background was not observed for the 30° telescope, which had a veto (but which also had fast coincidence).

Chapter 4

Analysis of the $^{64}Zn(\vec{d},^{6}Li)$ Data

In Section 3.1, we detailed how the eight steps of $^{64}Zn(\vec{d},^{6}Li)$ data required by Tonsfeldt's mode-1 measurement scheme were taken. Tonsfeldt has developed equations for obtaining cross-sections and analyzing powers from these data. [Ton80] However, a slightly modified version of these equations has been employed to extract cross-sections and analyzing powers from all mode-1 measurements performed at TUNL since 1986, including the $^{64}Zn(\vec{d},^{6}Li)$ data from the FEB86 and MAY86 runs. These modifications resulted in more precise determinations of A_{xx} without significantly decreasing the precision of other analyzing power measurements. In Section 4.1, reasons for and consequences of these modifications are elucidated. The $^{64}Zn(\vec{d},^{6}Li)$ cross-sections and analyzing powers calculated using this modified set of equations are presented in Section 4.2.

4.1 Modifications to the Tonsfeldt Measurement Scheme

Table 4.1.1 indicates the spin direction, spin state, and chamber orientation during each step of the mode-1 measurement scheme. When the chamber is oriented horizontally, the terms L_1, R_1, L_2, and R_2 are measured. L_1 is the geometric mean of state-1, spin-up counts in the left detector and state-1, spin-down counts in the right detector. The other three quantities are defined in a similar fashion. The terms U_1, D_1, U_2, and D_2 are obtained during the four chamber-vertical steps. Here D_2 stands for the geometric mean of state-2, spin-up counts in the down detector and state-2, spin-down counts in the up detector. Similar definitions apply to U_1, D_1, and U_2. [Ton80]

Data Step	Spin Direction	Spin State	Chamber Orientation
1	up	1	H
2	down	1	H
3	down	2	H
4	up	2	H
5	up	2	V
6	down	2	V
7	down	1	V
8	up	1	V

Table 4.1.1 : Data Acquisition Steps in Tonsfeldt's Mode-1 Measurement Scheme.

Scheme	ΔA_{yy}	ΔA_{zz}	ΔA_{xx}
Tonsfeldt	1	$\sqrt{2}$	$\sqrt{3}$
Tonsfeldt-A	1	$\sqrt{2}$	1

Table 4.1.2 : Relative Errors for the Tonsfeldt and the Tonsfeldt-A Measurement Schemes When R_{68} Is Excluded.

Scheme	ΔA_y	ΔA_{yy}	ΔA_{zz}	ΔA_{xx}
Tonsfeldt	0.0563	0.062	0.117	0.132
Tonsfeldt-A	0.0565	0.077	0.112	0.081
Tonsfeldt-B	0.0567	0.085	0.108	0.067

Table 4.1.3 : Errors Obtained for the 73.3° Telescope Using the Tonsfeldt, Tonsfeldt-A, and Tonsfeldt-B Measurement Schemes.

From these eight measured quantities Tonsfeldt forms eight independent sums and differences. These are :

$$(L_1\text{-}R_1) \equiv (L\text{-}R)_1$$

$$(L_1\text{+}R_1) \equiv (L\text{+}R)_1$$

$$(U_1\text{-}D_1) \equiv (U\text{-}D)_1 = 0 \quad \text{for } \beta = 90^\circ \ \dagger$$

$$(U_1\text{+}D_1) \equiv (U\text{+}D)_1$$

$$(L_2\text{-}R_2) \equiv (L\text{-}R)_2 \cong 0 \quad \text{since } P_z^{(2)} \cong 0$$

$$(L_2\text{+}R_2) \equiv (L\text{+}R)_2$$

$$(U_2\text{-}D_2) \equiv (U\text{-}D)_2 = 0 \quad \text{for } \beta = 90^\circ$$

$$(U_2\text{+}D_2) \equiv (U\text{+}D)_2$$

As indicated above, three of the differences are more or less zero. Left are five independent, experimentally determined quantities from which many ratios can be formed, only four of which are independent. Tonsfeldt considers the following six ratios.

$$R_{12} = \frac{(L\text{-}R)_1}{(L\text{+}R)_1} = \frac{\frac{3}{2} P_{zz}^{(1)} A_y}{1 + \frac{1}{2} P_{zz}^{(1)} A_{yy}} \qquad (4.1.1)^{\dagger\dagger}$$

---

† β is the angle between the beam and the deuteron spin axis. $\beta = 90^\circ$ for all mode-1 steps. [Ton80]

†† This equation assumes that $P_{zz}^{(1)} = P_z^{(1)}$. [Chapter 3]

$$R_{24} = \frac{(L+R)_1}{(U+D)_1} = \frac{1 + \frac{1}{2} P_{zz}^{(1)} A_{yy}}{1 + \frac{1}{2} P_{zz}^{(1)} A_{xx}} \qquad (4.1.2)$$

$$R_{68} = \frac{(L+R)_2}{(U+D)_2} = \frac{1 + \frac{1}{2} P_{zz}^{(2)} A_{yy}}{1 + \frac{1}{2} P_{zz}^{(2)} A_{xx}} \qquad (4.1.3)$$

$$R_{26} = \frac{(L+R)_1}{(L+R)_2} = \frac{1 + \frac{1}{2} P_{zz}^{(1)} A_{yy}}{1 + \frac{1}{2} P_{zz}^{(2)} A_{yy}} \qquad (4.1.4)$$

$$R_{48} = \frac{(U+D)_1}{(U+D)_2} = \frac{1 + \frac{1}{2} P_{zz}^{(1)} A_{xx}}{1 + \frac{1}{2} P_{zz}^{(2)} A_{xx}} \qquad (4.1.5)$$

$$R = \frac{(L+R+U+D)_1}{(L+R+U+D)_2} = \frac{1 - \frac{1}{4} P_{zz}^{(1)} A_{zz}}{1 - \frac{1}{4} P_{zz}^{(2)} A_{zz}} \qquad (4.1.6)$$

R_{12} is the only ratio containing $(L\text{-}R)_1$ and is therefore independent of the other ratios shown. Of the remaining five ratios, two must be eliminated.

For two reasons, Tonsfeldt eliminates R_{24} in favor of R_{68}.

1) A_{xx} and A_{yy} are weighted by $P_{zz}^{(2)}$ in R_{68} whereas they are weighted by $P_{zz}^{(1)}$ in R_{24}. Since $P_{zz}^{(2)} \cong (2)\ |P_{zz}^{(1)}|$, R_{68} is more sensitive to these TAP than R_{24}.

2) R_{24} is susceptible to vector contamination since $P_z^{(1)}$ is large.

Next, Tonsfeldt eliminates R_{48} in favor of R. In the modified scheme introduced below, R_{48} is retained while R is eliminated. This modification dramatically improves the precision of A_{xx} measurements without strongly affecting the precision for the other analyzing powers.

Tonsfeldt's 8-step method for calculating analyzing powers other than A_{xz} is diagramed in Figure 4.1.1; Figure 4.1.2 indicates a modified scheme, which we designate Tonsfeldt-A. Both methods use R_{26} to obtain A_{yy}. Tonsfeldt's mode-1 approach uses R to determine A_{zz}, and A_{xx} is then calculated from A_{yy} and A_{zz}. The Tonsfeldt-A scheme obtains A_{xx} from R_{48} and then determines A_{zz} from A_{yy} and A_{xx}. (For simplicity, the effect of the ratio R_{68} is ignored for the moment.) The Tonsfeldt-A scheme yields comparable or smaller error bars on all TAP because R_{48} is much more sensitive to A_{xx} than R is to A_{zz}.

The error in A_{yy} from the uncertainty in R_{26} is :

$$\Delta A_{yy} = \frac{dA_{yy}}{dR_{26}} \Delta R_{26}, \qquad (4.1.7)$$

and the error in A_{zz} from R is :

$$\Delta A_{zz} = \frac{dA_{zz}}{dR} \Delta R \qquad (4.1.8)$$

From expression (4.1.4) for R_{26} one can obtain :

$$A_{yy} = \frac{2\,(R_{26}-1)}{(P_{zz}^{(1)} - R_{26}\,P_{zz}^{(2)})} \qquad (4.1.9)$$

Differentiating gives :

$$\frac{dA_{yy}}{dR_{26}} = \frac{2\,(P_{zz}^{(1)} - P_{zz}^{(2)})}{(P_{zz}^{(1)} - R_{26}\,P_{zz}^{(2)})^2} \qquad (4.1.10)$$

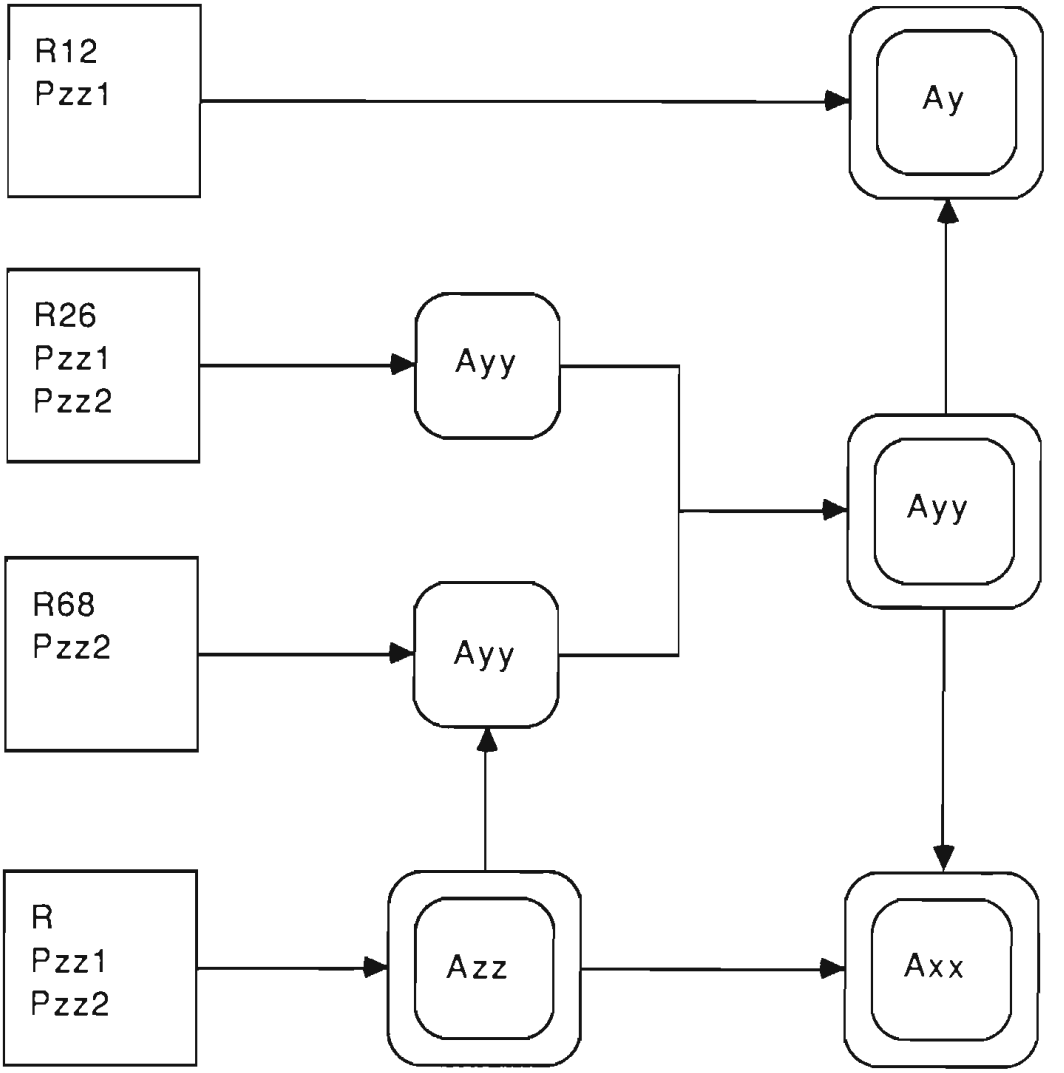

Figure 4.1.1 : Tonsfeldt's Mode-1 Measurement Scheme.

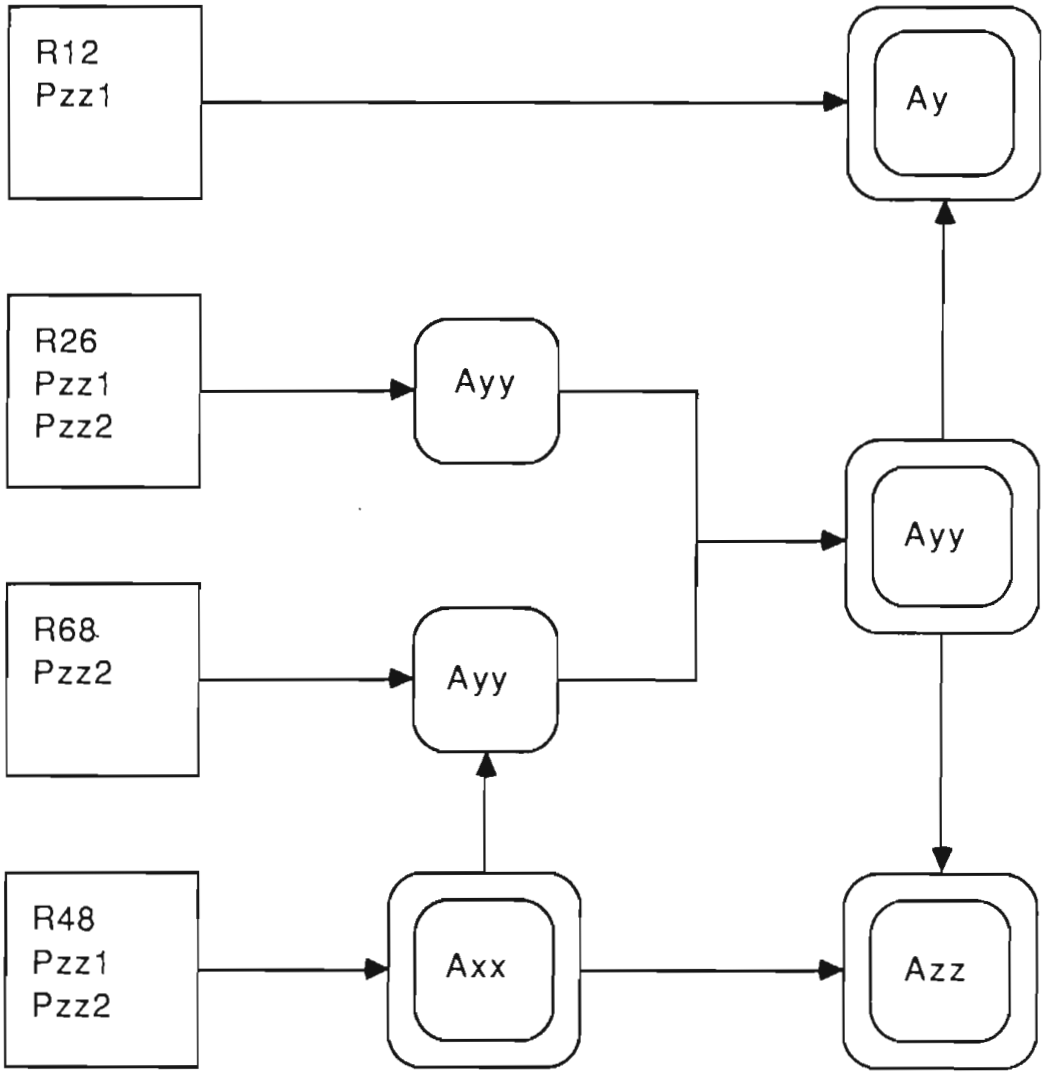

Figure 4.1.2 : The Tonsfeldt-A Measurement Scheme.

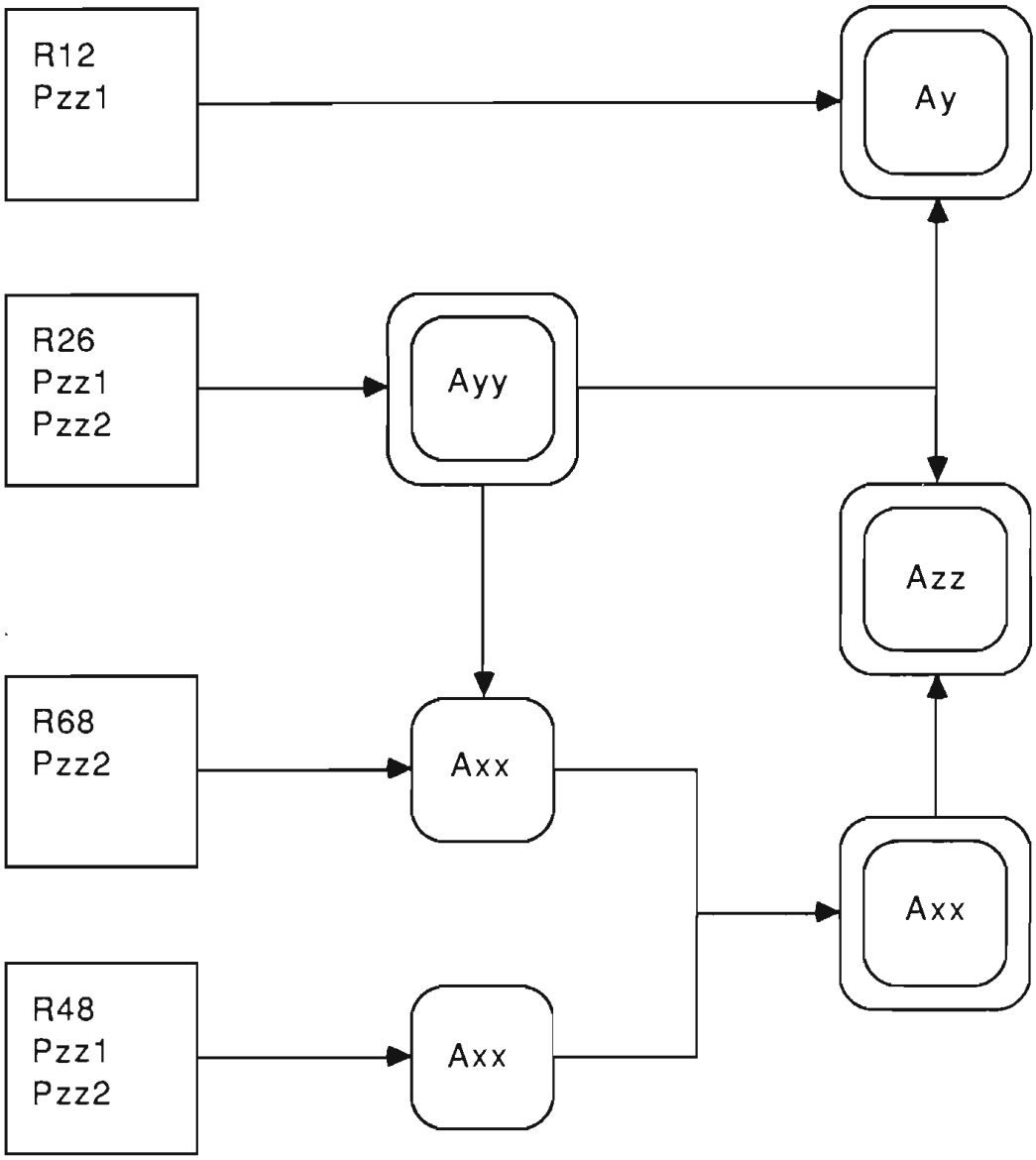

Figure 4.1.3 : The Tonsfeldt-B Measurement Scheme. This method was employed to analyze the $^{64}Zn(\vec{d},^{6}Li)$ data.

Likewise, for A_{zz} and R :

$$A_{zz} = \frac{4\,(1-R)}{(P_{zz}^{(1)} - R\,P_{zz}^{(2)})} \qquad (4.1.11)$$

$$\frac{dA_{zz}}{dR} = \frac{-4\,(P_{zz}^{(1)} - P_{zz}^{(2)})}{(P_{zz}^{(1)} - R\;P_{zz}^{(2)})^2} \qquad (4.1.12)$$

If, for the sake of insight, one ignores the difference between the denominators in expressions (4.1.10) and (4.1.12), one can see that A_{zz} is about twice as sensitive to variations in R as A_{yy} is to variations in R_{26}. On the other hand, R is formed from approximately twice as many counts as R_{26}, so one expects ΔR to be smaller than ΔR_{26} by a factor of about $\sqrt{2}$. Combining these results yields :

$$\Delta A_{zz} = \sqrt{2}\;\Delta A_{yy} \qquad \text{(Tonsfeldt)}$$

This is of course only a rough estimate. Since $A_{xx} = -(A_{yy} + A_{zz})$, one also obtains :

$$\Delta A_{xx} = \sqrt{\Delta A_{yy}^2 + \Delta A_{zz}^2} = \sqrt{3}\;\Delta A_{yy} \qquad \text{(Tonsfeldt)}$$

Consider the Tonsfeldt-A scheme, again ignoring the contribution from R_{68}. Here, A_{xx} has the same relation to R_{48} that A_{yy} has to R_{26}. One can immediately write :

$$\Delta A_{xx} = \Delta A_{yy} \qquad \text{(Tonsfeldt-A)}$$

Since $A_{zz} = -(A_{yy} + A_{xx})$,

$$\Delta A_{zz} = \sqrt{\Delta A_{yy}^2 + \Delta A_{xx}^2} = \sqrt{2}\;\Delta A_{yy} \qquad \text{(Tonsfeldt-A)}$$

Table 4.1.2 compares results of the two methods when R_{68} is excluded. The methods are equally sensitive to A_{yy} and A_{zz}, while the Tonsfeldt-A approach is far more sensitive to A_{xx}.

The first two rows of Table 4.1.3 give the analyzing power errors obtained by the Tonsfeldt scheme and the modified scheme for the $\theta_{cm} = 73.3°$ detector in the FEB86 run. The third row shows the error bars obtained by a third scheme which will be discussed below. These calculations *include* contributions from R_{68}. As predicted by the above simple argument, the two methods are equally sensitive to A_{zz}. The ΔA_{zz} values differ by less than 5%. Also as predicted above, the Tonsfeldt-A scheme reduces the A_{xx} error by a factor of 1.63, which is very close to $\sqrt{3}$.

Once A_{xx}, A_{yy}, or A_{zz} is determined by one of the experimental ratios, R_{68} can be used to improve the precision of one of the two remaining TAP. In Tonsfeldt's scheme, A_{zz} and R_{68} are used to obtain a value for A_{yy}. This value of A_{yy} is combined with the value of A_{yy} determined from R_{26} to give a more precise A_{yy} measurement. (Figure 4.1.1.) Because of this contribution from R_{68}, the ΔA_{yy} in Table 4.1.3 is smaller relative to ΔA_{xx} and ΔA_{zz} than predicted by the above simple argument. The Tonsfeldt-A scheme uses A_{xx} and R_{68} to improve the value of A_{yy}. (Figure 4.1.2) At least for this 73.3° detector, A_{xx} and R_{68} do not do as good a job of determining A_{yy} as do A_{zz} and R_{68}. Hence ΔA_{yy} is larger in the modified scheme than in the Tonsfeldt scheme. The generality of this effect has not been investigated.

One can further reduce the A_{xx} error by using R_{68} to improve the A_{xx} measurement rather than the A_{yy} measurement. This scheme is designated Tonsfeldt-B and is diagramed in Figure 4.1.3. The third row of Table 4.1.3 contains the errors for the Tonsfeldt-B scheme.

One can see from Table 4.1.3 that the three schemes are about equally sensitive to A_y. A_{yy} is needed to obtain A_y from R_{12}, and since Tonsfeldt's original scheme yields smaller A_{yy} errors, one might think that it would be more precise in determining A_y. It is, but only very slightly, because A_y is only weakly dependent on A_{yy}.

The preceding paragraphs have analyzed the sensitivity of Tonsfeldt's scheme, and two modified versions of it, to the analyzing powers for deuteron induced reactions. The modified schemes yield much smaller errors for A_{xx} while producing comparable errors for A_y and A_{zz} and only slightly larger errors for A_{yy}.

One-step, DWBA calculations indicate that, for the ^{64}Zn(d,^{6}Li) reaction at about 16 MeV, A_{xx} is strongly influenced by the D-wave admixture in the ^{6}Li ground state. Accordingly, the Tonsfeldt-B scheme was used to analyze our (d,^{6}Li) data. By switching from Tonsfeldt's scheme to the Tonsfeldt-B scheme, the errors for A_{xx} were reduced by a factor of two, which corresponds to a factor of four reduction in the beam time required to measure A_{xx} to a given precision. For the ^{64}Zn(d,^{6}Li) experiment, a factor of four reduction in beam time was an important improvement.

In general, there is no one best scheme for measuring all of the analyzing powers. Different analyzing powers are sensitive to different aspects of nuclear structure and nuclear reaction mechanisms. For a given experiment, the best scheme is one that optimizes the precision of those analyzing powers that are most responsive to the nuclear physics issues under study. If A_{yy} and A_{zz} are the important analyzing powers, the Tonsfeldt scheme is slightly more sensitive to these quantities than are the modified schemes. The modified schemes do much better with other commonly used pairs of analyzing powers, such as A_{xx} and A_{yy} or T_{20} and T_{22}.

Optimizing precision is an important but not a critical consideration for most experiments. For example, in (d,d) scattering or (d,^{3}He) reactions the count rate is fairly high; modifying the calculation programs for each of these experiments is hardly worth the effort. A compromise scheme that works well for all of the commonly used sets of analyzing powers is needed. One of the modified schemes is a much better choice for this

compromise, because, roughly speaking, these schemes are as good or better than Tonsfeldt's original scheme for all of the commonly used pairs of TAP.

4.2 Results of Analysis of the ^{64}Zn(d,^{6}Li) Data

Cross-sections and analyzing powers extracted from the FEB86 and MAY86 ^{64}Zn($\vec{d}$,^{6}Li) data via the Tonsfeldt-B scheme are presented in Figures 4.2.1 and 4.2.2 and in Tables C-1 and C-2 of Appendix C.

The analyzing powers A_y and A_{yy} are absent at $\theta_{lab} = 65^{\circ}$ because of a bad E detector during the chamber horizontal portion of the MAY86 run.

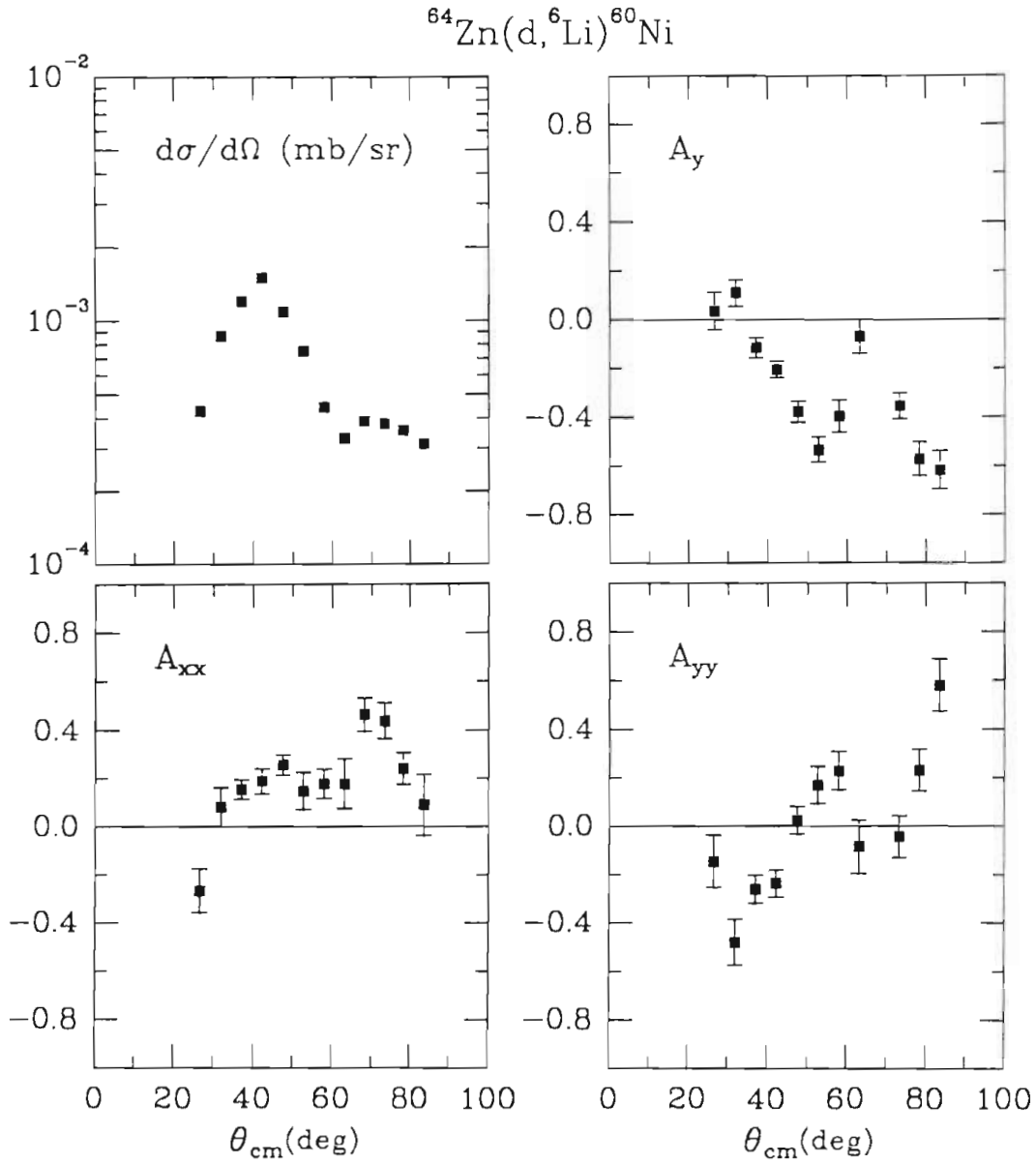

Figure 4.2.1 : Measured Cross-sections and Analyzing Powers for the ^{64}Zn(d,^{6}Li) Reaction Forming the ^{60}Ni Ground State.

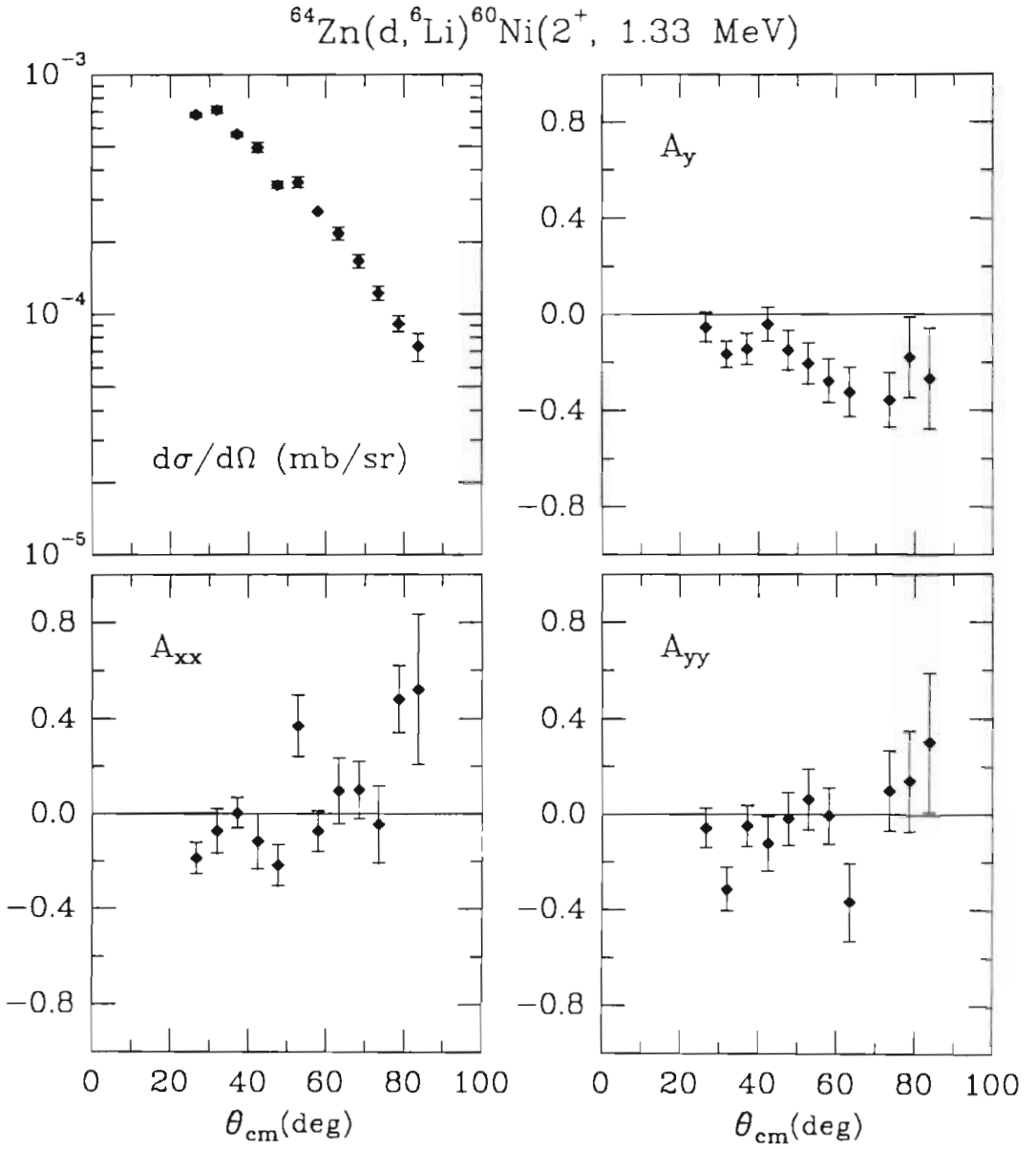

Figure 4.2.2 : Measured Cross-sections and Analyzing Powers for the ^{64}Zn(d,^{6}Li) Reaction Forming the $I^{\pi} = 2^{+}$, 1.33 MeV First Excited State of ^{60}Ni.

Chapter 5

Elastic Scattering Data and Optical Model Potentials

In Chapter 8, the ^{64}Zn(d,^{6}Li) reaction is analyzed within the coupled-channel Born approximation (CCBA) formalism. This formalism requires the use of distorted waves in both the incoming d-^{64}Zn and the outgoing ^{6}Li-^{60}Ni channels. These waves are solutions to the Schrodinger equation in the presence of potentials which depend on the spins of the two nuclei composing the channel and the relative coordinates of these nuclei but not on internal coordinates of the nuclei. Such interactions are referred to as optical model potentials. [Gle83]

Measurements of ^{64}Zn($\vec{d}$,d) and ^{60}Ni(^{6}Li,^{6}Li) scattering are described in this chapter. Deuteron optical model potentials are obtained by moderately adjusting the global parameters of Daehnick et al. [Dae80] such that the ^{64}Zn($\vec{d}$,d) data are well reproduced. In Chapter 7, interactions for ^{6}Li scattering are generated from a folding model, and the cross-sections calculated using those interactions are compared with the measured cross-sections discussed here.

5.1 ^{64}Zn($\vec{d}$,d) Scattering

Experimental Procedures

Differential cross-sections, A_y, A_{xx}, and A_{yy} were obtained for ^{64}Zn($\vec{d}$,d) scattering to the ground state and the $I^{\pi} = 2^{+}$, 0.998 MeV, first excited state of ^{64}Zn in 5°

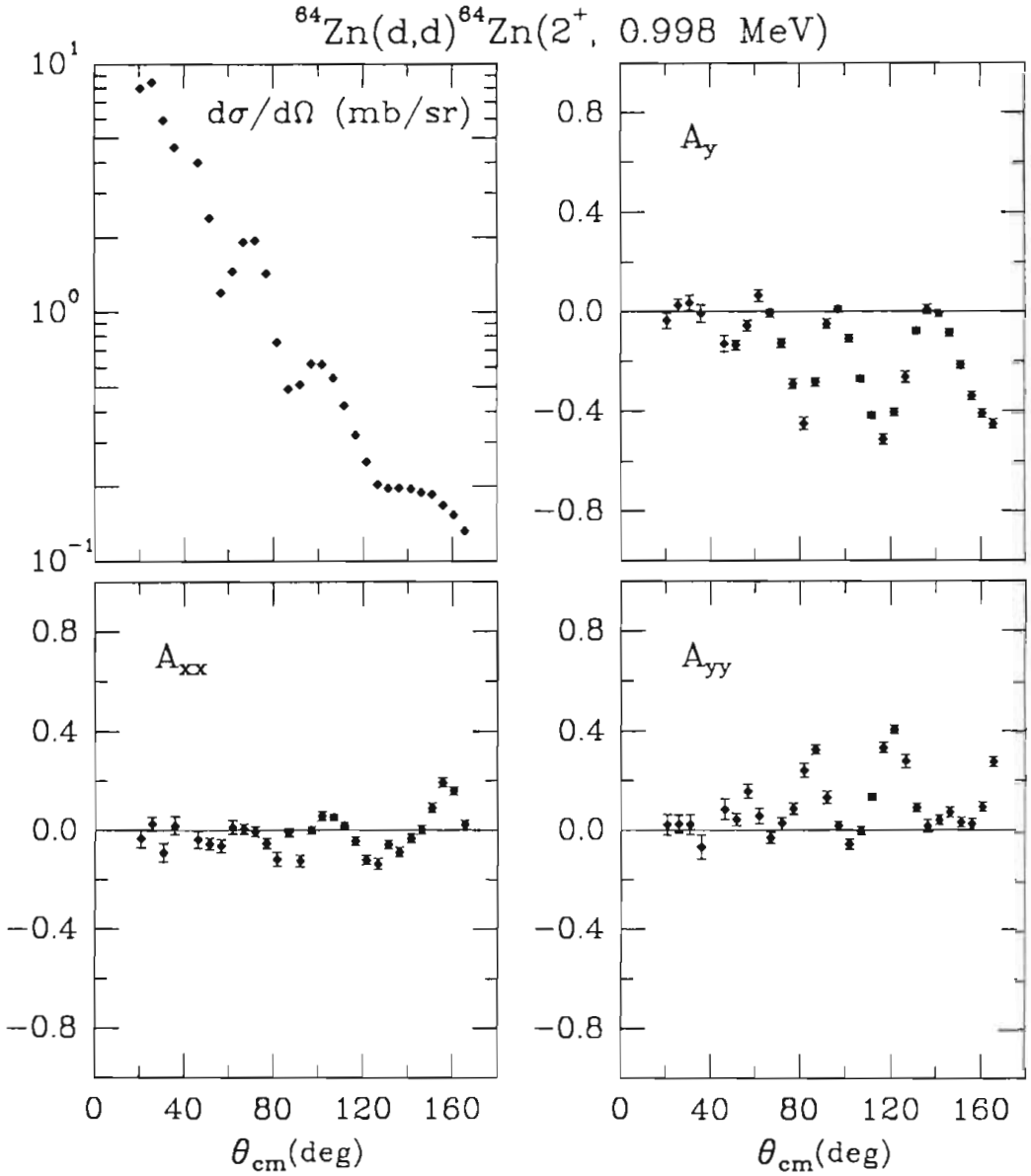

Figure 5.1.2 : Measured Cross-sections and Analyzing Powers for ^{64}Zn(d,d') Scattering Forming the $I^{\pi} = 2^{+}$, 0.998 MeV First Excited State of ^{64}Zn.

determinations of N were not fully independent, since the data of [Chi74] were utilized in developing the global optical model potential of [Dae80].

The data of Figures 5.1.1 and 5.1.2 and Tables C-3 and C-4 assume a renormalization of 0.52 for the cross-section. This value was obtained by the fitting procedure described below. Possible sources of the error in the originally measured cross-sections are discussed in Appendix B.

Determination of Deuteron Optical Model Potentials

The d-^{64}Zn interaction was assumed to have the form :

$$\begin{aligned} V(r) \;=\; & V_C(r) + -V_0\, f(r,r_0,a_0) \;+ \\ & -i\, W_S\, f(r,r_{WS},a_{WS}) \;+\; 4\, i\, a_{WD}\, W_D \frac{d}{dr} f(r,r_{WD},a_{WD}) \;+ \\ & 2\, V_{SO} \frac{1}{r} \frac{d}{dr} f(r,r_{SO},a_{SO})\, \mathbf{L}\cdot\mathbf{S} \;+ \\ & 2\, i\, W_{SO} \frac{1}{r} \frac{d}{dr} f(r,r_{WSO},a_{WSO})\, \mathbf{L}\cdot\mathbf{S} \end{aligned} \qquad (5.1.3)$$

where the geometrical factor $f(r,r_X,a_X)$ is :

$$f(r,r_X,a_X) = \frac{1}{1 + \exp \dfrac{r - (r_X \cdot A^{1/3})}{a_X}} \qquad (5.1.4)$$

The Coulomb interaction is specified by $V_C(r)$. The next three terms are volume real, volume imaginary, and surface imaginary central potentials, and the last two terms are real and imaginary spin-orbit potentials. The **L** and **S** represent the orbital angular momentum and spin of the projectile. The mass of the target nucleus is given by A.

without and with an imaginary spin-orbit potential are referred to as the TUNL-A and TUNL-B parameters, respectively. In Figure 5.1.1, the measured cross-sections and analyzing powers are compared with those calculated assuming the TUNL-B parameters and the parameters of [Dae80]. Also shown are values of A_{yy} and A_{xx} calculated using the TUNL-A potentials.

The present optical model analysis indicates a strong preference for a non-zero imaginary spin-orbit potential. The optical model parameters were varied to minimize χ^2 for $d\sigma/d\Omega$ and A_y only; including an imaginary spin-orbit potential lowered χ^2 considerably for both of these observables. The TUNL-B parameters also provided a fairly good fit to A_{yy} and A_{xx}, apparently because this set included an imaginary spin-orbit potential, since the TUNL-A potentials did not reproduce A_{yy} and A_{xx} much better than did the potentials of [Dae80].

5.2 ^{60}Ni(^{6}Li,^{6}Li) Scattering

Cross-sections for ^{60}Ni(^{6}Li,^{6}Li) scattering to the ground state and the $I^\pi = 2^+$, 1.33 MeV, first excited state of ^{60}Ni were measured in 5° steps from θ_{lab} = 20° to 165° in April, 1987.

A beam of unpolarized $^6Li^-$ ions was obtained from the TUNL heavy ion sputter source. The terminal voltage of the TUNL FN tandem Van de Graaff electrostatic accelerator was set such that ^{6}Li ions stripped into their 3^+ charge state were accelerated to 14.8 MeV; these ions were then deflected 52° into a scattering chamber.

Beam current on target was taken to be the sum of current striking slits S_3 and current striking a Faraday cup placed in the polarimeter chamber. (Figure 3.1.1) Aluminum cylinders aligned coaxially with the beam and biased to -60 volts were placed just upstream from S_3 and from the Faraday cup to suppress electrons knocked off these

devices by the beam. Current from these sources was wired together and sent directly to the control room. Beam currents on target ranged from 5 to 8 nA.

Scattered ^{6}Li nuclei were detected by two E-ΔE telescopes placed to the left of the beam and separated by 10° and by four, single detectors placed to the right of the beam and also separated by 10°. Ortec silicon, surface-barrier detectors were employed. The L_1 and L_2 ΔE detectors were 18.6 μ and 19.1 μ thick; both E detectors were 300 μ thick. On the right side, detectors R_1 through R_4 were 75 μ, 75 μ, 49.5 μ, and 48.5 μ thick, respectively. Angle settings ranged from 20° to 155° for the L_1 telescope and from 20° to 135° for detector R_1. All back slits were 0.3175 cm x 0.9525 cm and were placed 15.88 cm from the target, giving solid angles of 1.2 msr per telescope or detector and angular acceptances of ±0.57°.

Optical model calculations indicated that for $\theta_{lab} \leq 40°$, ^{60}Ni(^{6}Li,^{6}Li) elastic scattering cross-sections are within 0.2% of Coulomb cross-sections. However, between the angles $\theta_{lab} = 20°$ and $\theta_{lab} = 40°$, cross-sections extracted from detectors R_1 and R_2 increased by about 5% relative to Coulomb cross-sections. (Cross-sections obtained from L_1 and L_2 were very nearly constant relative to Coulomb cross-sections.) These results imply that the true angle between the beam and the right detectors was slightly larger than the nominal angle. For each of the detectors R_1, R_2, L_1, and L_2, a search was performed for the angle shift that would produce the most constant ratio of measured cross-sections to Coulomb cross-sections at the angles $\theta_{lab} \leq 45°$. For R_1, this procedure provided a very definitive result, $\Delta\theta_{lab}(R_1) = +0.34° \pm 0.01°$. Results for R_2 were more ambiguous but were consistent with $\Delta\theta_{lab}(R_2) = +0.34°$. The agreement between measured and Coulomb cross-sections was not significantly enhanced by shifting the angles of L_1 and L_2. Accordingly, an angle shift of $\Delta\theta_{lab} = +0.34°$ was applied to all four right detectors. At each nominal angle, the average angle shift was computed assuming $\Delta\theta_{lab} = +0.34°$ for each right detector and $\Delta\theta_{lab} = 0.0°$ for each left detector.

The measured cross-sections were renormalized so that, on average, the measured elastic scattering cross-sections at $\theta_{lab} \leq 40.2^\circ$ equaled Coulomb cross-sections. Given the nominal values for detector solid angles, the resulting cross-sections implied a target thickness of 323 $\mu g/cm^2$.

The data are shown in Figure 5.2.1 and are tabulated in Appendix C.

At each of the angles $\theta_{lab} \leq 50.2^\circ$, $\theta_{lab} = 60.2^\circ$, and $\theta_{lab} \geq 150.2^\circ$, the elastic scattering data were acquired simultaneously by detectors placed at equal angles to the left and right of the beam. This symmetrical configuration minimized systematic errors that might have been caused by misalignments of the beam. These data points are indicated by squares in Figure 5.2.1. At the remaining angles, elastic scattering data were obtained with, at any given time, a detector placed on one side of the beam only. Diamonds represent these data points. At all angles, statistical errors in the elastic scattering data are smaller than the sizes of the squares and diamonds. All inelastic scattering data points are indicated by diamonds in Figure 5.2.1. Only the $\theta_{lab} = 160.2^\circ$ and 165.2° inelastic data points were measured by symmetrically placed detectors.

The ^{60}Ni target was produced by Varner [Var86] on April 5, 1983. Given the four-year interval between production of the target and acquisition of the (^6Li,^6Li) data, a convincing determination of the isotopic content of this target was desired. For each of the two E-ΔE telescopes, at each measured scattering angle, the channel number of the highest-energy peak was plotted against the kinematically calculated energy for $^{60}Ni(^6Li,^6Li)$ elastic scattering. For each telescope, a straight line was fit to these points. All points fell within 1% of the straight line, indicating that the dependence of channel number on scattering angle was highly consistent with $^{60}Ni(^6Li,^6Li)$ elastic scattering. These linear fits also provided precise energy calibrations of the spectra. Measured energies of the second-highest-energy peak were then determined assuming this

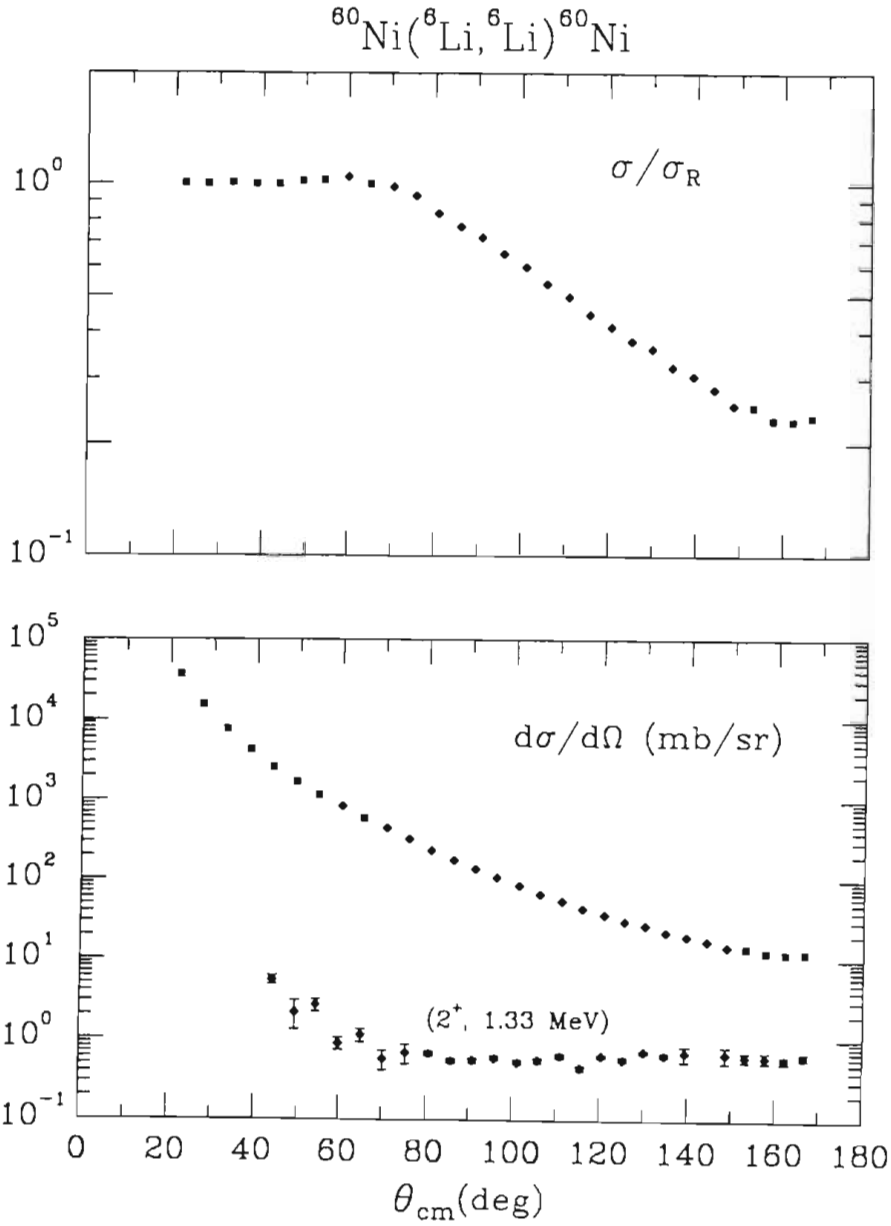

Figure 5.2.1 : Measured Cross-sections for ^{60}Ni(^{6}Li,^{6}Li) Scattering Forming the Ground and the $I^{\pi} = 2^{+}$, 1.33 MeV States of ^{60}Ni. Shown in the top part are measured ^{60}Ni(^{6}Li,^{6}Li) elastic scattering cross-sections divided by Rutherford cross-sections. Absolute cross-sections for the elastic and inelastic scattering are plotted in the lower part. Squares indicate data acquired using symmetrically placed detectors.

calibration. The average deviation of these measured energies from the kinematically predicted energies for ^{60}Ni(^{6}Li,^{6}Li') scattering forming the $I^{\pi} = 2^{+}$, 1.33 MeV state of ^{60}Ni was less than 1%, indicating that the second-highest-energy peak is definitely associated with the ^{60}Ni first excited state and that the highest-energy peak is at least partly associated with the ^{60}Ni ground state. Because of the width of the highest-energy peak, any contamination by ^{6}Li elastic scattering off other nuclei near mass 60 cannot be ruled out. However, no evidence for such a contamination was seen.

Spectra from the right-hand side, single detectors included some background below the two ^{60}Ni(^{6}Li,^{6}Li) peaks; otherwise, both the telescope and single-detector spectra were very clean. No other peaks were seen, except for very small ^{12}C and ^{16}O peaks at forward angles.

Chapter 6

A Simple Model for $\Delta l = 2$ α Transfers in the ^{64}Zn(d,^{6}Li) Reaction

Transfers forming ^{6}Li states with two units of orbital angular momentum between d and α are an important consideration when analyzing the ^{64}Zn($\vec{d}$,^{6}Li) data. The analysis of Chapter 8 suggests that formation of the $I^{\pi} = 3^{+}$, $l = 2$ resonance at $E_x = 2.185$ MeV may influence the ^{64}Zn(d,^{6}Li) reaction very strongly. Transfers forming the two other low-lying, $l = 2$, d-α resonances may also contribute significantly. Furthermore, the ^{64}Zn(d,^{6}Li) data may eventually be utilized to study the ^{6}Li ground-state D-wave admixture.

The dotted curves of Figure 6.1 show DWBA calculations of $d\sigma/d\Omega$, A_y, A_{yy}, A_{xx}, A_{zz}, and A_{xz} for α transfers forming the $l = 0$, $I^{\pi} = 1^{+}$, ^{6}Li ground state. The solid, dash-dot, and dashed curves are the results of DWBA calculations for α transfers forming *artificial*, pure $l = 2$, $I^{\pi} = 3^{+}$, 2^{+}, and 1^{+} ^{6}Li ground states, respectively. The wave functions of all four states were generated assuming the interaction geometry of equation (1.2.3) and adjusting the depth of this interaction to reproduce the binding energy of the ^{6}Li ground state. These calculations employed the TUNL-B deuteron optical potentials and the global ^{6}Li optical potentials of [Coo82b]. For the $\Delta l = 0$ transfer, the analyzing powers are small and oscillate symmetrically about zero. In contrast, the analyzing powers for $\Delta l = 2$ transfers reveal strong preferences for particular spin orientations. These calculations included spin-orbit coupling in the d-^{64}Zn channel. Calculations performed

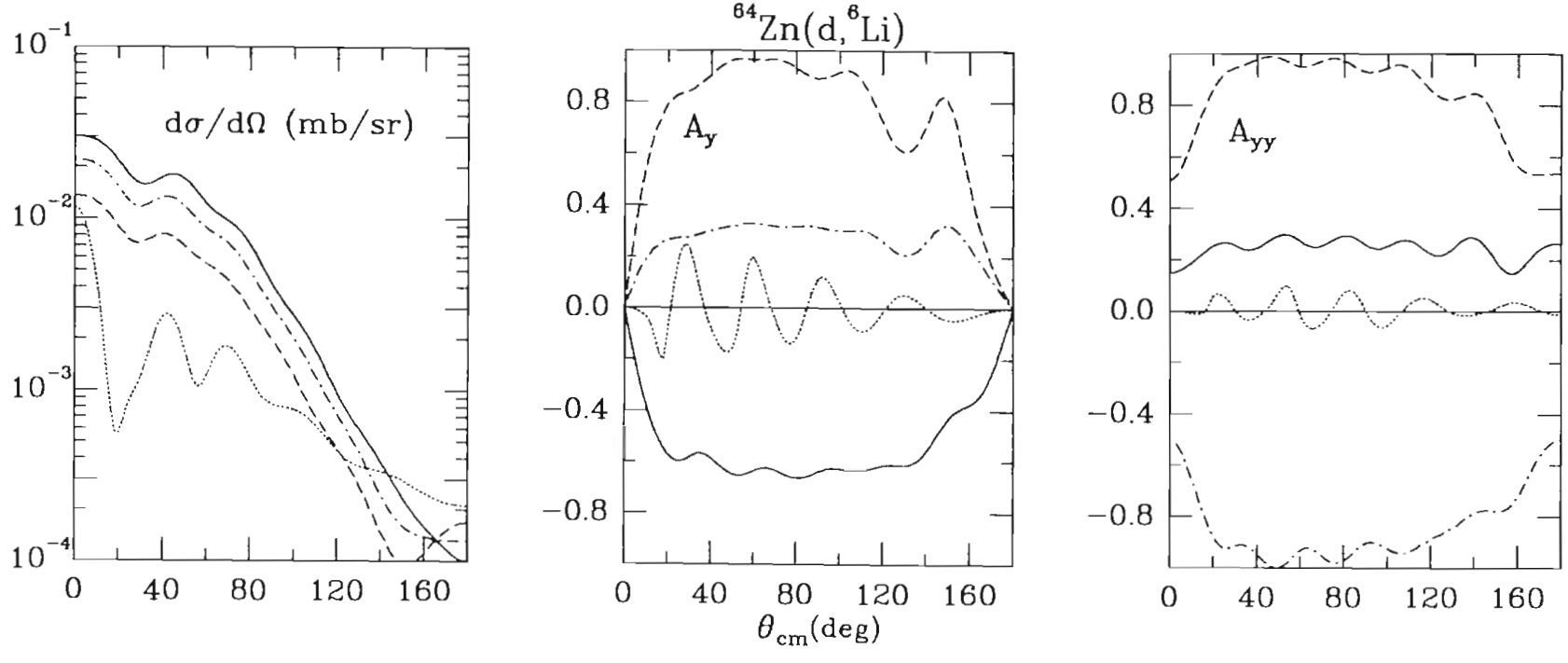

Figure 6.1 : Calculated Cross-sections and Analyzing Powers for One-Step α Transfers Forming *Artificial* ^{6}Li Ground States. The calculation corresponding to the dotted curve assumed a pure $l = 0$, $I^{\pi} = 1^{+}$ ^{6}Li ground state. The calculations associated with the solid, dash-dot, and dashed curves assumed artificial, pure $l = 2$, $I^{\pi} = 3^{+}$, 2^{+}, and 1^{+} ^{6}Li ground states, respectively.

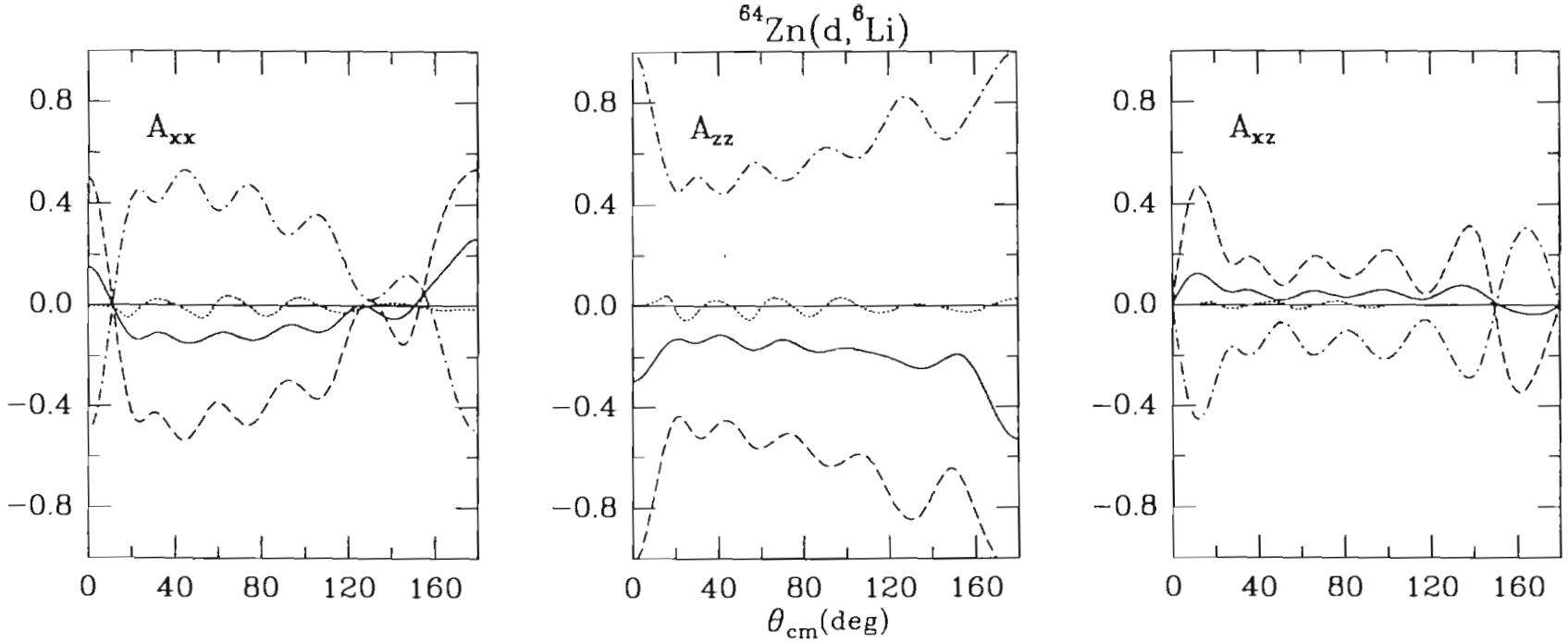

Figure 6.1 (Continued)

without spin-orbit coupling yielded zero for the $\Delta l = 0$ analyzing powers, whereas removing this coupling altered the $\Delta l = 2$ analyzing powers only slightly.

The above results for A_y, and to some extent those for the TAPs, can be understood in terms of a simple model. We discuss this model in the remainder of this chapter. For specificity, we focus on transfers forming $l = 2$, $I^\pi = 3^+$ states. Also for specificity, only ^{6}Li nuclei that strike detectors placed to the left of the beam are considered.

The trajectory of ^{6}Li should be roughly that of Coulomb scattering, because for the ^{64}Zn(d,^{6}Li) reaction at $E_{lab} = 16.4$ MeV, the center-of-mass energy of ^{6}Li is only slightly above the ^{6}Li-^{60}Ni Coulomb barrier energy. This expectation is confirmed by the ^{6}Li-^{60}Ni elastic scattering data [Chapter 5], which agrees with Coulomb cross-sections back to $\theta_{cm} \approx 65°$. It is interesting to calculate the semi-classical distance of closest approach assuming Coulomb scattering. The equation for this turning point is :

$$R_C = \frac{\eta + \sqrt{\eta^2 + L(L+1)}}{k_b} , \qquad (6.1)$$

where $\eta = \frac{\mu Z_1 Z_2}{k_b}$ is the Coulomb parameter, L is the orbital angular momentum between the projectile and the target, k_b is the wave number of the beam, Z_1 and Z_2 are projectile and target charges, and μ is the reduced mass of the system. Values of η and k_b for the ^{6}Li-^{60}Ni system are listed in Table 6.1. In Table 6.2, the turning points R_C are given as a function of M, where M is the projection of L. For reasons discussed below, values for d-^{64}Zn Coulomb scattering are also tabulated. In Table 6.2 and in the text below, the symbols L_{Li} (L_d) and M_{Li} (M_d) are used for specific references to the ^{6}Li-^{60}Ni (d-^{64}Zn) system.

Channel	E_{cm} (MeV)	η	k_b (fm^{-1})
d - ^{64}Zn	16.0	1.7	1.2
^{6}Li - ^{60}Ni	13.4	8.4	1.9

Table 6.1 : Values of η and k_b for ^{64}Zn(d,d) and ^{60}Ni(^{6}Li,^{6}Li) Elastic Scattering.

The values of R_C(Li) in Table 6.2 show that ^{6}Li is at least 9 fm from ^{60}Ni for all values of M_{Li}. Figure 8.1 indicates that, for $r_\alpha > 8$ fm, $|\varphi(Zn;r_\alpha)|^2$, the probability of finding an α particle a distance r_α from ^{60}Ni, is small and decreases rapidly with increasing r_α. Hence, the cross-section for forming ^{6}Li also decreases rapidly with increasing r_α. We thus expect the cross-section to be dominated by transfers at the distance of closest approach rather than farther out. The simple model assumes that all transfers occur at this distance.

Optical model calculations show that, at these energies, both d-^{64}Zn and ^{6}Li-^{60}Ni scattering are predominantly nearside. In the simple model, we assume that all d and ^{6}Li scattering occurs on the near side of ^{60}Ni, as drawn in Figure 6.2. The consequence of this premise is that (for scattering to a left detector) the projections of L_{Li} and L_d are down, into the paper of Figure 6.2. The negative signs for M_{Li} and M_d in Table 6.2 and Figure 6.2 indicate this projection.

The final assumption of the model is that the deuteron spin does not flip. Hence, deuterons incident with their spins up form ^{6}Li states in which the deuteron spin points up.

In an $l = 2$, $I^\pi = 3^+$ state of ^{6}Li, the two units of internal orbital angular momentum must be aligned with the deuteron spin to form the total spin of I = 3. The spin direction of the incident deuteron thus determines the sign of m, where m is the projection of l. It follows that, for a given M_{Li}, the deuteron spin direction determines the projection of total

M_d or M_{Li}	$R_C(d)$ (in fm)	$R_C(Li)$ (in fm)	$M_T = \lvert M_{Li} + m \rvert_{up}$	$M_T = \lvert M_{Li} + m \rvert_{dn}$
0	2.7	9.0	+2	-2
-1	3.1	9.0	+1	-3
-2	3.8	9.2	0	-4
-3	4.5	9.4	-1	-5
-4	5.3	9.6	-2	-6
-5	6.1	9.9	-3	-7
-6	6.8	**10.2**	-4	**-8**
-7	7.6	10.5	-5	-9
-8	**8.4**	10.9	-6	-10
-9	9.3	11.3	-7	-11
-10	10.1	**11.7**	**-8**	-12
-11	10.9	12.1	-9	-13
-12	11.7	12.5	-10	-14

Table 6.2 : Turning Points, R_C, of d-^{64}Zn and ^{6}Li-^{60}Ni Coulomb Scattering. The R_C were calculated using equation (6.1) and the values in Table 6.1. The projection of orbital angular momentum for ^{6}Li-^{60}Ni (d-^{64}Zn) scattering is denoted by M_{Li} (M_d). The projection of ^{6}Li internal orbital angular momentum is indicated by an m. The last two columns are explained in the text. Numbers in bold are specifically referred to in the text.

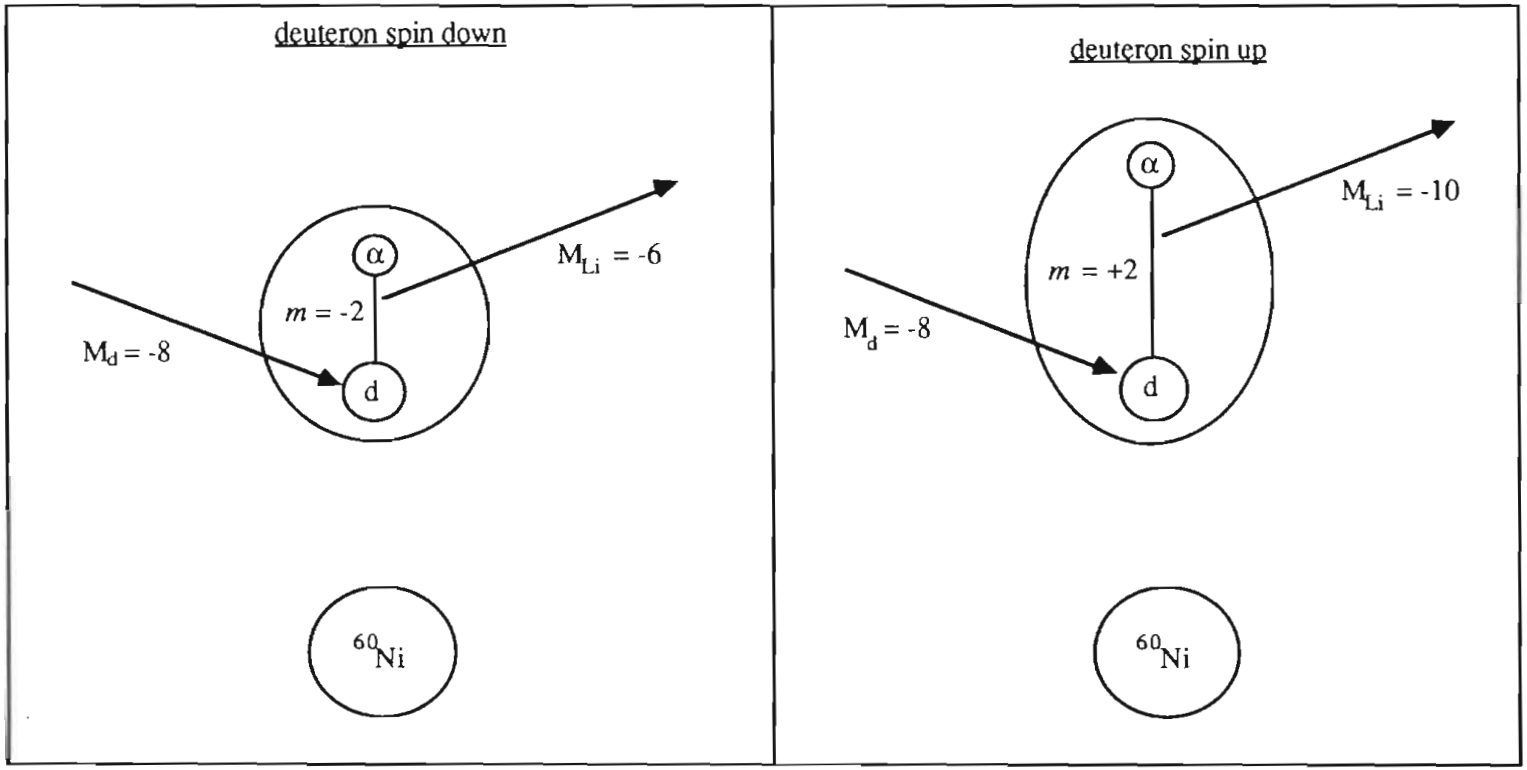

Figure 6.2 : A simple picture of α transfers forming *artificial* $l = 2$, $I^{\pi} = 3^{+}$, ^{6}Li ground states for the two opposite projections of incident deuteron spin. The projection of orbital angular momentum between d and ^{64}Zn (^{6}Li and ^{60}Ni) is given by M_d (M_{Li}). The plus and minus signs indicate projections directed into and out of the paper, respectively. The example of the text with $M_d = -8$ is illustrated but the qualitative picture is true for all M_d. The more negative values of M_{Li} for ^{6}Li nuclei formed from spin-up deuterons imply greater separations of the ^{6}Li and ^{60}Ni centers of mass, which in turn imply greater distances between ^{60}Ni and α and between d and α.

orbital angular momentum $M_T = (M_{Li} + m)$. The last two columns of Table 6.2 list M_T as a function of M_{Li} and the deuteron spin direction.

The major premises of the simple model are summarized below.

1) The transfer occurs with ^{6}Li at its Coulomb turning point.

2) ^{6}Li-^{60}Ni and d-^{64}Zn scattering are nearside.

3) The deuteron spin does not flip.

Two factors cause α transfers forming $I^\pi = 3^+$, $l = 2$ states of ^{6}Li to prefer spin-down deuterons.

First, since the projection of total angular momentum is conserved, the no-spinflip assumption implies that M_T, the projection of total *orbital* angular momentum, is also conserved. (Note also that since no internal orbital angular momentum is present in the d-^{64}Zn channel, $M_d = M_T$.) Consider the case of $M_T = -8$. Conservation of M_T requires that spin-down deuterons produce ^{6}Li nuclei with $M_{Li} = -6$ while spin-up deuterons produce ^{6}Li nuclei with $M_{Li} = -10$. According to Table 6.2, spin-down deuterons thus form ^{6}Li about 10.2 fm from ^{60}Ni whereas the transfer involving spin-up deuterons occurs at about 11.7 fm. Over this range, $|\varphi(Zn;r_\alpha)|^2$ decreases by a factor of about 60. Hence, the transfer strongly favors spin-down deuterons. In general, for a given L_T, spin-down deuterons are favored because they form ^{6}Li nuclei closer to ^{60}Ni than do spin-up deuterons.

Second, though Coulomb scattering does not accurately describe d-^{64}Zn scattering at $E_{lab} = 16.4$ MeV, the Coulomb turning points may be used to estimate an upper limit on the distance of closest approach. The attractive nuclear well should only reduce this distance. Table 6.2 indicates that, even assuming Coulomb scattering, d tends to be much closer to ^{60}Ni than is ^{6}Li. For example, with $M_T = -8$, the distances of closest approach are 8.4 fm, 10.2 fm, and 11.7 fm for deuterons, ^{6}Li nuclei formed from spin-down

deuterons, and ^{6}Li nuclei formed from spin-up deuterons, respectively. Hence, at the transfer, the centers of mass of d and ^{6}Li are well separated, which implies that the centers of mass of d and α are well separated. The cross-section for a transfer depends not only on $|\varphi(Zn;r_\alpha)|^2$, but also on the product $|\varphi(3^+,r)V_{d\alpha}(r)|^2$, where r is the separation of d and α and $\varphi(3^+,r)$ is the wave function of the ^{6}Li 3^+ state. This product falls off rapidly beyond the range of $V_{d\alpha}(r)$, which is about 4 fm, and thus strongly suppresses the cross-section. However, the ^{6}Li nuclei formed from spin-down deuterons are closer to ^{60}Ni and thus to d, so their formation is less suppressed by $|\varphi(3^+,r)V_{d\alpha}(r)|^2$.

For scattering to a left detector :

$$A_y \propto \frac{N_{up} - N_{dn}}{N_{up} + N_{dn}} , \qquad (6.2)$$

where N_{up} and N_{dn} are the number of ^{6}Li nuclei formed from spin-up and spin-down deuterons, respectively, and the proportionality constant is positive. The simple model thus predicts negative values of A_y.

More generally, the simple model implies that an α transfer forming any $l = 2$ state favors configurations in which l and L_{Li} are aligned. Spin-down deuterons are preferred for forming $I^\pi = 3^+$ states because they produce this alignment. In $I^\pi = 1^+$ states, l and the deuteron spin are anti-aligned, so α transfers forming these states favor spin-up deuterons and have positive VAPs. (Note the dashed A_y curve of Figure 6.1.)

The TAP A_{yy} may be defined as :

$$A_{yy} \propto \frac{N_{up} + N_{dn} - 2N_0}{N_{up} + N_{dn} + N_0} , \qquad (6.3)$$

where N_0 is the number of ^{6}Li nuclei formed from $\sigma^d = 0$ deuterons, that is, deuterons whose spins have no projection onto the spin symmetry axis. For formation of $I^\pi = 3^+$ (1^+) states, spin-down (spin-up) deuterons provide a stronger alignment of l and L_{Li} than

do $\sigma^d = 0$ deuterons. If this effect more than offsets the preference for $\sigma^d = 0$ deuterons over spin-up (spin-down) deuterons, A_{yy} should be positive, as it is for α transfers forming these two states.

The TAP are subject to the condition :

$$A_{xx} + A_{yy} + A_{zz} = 0. \tag{6.4}$$

In the region $20° \leq \theta_{cm} \leq 100°$, A_{xx} and A_{zz} are both of opposite sign to A_{yy} and have about half the magnitude of A_{yy}, suggesting that their values can be understood simply in terms of condition (6.4). At $\theta_{cm} = 0°$ and 180°, the X and Y axes are indistinguishable. The behavior of A_{xx} and A_{zz} near these angles is explicable in terms of (6.4) and the requirement :

$$A_{xx}(\theta_0) = A_{yy}(\theta_0), \ \theta_0 = 0°, 180° \tag{6.5}$$

Chapter 7

Coupled-Channels Treatment of the ^{6}Li-^{60}Ni Partition

Analysis of ^{60}Ni(^{6}Li,^{6}Li) Scattering

The low-lying states of the d-α system as well as wave functions associated with these states were described in Chapter 1. In this chapter, we couple those wave functions with functions specifying ^{6}Li-^{60}Ni scattering to form eigenstates of E_T, J^2, and M, where E_T is the total energy, J is the total angular momentum, and M is the projection of total angular momentum. Then, we approximate the ^{6}Li continuum as a small number of discrete states, thus allowing treatment of the d-α-^{60}Ni system within a coupled-channels (CC) framework. Diagonal and off-diagonal interactions among these states are generated from a folding model. Finally, this description of the ^{6}Li-^{60}Ni partition is tested against the ^{60}Ni(^{6}Li,^{6}Li) elastic scattering data described in Chapter 5.

Coupling of States

In general, the wave function of the d-α-^{60}Ni system in a state of total angular momentum J and projection M can be expanded in terms of a complete set of states of the d-α system. [Tos87]

$$\Psi_{JM}(\mathbf{r},\mathbf{R}) = [\, \chi^{J1}_{L0}(P_o,\mathbf{R}) \otimes \varphi^{1\sigma}(gs,\mathbf{r}) \,]_{JM} + \sum_{Il} \sum_{L} \int dk \, [\, \chi^{\Pi}_{Ll}(P_k,\mathbf{R}) \otimes \varphi^{I\sigma}_{l1}(k,\mathbf{r}) \,]_{JM}. \qquad (7.1)$$

The coordinate between d and α is $\mathbf{r}$ (Figure 7.1), and the wave functions $\varphi^{1\sigma}(gs,\mathbf{r})$ and $\varphi^{I\sigma}_{l1}(k,\mathbf{r})$ describe the d-α structure of ^{6}Li states. (Chapter 1) The

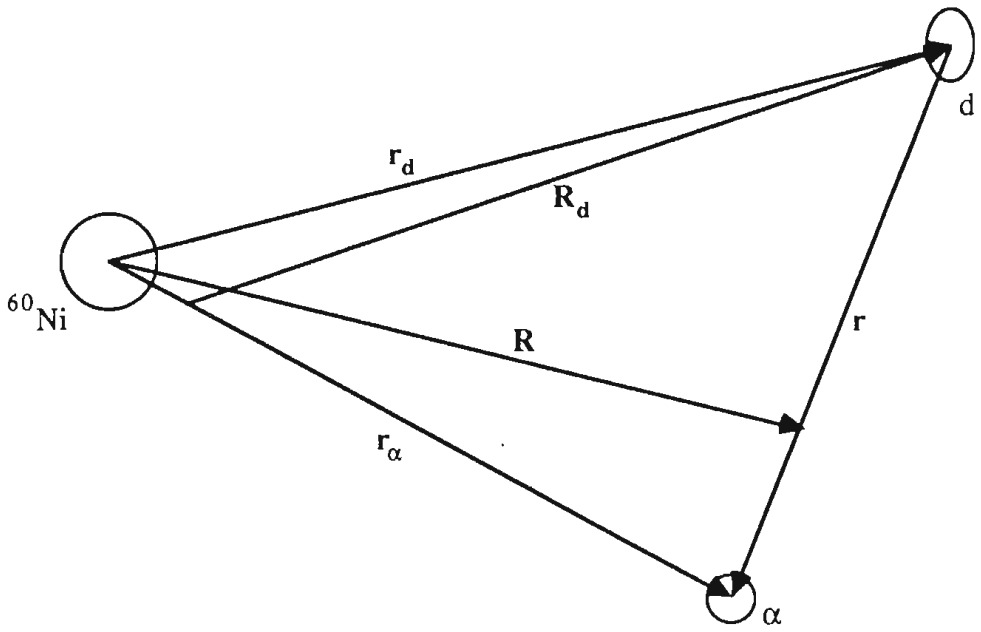

Figure 7.1 : Coordinates for the d-α-^{60}Ni System. The coordinates **R** and **r** are, of course, sufficient. At times, for clarity, $\mathbf{R_d}$, $\mathbf{r_d}$, and $\mathbf{r_\alpha}$ are utilized to indicate the specific dependence of a particular function.

coordinate between ^{60}Ni and the ^{6}Li center of mass is **R**. Scattering in this coordinate is specified by the $\chi^{JI}_{L0}(P_o,\mathbf{R})$ and $\chi^{JI}_{Lk}(P_k,\mathbf{R})$. The orbital angular momentum between ^{6}Li and ^{60}Ni is L; P_0 and P_k are asymptotic momenta. Energy conservation can thus be expressed as :

$$\frac{P_0^2}{2\mu_R} + \varepsilon_{gs} = \frac{P_k^2}{2\mu_R} + \varepsilon_k = E_T , \qquad (7.2)$$

where ε_{gs} = -1.47 MeV is the ground state binding energy, ε_k is defined by equation (1.2.8), and μ_R is the reduced mass of the ^{6}Li-^{60}Ni system.

The $\otimes$ and the $[\ ]_{JM}$ denote coupling of the internal wave function with total spin I and the scattering wave function with orbital angular momentum L to form the state of total angular momentum J and projection M.

Procedures for Binning the ^{6}Li *Continuum*

For ease of manipulation, equation (7.1) can now be written more schematically as :

$$\Psi_J(\mathbf{r},\mathbf{R}) = \chi^J(P_o,\mathbf{R})\,\varphi(gs,\mathbf{r}) + \sum_{\Omega}\int dk\ \chi^J_{\Omega}(P_k,\mathbf{R})\,\varphi_{\Omega}(k,\mathbf{r}) \qquad (7.3)$$

where Ω represents the quantum numbers I, *l*, and L.

Following the procedure of [Sak87], we replace the integral of (7.3) with a sum over a finite number of discrete states. The first step is to rewrite (7.3) as :

$$\Psi_J(\mathbf{r},\mathbf{R}) = \chi^J(P_o,\mathbf{R})\,\varphi(gs,\mathbf{r}) + \sum_{\Omega}\sum_{i}\int_{k_i^<}^{k_i^>} dk\ \chi^J_{\Omega}(P_k,\mathbf{R})\,\varphi_{\Omega}(k,\mathbf{r}) \qquad (7.4)$$

The integral over k has been broken up into a series of bins. The lower and upper bounds of bin i being denoted by $k_i^<$ and $k_i^>$. The energy dependence of the center-of-mass wave functions, $\chi^J_\Omega(P_k,\mathbf{R})$, can be accurately factored out. [Sak87]

$$\chi^J_\Omega(P_k,\mathbf{R}) \approx f_{il}(k)\, \chi^J_\Omega(P^i,\mathbf{R}), \tag{7.5}$$

where P^i is the ^{6}Li-^{60}Ni asymptotic momentum at the mean energy ε_i of the i^{th} bin. Over moderate energy intervals in non-resonant regions, the $\chi^J_\Omega(P_k,\mathbf{R})$ are essentially energy independent, implying :

$$f_{il}(k) = 1. \qquad \text{(non-resonant states)} \tag{7.6a}$$

In resonant regions, we use :

$$f_{il}(k) = \sin\delta(k), \qquad \text{(resonant states)} \tag{7.6b}$$

where $\delta(k)$ is the nuclear phase shift. The function $\sin\delta(k)$ takes on a characteristic resonant form. Other authors have used slightly different forms [Sak87], but results are insensitive to such details.

Using (7.5), (7.4) can be reduced to :

$$\Psi_J(\mathbf{r},\mathbf{R}) = \chi^J(P_o,\mathbf{R})\, \varphi(gs,\mathbf{r}) + \sum_\Omega \sum_i \chi^J_\Omega(P^i,\mathbf{R}) \int_{k_i^<}^{k_i^>} dk\, \varphi_\Omega(k,\mathbf{r})\, f_{il}(k) \tag{7.7}$$

Equation (7.7) can be cast into a form that is truly analogous to a sum over normalized, discrete states by substituting in the definitions :

$$X^J_\Omega(P^i,\mathbf{R}) \equiv \sqrt{N_{il}}\ \chi^J_\Omega(P^i,\mathbf{R}), \tag{7.8}$$

$$\Phi_{\Omega i}(\mathbf{r}) \equiv \frac{1}{\sqrt{N_{il}}} \int_{k_i^<}^{k_i^>} dk\, \varphi_{\Omega}(k,\mathbf{r})\, f_{il}(k), \text{ and} \tag{7.9}$$

$$N_{il} \equiv \int_{k_i^<}^{k_i^>} dk\, [f_{il}(k)]^2, \tag{7.10}$$

giving :

$$\Psi_J(\mathbf{r},\mathbf{R}) = \chi^J(P_o,\mathbf{R})\, \varphi(gs,\mathbf{r}) + \sum_{\Omega} \sum_{i} X^J_{\Omega}(P^i,\mathbf{R})\, \Phi_{\Omega i}(\mathbf{r}) \tag{7.11a}$$

$$\equiv \sum_{\beta} \chi^J_{\beta}(\mathbf{R})\, \varphi_{\beta}(\mathbf{r}). \tag{7.11b}$$

The notation of (7.11b) will be convenient for manipulations below. One point concerning the analogy between discrete states and the $\Phi_{\Omega i}(\mathbf{r})$ of equations (7.9) and (7.11) is that the $\Phi_{\Omega i}(\mathbf{r})$ form a square-integrable set of states. That is :

$$\left(\Phi_{\Omega i}(\mathbf{r}) | \Phi_{\Omega' i'}(\mathbf{r}) \right)_{\mathbf{r}} = \delta_{ii'}\, \delta_{\Omega\Omega'}, \tag{7.12}$$

where $(\,)_{\mathbf{r}}$ denotes integration over all $\mathbf{r}$.

Truncation of the ^{6}Li Continuum

Following the work of Sakuragi *et al.* [Sak87], we include in the calculations only the l = 0, 1, and 2 states of the ^{6}Li continuum. For each of the l = 0 and 1 states, a bin was placed over the interval 0.05 fm^{-1} ≤ k ≤ 0.55 fm^{-1}, which corresponds to the energy interval 0.039 MeV ≤ ε_k ≤ 4.722 MeV. These states were located at ε_i = 2.381 MeV, that is, 3.854 MeV above the ^{6}Li ground state. For the l = 2 states, bin widths of 0.028, 2.0, and 3.0 MeV were utilized for the $I^{\pi} = 3^+$, 2^+, and 1^+ states, respectively, as these widths correspond crudely to the widths of these states. These states were placed at 2.185, 4.36, and 5.3 MeV above the ground state, as specified in Table 1.2.2. Hence, the calculations included the spin orbit splitting of these states. The locations and widths of these bins are

illustrated schematically in Figure 7.2. In equations (7.1) through (7.11), the sums over l are therefore restricted to $0 \leq l \leq 2$; the lower and upper limits of the integrals in these equations correspond to the lower and upper limits of the bins.

Calculation of the ^{6}Li Continuum-Bin Wave Functions

The $\Phi_{\Omega i}(\mathbf{r})$ were generated numerically within FRESCO according to prescription (7.9) and over the range 0 fm $\leq r \leq$ 45 fm. For each bin, Table 7.1 indicates the value of $(\Phi_{\Omega i}(\mathbf{r})|\Phi_{\Omega i}(\mathbf{r}))_r$ as approximated by an integration restricted to this same radial range. All values are near 1.0, as required by condition (7.12). Each $\Phi_{\Omega i}(\mathbf{r})$ was renormalized to satisfy this condition exactly.

l	0	1			2		
$I\pi$	1+	2-	1-	0-	3+	2+	1+
integral	0.98	0.97	0.97	0.93	0.83	0.96	0.96

Table 7.1 : Initial Normalizations of the ^{6}Li Continuum-Bin Wave Functions. The numbers shown are $(\Phi_{\Omega i}(\mathbf{r})|\Phi_{\Omega i}(\mathbf{r}))_r$ as approximated by an integration over the range 0 fm $\leq r \leq$ 45 fm.

The $\Phi_{\Omega i}(\mathbf{r})$ corresponding to each of the seven bin states are shown in Figure 7.3.

Coupled-Channels Equations and Folding Model Interactions

The Schrodinger equation describing the ^{6}Li-^{60}Ni system is :

$$(E_T - T_R(\mathbf{R}) - U^{eff}(\mathbf{R},\mathbf{r}) - H_{Li}(\mathbf{r})) \sum_{\beta'} \varphi_{\beta'}(\mathbf{r}) \chi^J_{\beta'}(\mathbf{R}) = 0. \qquad (7.13)$$

The notation (7.11b) has now been adopted, so that both the ground and continuum bin wave functions are designated by $\varphi_\beta(\mathbf{r})$. $T_R(\mathbf{R})$ is the kinetic energy operator associated

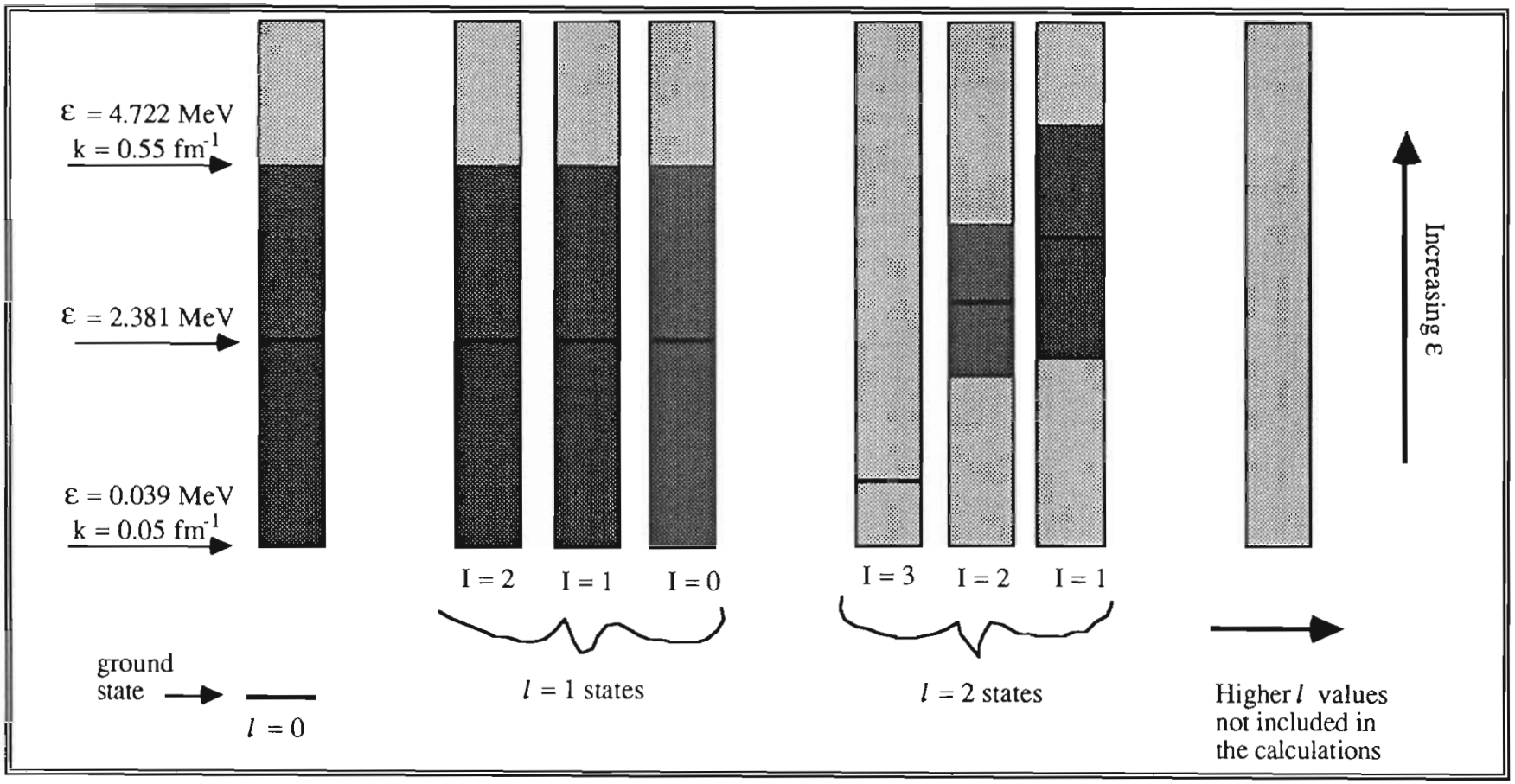

Figure 7.2 : Placement of Bins over the ^{6}Li Continuum. The $l = 2$, $I^{\pi} = 3^{+}$, 2^{+}, and 1^{+} bins were centered at $\varepsilon_{res} = 0.711$, 2.89, and 3.8 MeV, respectively, as indicated in table 1.2.2.

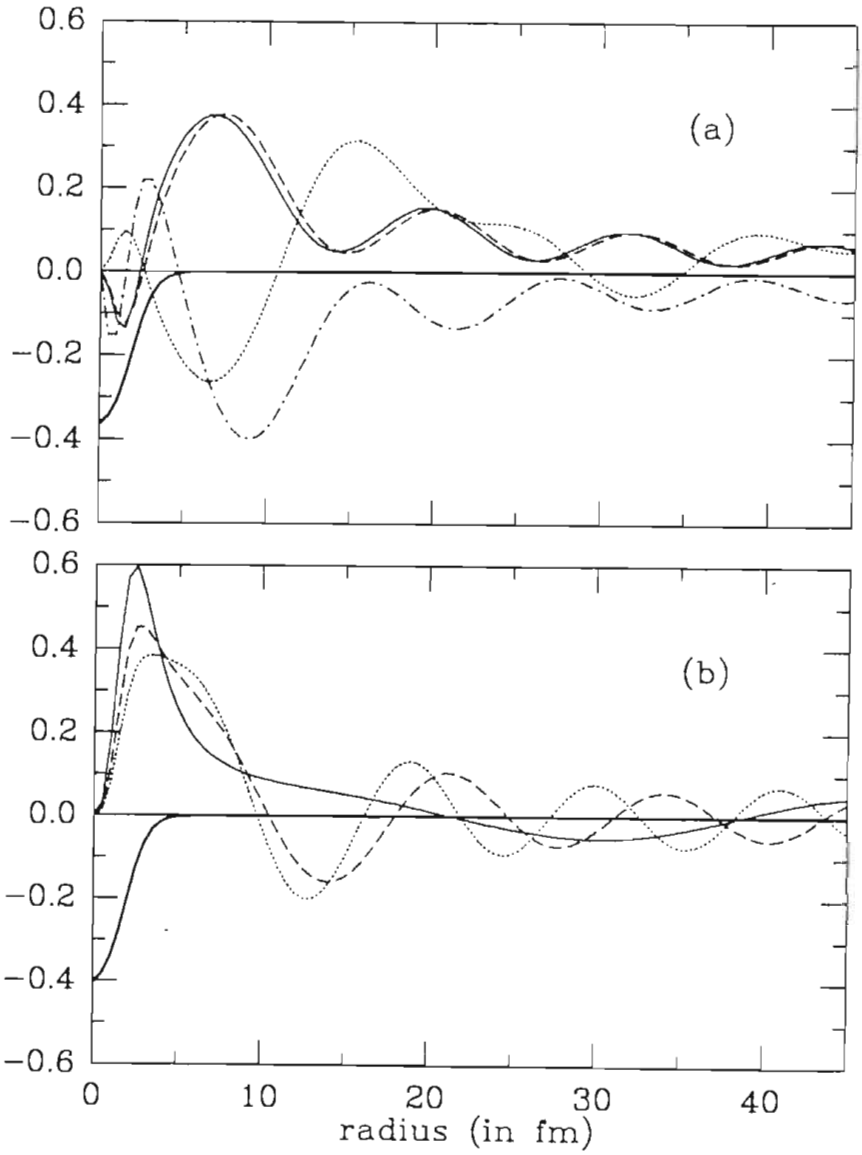

Figure 7.3 : Wave Functions for the ^{6}Li Continuum Bins. The dash-dot curve of part (a) represents the wave function r•φ(r) associated with the $l = 0$ bin. The solid, dashed, and dotted curves of part (a) are for the $l = 1$, $I^\pi = 2^-$, 1^-, and 0^- bins, respectively. Those of part (b) are for the $l = 2$, $I^\pi = 3^+$, 2^+, and 1^+ bins. The dark solid curves of parts (a) and (b) indicate the Woods-Saxon potentials in which wave functions associated with the 2^- and 3^+ bins were calculated, respectively.

with $\mathbf{R}$, and $U^{eff}(\mathbf{R},\mathbf{r})$ is the interaction between ^{6}Li and ^{60}Ni. $H_{Li}(\mathbf{r})$ is the internal Hamiltonian of ^{6}Li. Note that :

$$H_{Li}(\mathbf{r})\ \varphi_\beta(\mathbf{r}) = \varepsilon_\beta\ \varphi_\beta(\mathbf{r}) \tag{7.14}$$

Multiplying (7.13) on the left by $\varphi_\beta(\mathbf{r})$, integrating over the internal coordinate, $\mathbf{r}$, and using expressions (7.12) and (7.14) gives the CC equation for $\chi^J_\beta(\mathbf{R})$.

$$\left(E_\beta - T_R(\mathbf{R}) - U_{\beta\beta}(\mathbf{R}) \right) \chi^J_\beta(\mathbf{R}) = \sum_{\beta' \neq \beta} U_{\beta\beta'}(\mathbf{R})\ \chi^J_{\beta'}(\mathbf{R}) \tag{7.15}$$

where :

$$E_\beta = E_T - \varepsilon_\beta, \tag{7.16}$$

and :

$$U_{\beta\beta'}(\mathbf{R}) = \left(\varphi_\beta(\mathbf{r}) \mid U^{eff}(\mathbf{R},\mathbf{r}) \mid \varphi_{\beta'}(\mathbf{r}) \right)_{\mathbf{r}} \tag{7.17}$$

Equation (7.17) is a cluster folding model (CFM) prescription for obtaining the $U_{\beta\beta'}(\mathbf{R})$. These interactions are not always obtained according to (7.17). For example, in single-channel calculations, (7.15) reduces to :

$$\left(E_0 - T_R(\mathbf{R}) - U_{00}(\mathbf{R}) \right) \chi^J_0(\mathbf{R}) = 0, \tag{7.18}$$

and a phenomenological optical model potential, adjusted to reproduce elastic scattering observables, may be used for $U_{00}(\mathbf{R})$. For several reasons, we obtained the $U_{\beta\beta'}(\mathbf{R})$ from the CFM.

1) In (7.17), the $\varphi_\beta(\mathbf{r})$ are wave functions of the d-α system, and, as discussed below, $U^{eff}(\mathbf{R},\mathbf{r})$ is based on phenomenological d-^{60}Ni and α-^{60}Ni interactions. Thus, obtaining the $U_{\beta\beta'}(\mathbf{R})$ from (7.17) is highly consistent with the three-body, d-α-^{60}Ni model space employed in this

analysis. The amount of physics extracted from an analysis depends on how decisively a particular model is either confirmed or discredited. Use of the CFM provides for a stringent test of the d-α-^{60}Ni model space.

2) The off-diagonal potentials $U_{\beta\beta'}(\mathbf{R})$ must be obtained by some method. The other obvious choice would be a collective model, which is undesirable for two reasons. First, in a collective model, the relevant degrees of freedom are those describing the bulk shape of a nucleus. Such a model is inconsistent with the d-α degrees of freedom employed in the remainder of this analysis. Secondly, collective model CC analyses of ^{7}Li elastic scattering, which has many properties in common with ^{6}Li elastic scattering, have not been particularly successful. [Ohn84]

3) Coupled-channels treatments that obtain $U_{\beta\beta'}(\mathbf{R})$ from folding models based on the d-α cluster structure of ^{6}Li have successfully described cross-sections [Sak87], VAP [Nis84,Ohn84], and TAP [Nis83] for ^{6}Li elastic scattering.

Appropriate Effective Interactions

The effective interaction of equations (7.13) and (7.17) was obtained from phenomenological d-^{60}Ni and α-^{60}Ni optical model potentials. Specifically :

$$U^{eff} = N_R (V_{d\text{-}Ni} + V_{\alpha\text{-}Ni}) + N_I (W_{d\text{-}Ni} + W_{\alpha\text{-}Ni}), \qquad (7.19)$$

where $V_{d\text{-}Ni}$ ($V_{\alpha\text{-}Ni}$) and $W_{d\text{-}Ni}$ ($W_{\alpha\text{-}Ni}$) are the real and imaginary components of the d-^{60}Ni (α-^{60}Ni) optical model interactions. Appropriate values of the scale factors N_R and N_I are discussed below.

The ^{6}Li ejectiles scattered off ^{60}Ni at E_{lab} = 14.8 MeV; the deuterons within ^{6}Li therefore scattered at E_{lab} = 14.8/3 MeV = 4.9 MeV. The $V_{d\text{-}Ni}$ and $W_{d\text{-}Ni}$ were calculated utilizing the set L global parameterization of Daehnick *et al.*, even though these parameters were generated using (d,d) elastic scattering data taken at significantly higher energies, specifically 11.8 MeV $\leq E_{lab} \leq$ 90.0 MeV. [Dae80]

Discrete ambiguities in α particle optical model parameters have been resolved and continuous ambiguities have been curtailed by analyses of high energy (E_{lab} > 100 MeV), back angle (α,α) data in which nuclear rainbow scattering occurs. For the α-^{58}Ni interaction, these analyses determined that, at E_{lab} = 139 MeV, the real volume integral per nucleon is :

$$\frac{J_V}{4A} \approx 300 \text{ MeV}\cdot\text{fm}^3. \qquad (7.20)$$

[Sat83, Gol74] Furthermore, microscopic calculations and phenomenological analyses have revealed that the real potential is well approximated by an energy independent, Woods-Saxon-squared shape. [Sat83, Bud78] Budzanowski *et al.* have developed a global parameterization describing ^{58,60}Ni(α,α) scattering at incident energies ranging from 26.5 to 139 MeV. They assumed potentials of the form :

$$U(r) = V_C(r) - Vf^2(r,r_0,a_0)$$
$$- i\,[\, W_S\, f^2(r,r_{WS},a_{WS}) - 4\, a_{WD}\, W_D \frac{d}{dr} f^2(r,r_{WD},a_{WD})], \qquad (7.21)$$

where $f(r,r_X,a_X)$ is the familiar Woods-Saxon form factor of equation (5.1.4) and $V_C(r)$ is the Coulomb interaction due to a uniformly charged sphere of radius $1.34\cdot A^{1/3}$. Discrete ambiguities were avoided by requiring $\frac{J_V}{4A} \approx 300$ MeV•fm^3 at E_{lab} = 139 MeV as well as a reasonable energy dependence for the depth of the real potential. The fitting procedure

produced potentials with real volume integrals very near 300 MeV•fm^3 for all incident energies. [Bud78]

The α particles within ^{6}Li scattered at E_{lab} = 2•14.8/3 = 9.9 MeV. Parameters appropriate for ^{60}Ni(α,α) at E_{lab} = 9.9 MeV were calculated according to the prescription of [Bud78] and are given in Table 7.2. Only the real volume and surface imaginary parameters are shown, as the predicted volume imaginary interaction W_S is negligible at such low energies.

V(MeV)	r_0(fm)	a_0(fm)	W_D(MeV)	r_{WD}	a_{WD}
154.9	1.42	1.19	28.6	1.33	0.407

Table 7.2 : Potentials describing ^{60}Ni(α,α) scattering at E_{lab} = 9.9 MeV as calculated using the global parameterization of Budzanowski *et al.* The parameters refer to equation (7.21).

One might expect that full CC calculations employing CFM interactions would reproduce both (^{6}Li,^{6}Li) and (d,^{6}Li) data with $N_R = N_I = 1.0$, assuming that the bins utilized in these calculations adequately account for all important states of the ^{6}Li continuum.

Certainly, full CC calculations utilizing double-folding models have provided excellent reproductions of cross-sections for ^{6}Li elastic scattering. Sakuragi *et al.* [Sak87] analyzed cross-section data for ^{6}Li elastic scattering at incident energies between 40 and 170 MeV on targets ranging in mass from A = 12 to 208 with CC calculations which included the l = 0, 1, and 2 states of the ^{6}Li continuum. The real component of the ^{6}Li-target interaction was obtained by folding a realistic, effective nucleon-nucleon interaction over projectile and target wave functions. The imaginary potential was assumed to be a simple scaling of the folded real interaction with the scaling factor adjusted to best

reproduce the data. Their CC calculations generated excellent fits to the data without any renormalization applied to the folded, real potential.

Use of the CFM in CC analyses of (^{6}Li,^{6}Li) cross-section data has been less extensive, and the validity of this approach is less definitive. Thompson and Nagarajan [Tho81] utilized the adiabatic approximation of Amakawa *et al.* [Ama79] to study ^{6}Li elastic scattering on ^{12}C, ^{40}Ca, and ^{208}Pb at E_{lab} = 156 MeV. As here, they folded in the real and imaginary components of d-target and α-target interactions and included in their calculations the ^{6}Li ground state and the l = 0, 1, and 2 continuum states. These CC calculations reproduced all three sets of cross-section data fairly well, without any renormalization of either the real or imaginary interactions. In contrast, a CC analysis of ^{58}Ni(^{6}Li,^{6}Li) scattering at E_{lab} = 20.0 MeV by Ohnishi *et al.* [Ohn84] underestimated the back-angle cross-sections, suggesting that the folding model potentials were too deep. As with the calculations performed for the present work, these calculations included the ^{6}Li ground state and one level for each of the seven spin and parity values of the l = 0, 1, and 2 continuum states. In a similar procedure, Nishioka *et al.* [Nis84] included the ground and the three l = 2 resonant states in CC calculations of ^{58}Ni(^{6}Li,^{6}Li) scattering at E_{lab} = 14.0, 20.0, and 22.8 MeV. For these calculations, a renormalization of 0.5 applied to both the real and imaginary interactions was necessary. As discussed below, our CC calculations underestimate the back angle cross-sections for ^{60}Ni(^{6}Li,^{6}Li) scattering at E_{lab} = 14.8 MeV.

For calculations that include the ground state only, the interaction U^{eff} of equation (7.17) must be modified to compensate for the ^{6}Li states excluded from the calculation. [Gle83] Double folding model and CFM studies of ^{6}Li elastic scattering have provided insight into the type of modifications needed.

Satchler and Love [Sat78] employed double-folding model interactions in a single-channel analysis of ^{6}Li elastic scattering on ^{28}Si, ^{40,44,48}Ca, ^{58}Ni, ^{90}Zr, ^{124}Sn and ^{208}Pb at various energies between 28 and 135 MeV. The imaginary interactions took the form of either three-parameter Woods-Saxon potentials or simple scalings of the folded real potentials and were adjusted to best reproduce the data. Good fits to the data could not be obtained without sharply reducing the depth of the folded real interaction. Averaged over all targets and beam energies, a renormalization of 0.58 ± 0.04 was determined.

Cook *et al.* [Coo82] studied ^{40}Ca(^{6}Li,^{6}Li) elastic scattering at E_{lab} = 26, 28, 30, and 34 MeV. They obtained the real ^{6}Li-^{40}Ca interaction from double folding an effective NN interaction and from a single folding of d-^{40}Ca and α-^{40}Ca potentials. Woods-Saxon interactions were employed for the imaginary potentials. The data could not be fit without renormalizations of 0.64 for the double-folding interaction and 0.61 for the single-folding potential.

Finally, in the aforementioned analysis by Sakuragi *et al.*, single-channel calculations were performed, and, again, a renormalization of about 0.6 was required to reproduce the data. Also, the same imaginary potentials were found to be optimal for both single-channel and full CC calculations.

These results imply that, in a single-channel representation of (^{6}Li,^{6}Li) scattering, the excluded states of ^{6}Li induce a strongly repulsive, real potential but do not alter the imaginary potential.

Analysis of ^{60}Ni(^{6}Li,^{6}Li) Scattering

The dotted, dashed, dash-dot, and solid curves of Figure 7.4 are the results of ^{60}Ni(^{6}Li,^{6}Li) calculations utilizing CFM interactions and including, respectively, the ^{6}Li ground state, the ground and 3^{+} states, the ground, 3^{+}, 2^{+}, and 1^{+}(l=2) states, and all eight

l = 0, 1 , and 2 states of Figure 7.2. The parameters N_R and N_I were set to 1.0. Couplings to the excited states improved the fit considerably. However, even the 8-state CC calculations underestimated the back-angle cross-sections.

For several reasons, a determination of the values of N_R and N_I needed to reproduce ^{60}Ni(^{6}Li,^{6}Li) cross-section data with both single-channel and full (8-state) CC calculations is useful. In full CC calculations, departures of N_R and N_I from 1.0 measure the failure of the CFM. Also, the values N_R and N_I obtained here can be compared with those obtained in the folding model analyses discussed above. Finally, we wish to consider ^{64}Zn(d,^{6}Li) calculations using values of N_R and N_I that accurately describe ^{60}Ni(^{6}Li,^{6}Li) elastic scattering at E_{lab} = 14.8 MeV.

Shown in Figure 7.5 are the results of single-channel calculations employing N_R = 0.6, 0.4, and 0.3, respectively. The solid, dashed, and dotted curves are associated with N_I = 1.0, 0.7, and 0.4. Values of $\chi 2$ per point, as defined by equation (5.1.5), for these and several other calculations are given in Table 7.3. The $\chi 2$ values imply that :

$$(N_R, N_I) = (0.30, 0.70), \text{ or} \qquad \text{(single-channel)} \qquad (7.22a)$$

$$(N_R, N_I) = (0.25, 0.75) \qquad (7.22b)$$

provide the best single-channel, effective interaction attainable from the CFM. Figure 7.5 supports this conclusion. Cross-sections calculated under the assumption that N_R = 0.6 fall off too quickly as a function of angle. The same is true of calculations using N_R = 0.4, though the effect is much less pronounced. Use of (N_R, N_I) = (0.30, 0.70) generates a fairly good fit to the data.

Figure 7.6 shows the results of full, eight-state CC calculations with N_R = 0.9, 0.7, and 0.5, respectively. Again, the solid, dashed, and dotted curves correspond to N_I = 1.0, 0.7, and 0.4. Values of $\chi 2$ per point are listed in Table 7.4. The curves of Figure

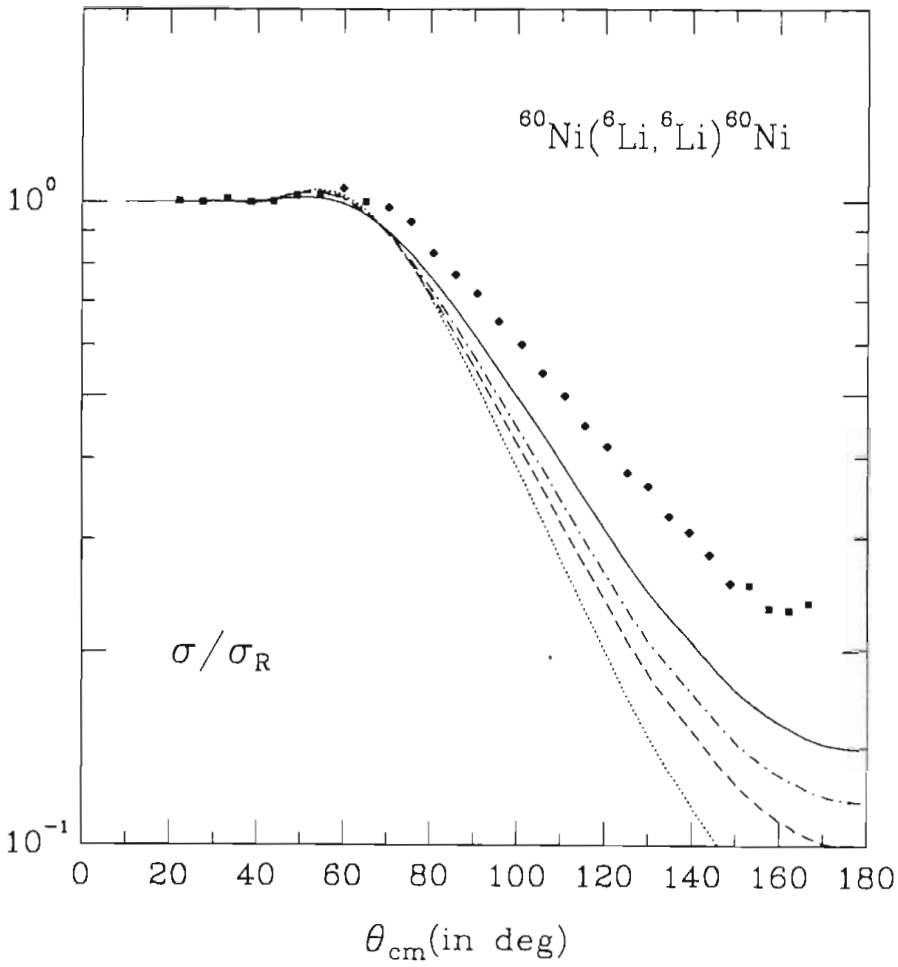

Figure 7.4 : The Effect of Channel Coupling on Predicted Cross-sections for ^{60}Ni(^{6}Li,^{6}Li) Elastic Scattering at E_{lab} = 14.8 MeV. The dotted, dashed, dash-dot, and solid curves correspond to calculations including the ^{6}Li ground state only, the ground and 3^+ states, the ground, 3^+, 2^+, and 1^+(l=2) states, and all eight states of Figure 7.2, respectively. For all four calculations, $N_R = N_I = 1$. Squares indicate data acquired using symmetrically placed detectors. (See Chapter 5.)

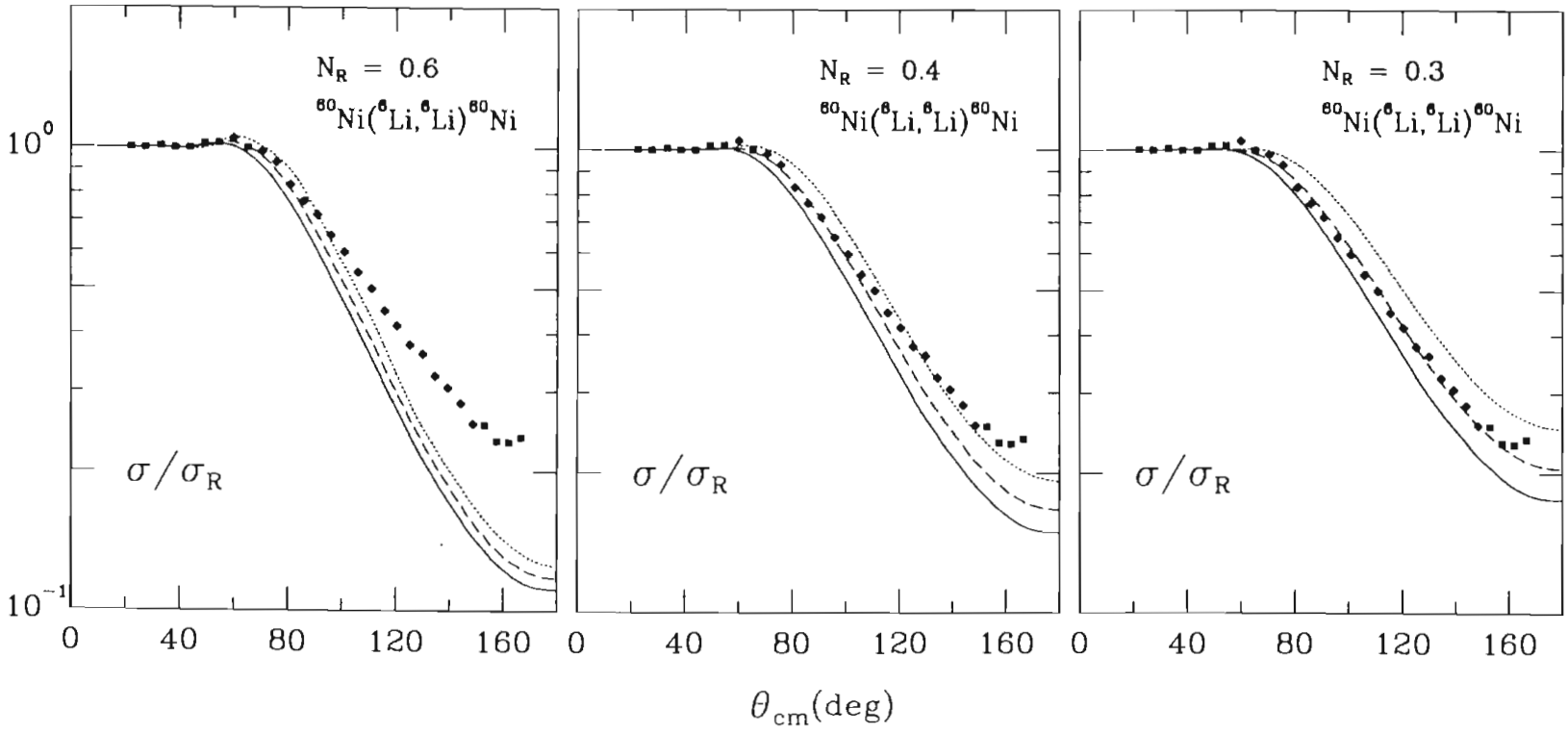

Figure 7.5 : Cross-sections for ^{60}Ni(^{6}Li,^{6}Li) Elastic Scattering as Predicted by Single-Channel Calculations using Cluster Folding Model Interactions. Parts (a), (b), and (c) assume N_R = 0.6, 0.4, and 0.3, respectively. The solid, dashed, and dotted curves correspond to N_I = 1.0, 0.7, and 0.4.

$N_I \backslash N_R$	0.80	0.60	0.40	0.30	0.25
1.00	1513	879	338	150	---
0.75	---	---	---	---	**29**
0.70	1129	503	77	**26**	60
0.40	822	291	211	541	---

Table 7.3 : Values of χ^2 per Point for Single-Channel Calculations of $^{60}Ni(^6Li,^6Li)$ Cross-sections. Equation (5.1.5) defines χ^2.

$N_I \backslash N_R$	0.90	0.70	0.50
1.00	447	224	**32**
0.70	279	90	**27**
0.40	148	**20**	112

Table 7.4 : Values of χ^2 per Point for Full, Coupled-Channels Calculations of $^{60}Ni(^6Li,^6Li)$ Cross-sections. Equation (5.1.5) defines χ^2.

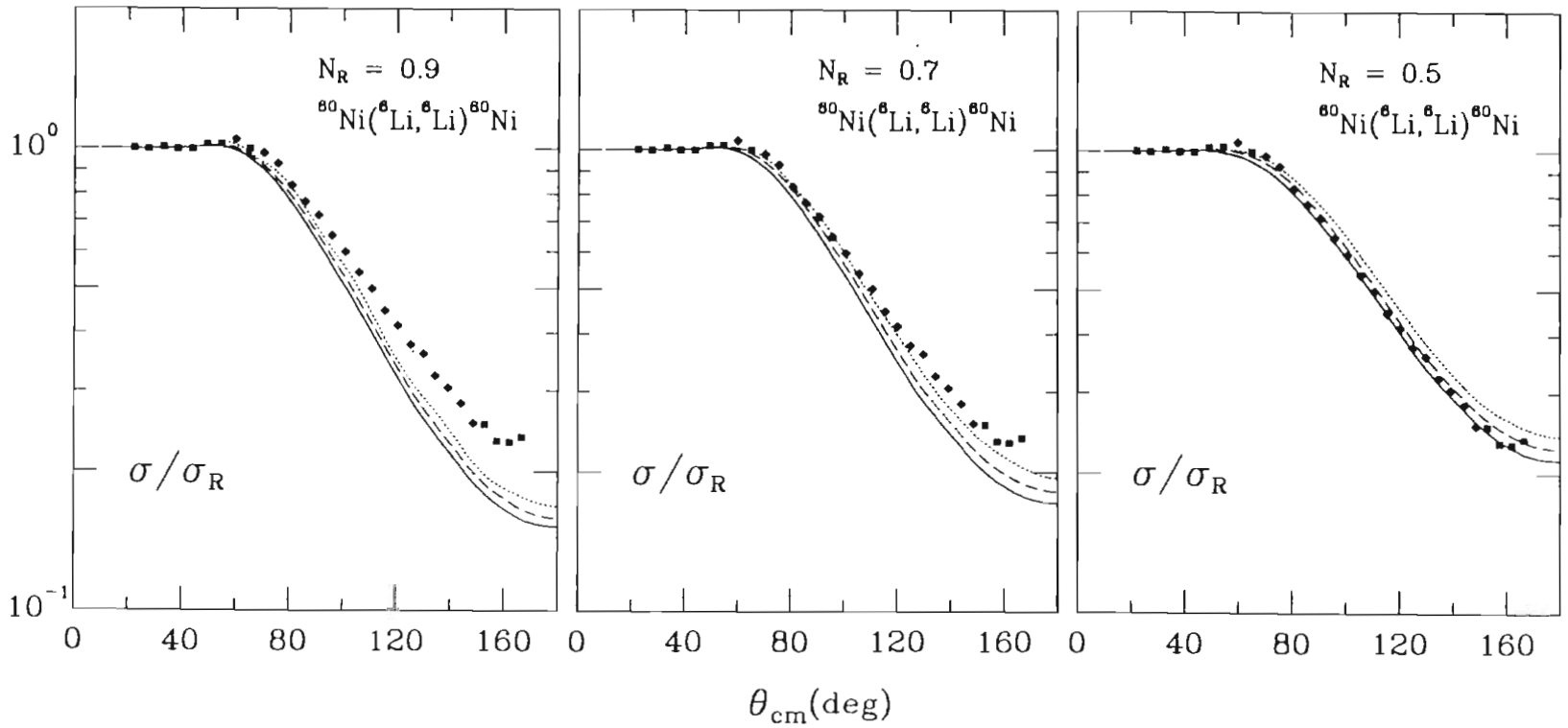

Figure 7.6 : Cross-sections for ^{60}Ni(^{6}Li,^{6}Li) Elastic Scattering as Predicted by Full Coupled-Channels Calculations using Cluster Folding Model Interactions. Each calculation includes all eight states of Figure 7.2. Parts (a), (b), and (c) assume N_R = 0.9, 0.7, and 0.5, respectively. The solid, dashed, and dotted curves correspond to N_I = 1.0, 0.7, and 0.4.

7.6 indicate that $N_R = 0.9$ underestimates the back-angle cross-section and suggest that the optimal value of N_R lies in the range :

$$0.5 \leq N_R \leq 0.7 \qquad \text{(full CC)} \qquad (7.23)$$

As with the single-channel calculations, the optimal value of N_I increased as that of N_R decreased. Of the values examined, the data were best reproduced by :

$$(N_R, N_I) = (0.7, 0.4) \qquad \text{(full CC)} \qquad (7.24)$$

The most significant result from the preceding analysis is that the full CC calculations utilizing CFM interactions reproduced the data only after a substantial renormalization of these interactions. Also, the optimal single-channel renormalization $N_R = 0.30 - 0.25$ is considerably lower than the value $N_R = 0.6$ obtained in many of the folding model analyses reviewed above. These results are consistent with the previously reported failure of calculations utilizing CFM interactions to reproduce ^{58}Ni(^{6}Li,^{6}Li) elastic scattering at Elab $\leq$ 22.8 MeV.

Possible explanations of this effect should be explored. First, it would be interesting to establish whether full CC calculations using CFM interactions (and $N_R = N_I = 1$) can reproduce ^{6}Li elastic scattering data. Second, if some deficiency in the calculations underlies these results, that deficiency may adversely affect the CCBA analysis of the (d,^{6}Li) reaction. The optical model parameters employed as folding model inputs are somewhat suspect. As discussed above, $U_{d\text{-}Ni}$ and $U_{\alpha\text{-}Ni}$ were calculated from global prescriptions developed using data acquired at significantly higher energies. It is interesting to note that cross-sections generated by single-channel calculations using the global, phenomenological optical potentials of [Coo82b] are nearly identical to the cross-sections yielded by a full CC calculation using CFM interactions and assuming $N_R = N_I = 1$. (The solid curve of Figure 7.4.) The energy dependences of the [Coo82b] ^{6}Li-^{60}Ni

potentials and the d-^{60}Ni and α-^{60}Ni potentials employed by the folding model were obtained by analyzing higher energy elastic scattering data. The nearly identical failure of the phenomenological and CFM approaches suggests that the ^{60}Ni(^{6}Li,^{6}Li) data is not reproduced because these energy dependences are not valid at the near Coulomb barrier energies considered here. Measurements of ^{60}Ni(d,d) cross-sections at E_{lab} = 4.9 MeV and ^{60}Ni(α,α) cross-sections at E_{lab} = 9.9 MeV would help to resolve this uncertainty. A second possibility is that more continuum bins are needed for each value of I and *l*. A convergence test such as that employed by Sakuragi *et al.* [Sak87] might be useful in determining the appropriate number and sizes of bins. The full (8-state) CC ^{60}Ni(^{6}Li,^{6}Li) calculations described here required 4 - 5 hours of CPU time on a VAX 11-780. A significant increase in the number of bins utilized would require a considerably more powerful computer.

Chapter 8

Coupled-Channel Born Approximation Analysis of the (d,^{6}Li) Reaction

Transition Amplitude for the ^{64}Zn(d,^{6}Li) Reaction

All observables for a reaction can be obtained from its transition amplitude. [Gle83] In the three-body, d-α-^{60}Ni system, the exact expression for the (d,^{6}Li) transition amplitude is :

$$T = \langle \Psi^{(-)}(\mathbf{R},\mathbf{r}) \mid V(\mathbf{R},\mathbf{r}) - U_d(\mathbf{R}_d) \mid \varphi(Zn; \mathbf{r}_\alpha)\, \chi_d^{(+)}(\mathbf{R}_d) \rangle \qquad (8.1)$$

Figure 7.1 illustrates the coordinate system employed in equation (8.1).

In the entrance channel, $\varphi(Zn; \mathbf{r}_\alpha)$ specifies the α-^{60}Ni component of the ^{64}Zn ground state. Relative motion between d and the ^{64}Zn center of mass is described by $\chi_d^+(\mathbf{R}_d)$, which is a solution to the Schrodinger equation in the presence of $U_d(\mathbf{R}_d)$ and with outgoing-wave boundary conditions. The interaction $U_d(\mathbf{R}_d)$ is arbitrary except that it must depend on $\mathbf{R}_d$ only.

The exact interaction between d and ^{64}Zn is given by :

$$V(\mathbf{R},\mathbf{r}) = V_{d\alpha}(\mathbf{r}) + V_{dNi}(\mathbf{R},\mathbf{r}) \qquad (8.2)$$

If $U_d(\mathbf{R}_d)$ is chosen so that $\chi_d^+(\mathbf{R}_d)$ reproduces d-^{64}Zn elastic scattering observables, $U_d(\mathbf{R}_d)$ will be quite similar to $V_{dNi}(\mathbf{R},\mathbf{r})$. It is then illuminating to rewrite equation (8.1) as :

$$T =$$

$$\langle \Psi^{(-)}(\mathbf{R},\mathbf{r}) \mid V_{d\alpha}(\mathbf{r}) + (V_{dNi}(\mathbf{R},\mathbf{r}) - U_d(\mathbf{R}_d)) \mid \varphi(Zn;\mathbf{r}_\alpha)\, \chi_d^{(+)}(\mathbf{R}_d) \rangle \qquad (8.3)$$

The interaction in parentheses is often small and is referred to as the remnant interaction. Unless stated otherwise, calculations presented in this thesis do not include the remnant interaction.

The $\Psi^{(-)}(\mathbf{R},\mathbf{r})$ in the bra of equations (8.1) and (8.3) is the exact solution of the full three-body, d-α-^{60}Ni problem. It must obey the boundary conditions :

$$\Psi^{(-)}(\mathbf{R},\mathbf{r}) \rightarrow \exp\left(\frac{i\,\mathbf{P}_0 \cdot \mathbf{R}}{\hbar}\right) \varphi^{1\sigma}(gs,\mathbf{r}) + \text{incoming waves} \qquad (8.4)$$

In the region of a detector, $\Psi^{(-)}(\mathbf{R},\mathbf{r})$ describes a ^{6}Li plane wave receding from ^{60}Ni, with ^{6}Li in its ground state. In the interaction region, $\Psi^{(-)}$ may also overlap substantially with other channels, such as those containing excited states of ^{6}Li.

In the coupled-channel Born approximation (CCBA), $\Psi^{(-)}(\mathbf{R},\mathbf{r})$ is expanded in terms of states of the ^{6}Li-^{60}Ni partition, as in equation (7.11), which is reproduced here as equation (8.5).

$$\Psi^{(-)}(\mathbf{R},\mathbf{r}) \approx \sum_\beta \chi_\beta^J(\mathbf{R})\varphi_\beta(\mathbf{r}) \qquad (8.5)$$

The sum in (8.5) includes the ^{6}Li ground and continuum states, $\varphi_\beta(\mathbf{r})$, each coupled to a wave function $\chi_\beta^J(\mathbf{R})$ that describes ^{6}Li-^{60}Ni scattering. The CCBA transition amplitude is therefore :

$$T^{CCBA} = \qquad (8.6)$$

$$\langle \sum_\beta \chi_\beta^J(\mathbf{R})\varphi_\beta(\mathbf{r}) \mid V_{d\alpha}(\mathbf{r}) + (V_{dNi}(\mathbf{R},\mathbf{r}) - U_d(\mathbf{R}_d)) \mid \varphi(Zn;\mathbf{r}_\alpha)\, \chi_d^{(+)}(\mathbf{R}_d) \rangle,$$

or, without the remnant interaction :

$$T^{CCBA} = \langle \sum_{\beta} \chi^{J}_{\beta}(\mathbf{R})\varphi_{\beta}(\mathbf{r}) \mid V_{d\alpha}(\mathbf{r}) \mid \varphi(Zn; \mathbf{r}_{\alpha})\, \chi^{(+)}_{d}(\mathbf{R}_{d}) \rangle. \qquad (8.7)$$

In the calculations presented below, the ^{6}Li-^{60}Ni wave functions $\chi^{J}_{\beta}(\mathbf{R})$ were calculated as specified by equation (7.15). The potentials $U_{\beta\beta'}(\mathbf{R})$ in (7.15) were generated using the CFM, equation (7.17), which utilized the effective interaction of equation (7.19). The TUNL-B deuteron optical model potentials were employed for $U_{d}(\mathbf{R}_{d})$, from which the d-^{64}Zn wave function $\chi^{(+)}_{d}(\mathbf{R}_{d})$ was calculated. The interaction $V_{d\alpha}(\mathbf{r})$ and the ground state wave function $\varphi^{1\sigma}(gs,\mathbf{r})$ (= $\varphi_{\beta=0}(\mathbf{r})$) were introduced in Chapter 1. In Chapter 7, we explicated calculations of the ^{6}Li continuum bin wave functions $\Phi_{\Omega i}(\mathbf{r})$ (= $\varphi_{\beta>0}(\mathbf{r})$). When included, the interaction $V_{dNi}(\mathbf{R},\mathbf{r})$ of equation (8.6) was approximated by the function $U_{d}(\mathbf{r}_{d})$, where $\mathbf{r}_{d}$ specifies the separation of d and ^{60}Ni. The target bound state wave function $\varphi(Zn; \mathbf{r}_{\alpha})$ is described below.

Wave Function for the ^{64}Zn Ground State

Both ^{60}Ni and α ground states have spins and parities of $I^{\pi} = 0^{+}$, so in the $I^{\pi} = 0^{+}$ ground state of ^{64}Zn the orbital angular momentum between ^{60}Ni and α must be zero. Hence, the angular and radial components of $\varphi(Zn; \mathbf{r}_{\alpha})$ can be separated as :

$$\varphi(Zn; \mathbf{r}_{\alpha}) = u_{0}(Zn,r_{\alpha})\, Y_{00}(\hat{r}_{\alpha}) \qquad (8.8)$$

The radial function $u_{0}(Zn,r_{\alpha})$ was generated using the Schrodinger equation. The Woods-Saxon-squared geometry of the α-^{60}Ni interaction was taken from Budzanowski et al. [Bud78] and is specified by the real component of equation (7.21) with r_{0} = 1.42 fm and a_{0} = 1.19 fm. The number of nodes in $u_{0}(Zn,r_{\alpha})$, six, was obtained using the harmonic oscillator energy-conservation relation :

$$2N + l = \sum_{i=1}^{4} (2n_{i} + l_{i}) \qquad (8.9)$$

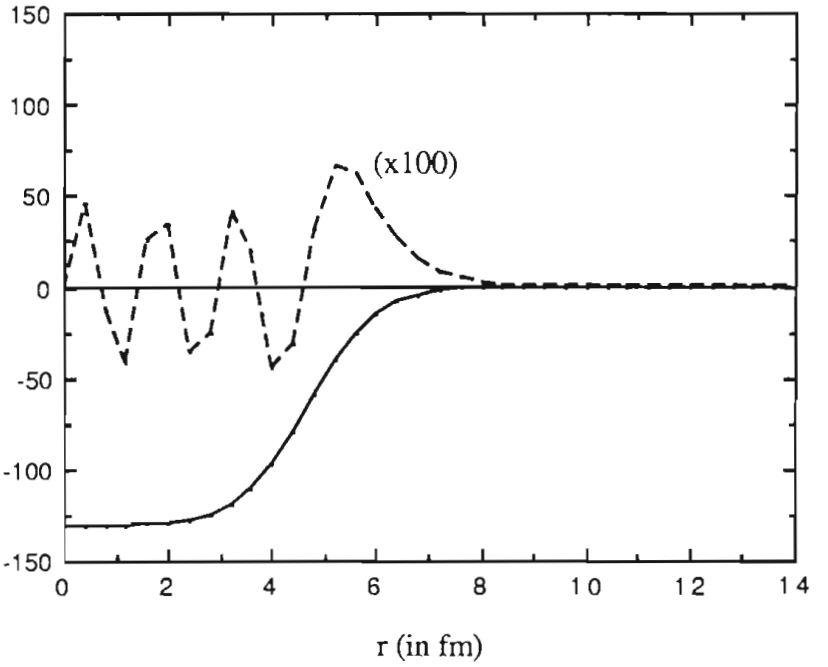

Figure 8.1 : The $^{64}Zn \rightarrow {}^{60}Ni + \alpha$ Wave Function. The dashed curve represents $r \cdot u_0(Zn;r_\alpha)$, the radial component of the ^{64}Zn wave function. The solid curve plots the α-^{60}Ni interaction (in MeV).

where n_i and l_i are the number of nodes and the orbital angular momentum of the shell model orbital of the i^{th} nucleon outside of a ^{60}Ni core. The depth of the α-^{60}Ni interaction was adjusted to reproduce the binding energy, 3.9556 MeV, of the ^{64}Zn ground state. The wave function $r \cdot u_0(Zn,r_\alpha)$ is shown in Figure 8.1.

Finite-Range, Coupled Channels Calculations Using FRESCO

In many analyses, the zero-range approximation is appropriate. For a pure $l = 0$ state of the projectile, this approximation replaces $\varphi_\beta(\mathbf{r})V_{d\alpha}(\mathbf{R},\mathbf{r})$ of equation (8.7) by the delta function $D_0\delta(\mathbf{r})$. Calculations that do not employ the zero-range approximation are termed finite-range. The zero-range approximation cannot be applied in calculations that include $l \neq 0$ states of the projectile. Our efforts to study $l \neq 0$ states of the ^{6}Li continuum as well as the D-wave admixture in the ^{6}Li ground state thus preclude use of the zero range approximation.

Several nuclear reaction codes calculate transition amplitudes in finite-range, but to our knowledge, only one code, FRESCO [Tho88], performs coupled-channels calculations in finite-range. Hence, FRESCO has been essential tool in our efforts to understand the consequences of coupling among the ground and excited states of ^{6}Li. FRESCO can also calculate the unbound wave functions $\Phi_{\Omega i}(\mathbf{r})$ of equation (7.11), and it allows for the folding model calculations of equation (7.17). Except for the calculation of Figure 1.1.1, all (d,^{6}Li) calculations presented in this thesis were performed using FRESCO.

Results of ^{64}Zn(d,^{6}Li)^{60}Ni(gs) DWBA and CCBA Calculations

Below, we attempt to illuminate the influence of α transfers forming the various states of ^{6}Li by discussing the results of calculations involving one or more of these states. Most of these calculations utilized the ^{6}Li-^{60}Ni interactions obtained from the CFM

described in Chapter 7. The significance of these CFM interactions is that, unlike phenomenological ^{6}Li-^{60}Ni interactions, the CFM interactions do not implicitly include the effects of couplings to ^{6}Li excited states. Use of these CFM interactions thus allows explicit control over the amount of channel coupling included in each calculation. These calculations indicate that ^{6}Li excited states strongly influence cross-sections and analyzing powers for the ^{64}Zn(d,^{6}Li) reaction. Furthermore, we employ these calculations to argue that the phenomenological potentials that implicitly include the influence of ^{6}Li continuum states on ^{6}Li elastic scattering do not adequately account for the effect of these states on the (d,^{6}Li) reaction. This result is significant because the standard practice in treating transfer reactions is to use optical potentials that reproduce elastic scattering observables. In Chapters 1 and 6, we argued that transfers forming the 3^{+} state might explain the predominantly negative character of the A_y data. Most notably, the calculations presented below indicate that these transfers make A_y predominantly positive, rather than negative. The contrast between measured and predicted values of A_y suggests a deficiency in the calculations but could also indicate that some other mechanism dominates the reaction.

Shown in Figure 8.2 are predicted cross-sections for 1-step α transfers forming the ^{6}Li ground state and each of the seven continuum bin states of Figure 7.2. These calculations do employ the phenomenological, global ^{6}Li optical model potentials of [Coo82b]. The calculation for the transfer forming the ($l = 0$) ^{6}Li ground state is identical to that of Figure 6.1. Calculations for the $l = 2$ states differ from those of Figure 6.1 only in that the continuum bin states, rather than the artificial, pure $l = 2$, ^{6}Li ground states, are employed here. This change dramatically lowers the $\Delta l = 2$ cross-sections. Cross-sections for 1-step α transfers forming the $l = 0$ and 1 continuum states are also low. Two factors are probably responsible for these low cross-sections. First, the $l = 2$, $I^{\pi} = 3^{+}$, 2^{+}, and 1^{+} states lie 2.2, 4.4, and 5.3 MeV above the ground state; bins for the $l =$ 0 and 1 continuum states are centered 3.9 MeV above the ground state. These internal

excitation energies imply lower kinetic energies for the ^{6}Li-^{60}Ni scattering. In particular, these kinetic energies are below the ^{6}Li-^{60}Ni Coulomb barrier energy. The Coulomb interaction forces ^{6}Li and ^{60}Ni apart and thus, according to the arguments of Chapter 6, strongly suppresses cross-sections for α transfers. Second, the finite lifetimes of the continuum states imply greater "time-averaged" distances between d and α. For instance, the $l = 0$ and 1 wave functions of Figure 7.3 indicate a much greater separation of d and α than does the ^{6}Li ground state wave function of Figure 1.2.1. This separation of d and α decreases the product $\varphi_{\beta}(r)V_{d\alpha}(r)$ in the transition amplitude. The effect may be mild for the narrow, $I^{\pi} = 3^{+}$ resonance; it should be more important for the $I^{\pi} = 2^{+}$ and 1^{+} resonances and most severe for the non-resonant $l = 0$ and 1 states. For example, the longer lifetime of the $I^{\pi} = 2^{+}$ state may explain why the cross-section for forming that state is greater than the cross-sections for forming the non-resonant $l = 0$ and 1 states.

The analyzing powers generated by the above calculations are not shown. For the Δl =2 transfers, these analyzing powers were very similar to those presented in Figure 6.1, indicating that the simple arguments of Chapter 6 apply to the continuum bin states.

The cross-sections plotted in Figure 8.2 suggest that α transfers forming the 3^{+} state of ^{6}Li may be quite important in the ^{64}Zn(d,^{6}Li) reaction at E_{lab} = 16.4 MeV. However, the influence of these transfers also depends on the strength of the coupling between the ^{6}Li ground and 3^{+} states. We now utilize the CCBA to calculate just how substantially α transfers forming the 3^{+} state contribute. Shown in Figure 8.3 are the results of several finite-range, CCBA, ^{64}Zn(d,^{6}Li)^{60}Ni(gs) calculations involving the ^{6}Li ground and 3^{+} states only. Interactions within the ^{6}Li-^{60}Ni partition were generated using the CFM of equation (7.17) and assuming (N_R, N_I) = (1.0, 1.0). The dotted, dashed, and solid curves correspond to calculations allowing for α transfers forming the 3^{+} state only, the ground state only, and both states, respectively. All calculations included channel coupling between the ground and 3^{+} states. (Figure 8.4) The cross-sections

plotted by the dotted and dashed curves are comparable in magnitude, indicating that strong interference effects should occur between these two channels. As one would expect from the discussion of Chapter 6, the pathway through the 3^+ state produces predominantly negative values of A_y, while the calculation allowing for α transfers forming the ^{6}Li ground state predicts that A_y oscillates symmetrically about zero. However, the interference between these pathways yields predominantly positive, rather than negative, VAPs. The positive values of A_{yy} and the negative values of A_{xx} for the dotted curve were also expected, given the results detailed in Chapter 6, though the magnitudes of these TAPs are significantly larger here. The solid curves perhaps suggest that the A_{yy} and A_{xx} data can be explained in terms of interference between α-transfers forming the ground and 3^+ states. Lower values of (N_R, N_I) decrease the channel coupling and thus lessen the influence of the 3^+ state. The various features of Figure 8.3, such as positive VAPs, remain, though they are somewhat less prominent.

Is explicit consideration of ^{6}Li excited states necessary? These states influence the (d,^{6}Li) reaction in two ways. First, as with ^{6}Li elastic scattering, coupling among these states strongly alters distortion effects within the ^{6}Li-^{60}Ni partition. Second, α transfers forming excited states of ^{6}Li provide alternate pathways into the ^{6}Li-^{60}Ni partition. The same effective interactions (e.g. optical potentials) developed to describe ^{6}Li elastic scattering may be employed to treat ^{6}Li-^{60}Ni distortion effects in (d,^{6}Li) reactions. The ^{6}Li excited states must be treated explicitly only if they are also important as alternate pathways into the ^{6}Li-^{60}Ni partition. Comparison of the dashed and solid curves of Figure 8.3 suggests that explicit treatment of the $I^\pi = 3^+$ resonance is needed. Distortion effects were handled identically by the two calculations associated with these curves. That is, both obtained interactions from the CFM and allowed for channel coupling between the ^{6}Li ground and 3^+ states. (Figure 8.4(a,c)) Including α-transfers forming the 3^+ state shifted the phase of $d\sigma/d\Omega$ and affected the analyzing powers dramatically. The full

(8-state) CCBA calculations of Figure 8.5 also indicate the importance of α transfers forming the 3^+ state. The dotted, dashed, and solid curves correspond to calculations that included α transfers forming the ^{6}Li ground state only, the ground and 3^+ states only, and all eight states of Figure 7.2. All three calculations handled distortion effects identically by allowing for channel coupling between all eight states. Interactions were generated from the CFM assuming $(N_R, N_I) = (1.0, 1.0)$. Explicit consideration of the 3^+ state yielded lower values of $d\sigma/d\Omega$ and produced predominantly positive VAPs. Comparisons of the dashed and solid curves indicate a more modest influence from transfers forming the other ^{6}Li continuum states.

Shown in Figures 8.6 are the results of finite-range, CCBA, ^{64}Zn(d,^{6}Li)^{60}Ni(gs) calculations that allowed for transfers forming each of the eight ^{6}Li states of Figure 7.2. The calculation corresponding to the solid curve employed $(N_R, N_I) = (1.0, 1.0)$, while the dotted and dashed curves were generated assuming the values (0.5, 0.7) and (0.7, 0.4), respectively. As discussed in Chapter 7, full CC calculations did not reproduce the ^{60}Ni(^{6}Li,^{6}Li) data using $(N_R, N_I) = (1.0, 1.0)$, though good fits were obtained with the values (0.5, 0.7) and (0.7, 0.4). In contrast, the (d,^{6}Li) $d\sigma/d\Omega$ data are best reproduced by calculations utilizing $(N_R, N_I) = (1.0, 1.0)$. Actually, full CC calculations with folding model renormalizations anywhere in the range $N_R = N_I =$ 0.8 - 1.0 generated results comparable to the solid curves of Figure 8.6. All three values of (N_R, N_I) yield positive VAPs.

The solid curves of Figure 8.7 are identical to those of Figures 8.5 and 8.6. The dashed curves were generated using the α particle optical potentials of Trombik et al. [Tro74] rather than those of Budzanowski. Otherwise, the calculations associated with the dashed and solid curves were identical. Trombik et al. assumed an interaction of the form :

$$U(r) = V_C(r) + (V + iW)\, f(r,r_0,a_0),$$

where $V_C(r)$ is the Coulomb interaction due to a uniformly charged sphere of radius 1.65 fm and $f(r,r_0,a_0)$ is defined by equation (5.1.4). They found that ^{58,60,62,64}Ni(α,α) data at E_{lab} = 18, 21, 24.1, and 27 MeV were well reproduced with the values V = 41.4 MeV, W = 8.4 MeV, r_0 = 1.65 fm and a_0 = 0.52. The real volume integral for this interaction, as calculated from the equation [McA86] :

$$\frac{JV}{4A} = \frac{\pi}{3} r_0^3 V \left[1 + \frac{\pi\, a_0}{A^{1/3} r_0}\right],$$

is 207 MeV•fm^3, in disagreement with the value of about 300 MeV•fm^3 established from analyses of nuclear rainbow scattering. [Chapter 7] Comparison of the dashed and solid curves in Figure 8.7 indicates a strong dependence on α particle optical potentials. In the surface region, R > 6 fm, the real folding model interactions generated using the α potentials of [Bud78] are nearly identical to those obtained assuming the potentials of [Tro74]. The imaginary interactions do not differ greatly. Hence, the differences between the solid and dashed curves of Figure 8.7 apparently result because the [Tro74] potentials are more shallow in the region R < 6 fm, or equivalently, because the [Tro74] potentials have a smaller volume integral. This effect is particularly interesting because only the surface region of the ^{6}Li-^{60}Ni interaction influences 1-step, DWBA calculations. Do these results suggest that CCBA analyses of (d,^{6}Li) reactions could be utilized to resolve discrete ambiguities in α particle optical potentials?

The calculation corresponding to the dotted curves of Figure 8.7 was identical to that for the solid curves except that the α-^{60}Ni interaction radius used for generating the ^{64}Zn $\rightarrow$ ^{60}Ni + α bound-state wave function was 10% smaller. (The well depth was readjusted to reproduce the ^{64}Zn binding energy.) The overall magnitude of the cross-

section is strongly affected by this radius (as one might expect from the simple model of Chapter 6). However, the influence on analyzing powers is very modest.

Several calculations were also performed using the remnant interaction of equation (8.3). These calculations indicated that results are not too sensitive to this interaction.

The contrast between the predominantly negative A_y data and the positive values of A_y obtained from CCBA calculations suggests several possibilities. If the calculations correctly and adequately model transfers forming the ^{6}Li ground and continuum states and the couplings between these states, the disagreement with the data implies that some other mechanism must dominate the reaction. For example, target excitation may be important. (The similarity between the ^{64}Zn(d,d') and ^{64}Zn(d,^{6}Li) A_y data is striking. (Figures 5.1.2 and 4.2.1)) Before such a conclusion can be definitive, several possible problems with the calculations must be considered.

The possibility of an error in the calculations can perhaps never be ruled out. However, in the plane wave approximation, FRESCO results have been checked against analytical (d,^{6}Li) calculations. [Tos88] Also, FRESCO CC calculations including the ^{6}Li ground and 3^+ states and using the CFM accurately reproduced measured values of A_y for ^{58}Ni(^{6}Li,^{6}Li) elastic scattering at E_{cm} = 18.1 MeV [Rus83] and 20.7 MeV [Wei76]; furthermore, these calculations agreed with similar CC calculations performed by [Nis84] and [Ohn84]. Predicted values of A_y for ^{6}Li elastic scattering are sensitive to, and therefore test, some, but not all, aspects of channel coupling. For example, predictions of A_y are strongly influenced by the magnitude of, but not the sign of, the interaction coupling the ground and 3^+ states. (In contrast, changing the sign of this interaction does change the predicted sign of Ay for the ^{64}Zn(d,^{6}Li) reaction.) Other than disagreement with the (d,^{6}Li) data, we have no reason to suspect an error in these calculations.

Another possibility is that the calculations do not adequately model the reaction. In Chapter 7, an insufficient number of continuum bins or an incorrect ^{6}Li-^{60}Ni effective interaction, arising from inappropriate d-^{60}Ni and α-^{60}Ni optical potentials, were adduced as possible reasons for the failure of full CC calculations to reproduce the ^{60}Ni(^{6}Li,^{6}Li) cross-section data. These possible deficiencies might also underlie the positive VAPs. Finally, a more microscopic treatment, employing nucleon-nucleon degrees of freedom in some components of the calculation, may be required. For instance, Cook has shown that the microscopic form factor for the ^{6}Li ground state is quite different from the cluster-model form factor $\varphi_{\beta}(\mathbf{r})V_{d\alpha}(\mathbf{r})$ of equation (8.7). [Coo84]

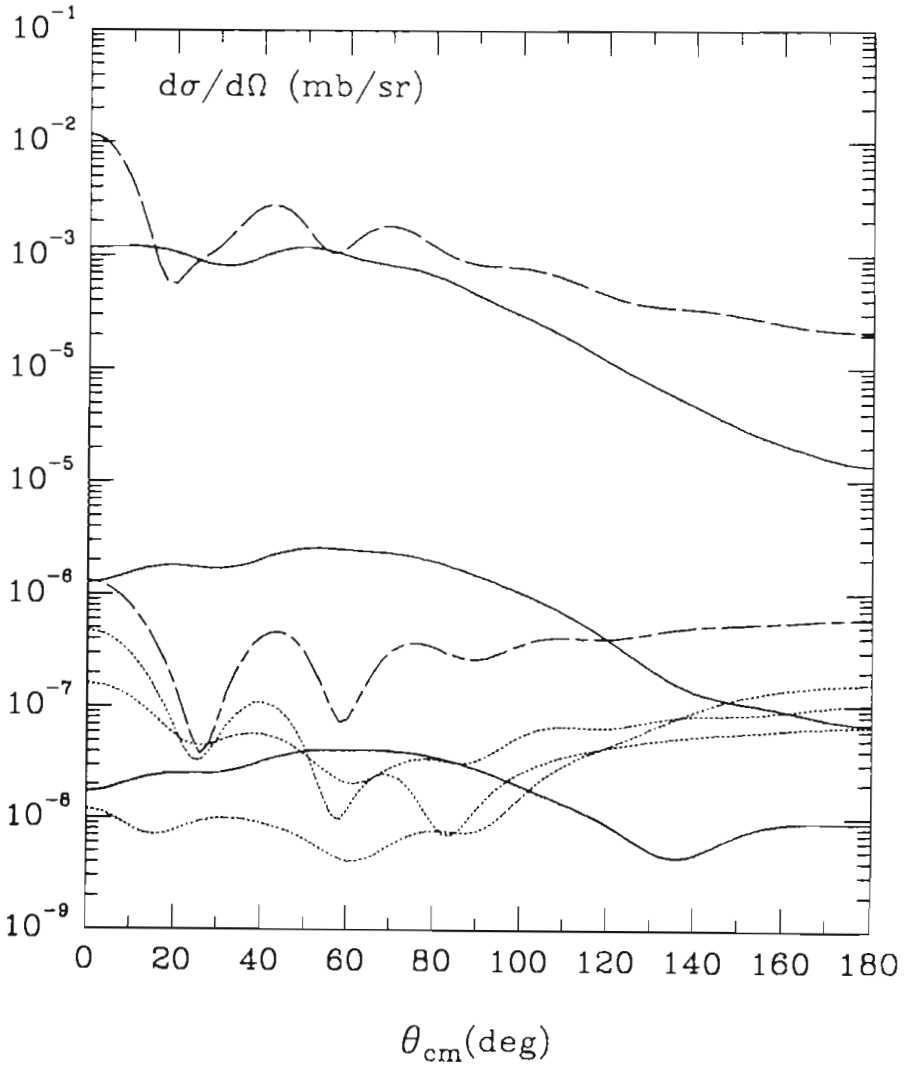

Figure 8.2 : Calculated Cross-sections for One-Step α Transfers Forming the Ground and the Seven Continuum Bin States of ^{6}Li. The long-dashed curve indicates differential cross-sections for formation of the ground state. The three solid curves represent cross-sections for forming of the $l = 2$ resonance states, with the transfer to the 3^+ state having the highest cross-section and that to the 1^+ state the lowest. Cross-sections for forming the $l = 0$ continuum state are specified by the long-dashed-short-dashed curve, and the dotted curves are for transfers forming the $l = 1$ continuum states.

Appendix A

Acquisition of the (d,^{6}Li) Excitation Functions

Excitation functions of cross-sections for the ^{36}Ar(d,^{6}Li), ^{40}Ca(d,^{6}Li), and ^{64}Zn(d,^{6}Li) reactions were measured in April of 1984, December of 1983, and April of 1984, respectively, to help determine the extent of compound nuclear contributions to these reactions. The acquisition of these data is detailed in this appendix. (Conclusions regarding compound nuclear effects are presented in Chapter 2.)

For each of the three excitation functions, a beam of unpolarized d^- ions was obtained from the TUNL direct-extraction negative-ion source (DENIS). These deuterons were accelerated by the TUNL FN tandem Van de Graaff electrostatic accelerator [New74], and the beam was then deflected 52° into a scattering chamber.

Acquisition of the ^{36}Ar(d,^{6}Li) Data

Approximately 600 nA of beam were delivered on target at incident laboratory energies ranging from 15.5 MeV to 17.3 MeV in 0.1 MeV steps. A cylindrical gas cell 2.54 cm in diameter and constructed from 0.00025 cm thick havar foil was placed in the center of the scattering chamber and loaded with 0.183 atmospheres of isotopically enriched ^{36}Ar. The ^{36}Ar gas pressure varied by less than 1% during the entire excitation function. To the right of the beam, three E-ΔE telescopes were placed at lab angles of 45°, 66.4°, and 82.9°, while to the left of the beam, a single detector was placed at 99.9°, and an E-ΔE telescope was placed at 125°.

Too much background was present for peaks to be extracted from the 99.9° spectra, and electronic problems precluded use of the 82.9° spectra. For the 45° and 66.4° telescopes, E signals from the ^{36}Ar(d,^{6}Li) reaction to the ground state of ^{32}S were too small to be detected at beam energies below 16.0 MeV and 15.7 MeV, respectively. The surviving data are presented in Table A-1 and in Figures 2.1(a-c).

Acquisition of the ^{40}Ca(d,^{6}Li) data

Cross-sections were measured at ten different beam energies between 16.5 MeV and 17.2 MeV using 600 nA to 1300 nA of d^- beam on target. A self-supporting, isotopically-enriched ^{40}Ca target was oriented so that its normal pointed 50° to the left of the beam. Telescopes were placed at laboratory angles of 45° and 64.1° to the left of the beam and 83.5°, 103.7°, and 125° to the right of the beam. Only cross-sections for the ^{40}Ca(d,^{6}Li) reaction forming the ^{36}Ar ground state could be extracted from the spectra. These cross-sections are listed in Table A-2.

Acquisition of the ^{64}Zn(d,^{6}Li) data

Between 500 and 800 nA of beam were placed on target, and the energy of this beam was varied from 15.5 MeV to 17.3 MeV in increments of 0.1 MeV. The target was produced as described in Chapter 3 and consisted of 291 $\mu g/cm^2$ of 99.67% isotopically pure ^{64}Zn backed by much thinner layers of carbon and aluminum. The target was oriented so that its normal pointed 45° to the right of the beam. Five E-ΔE telescopes were positioned to the right of the beam at laboratory angles of 45°, 66.8°, 86.5°, 106.6° and 125°.

Target thickness was determined by lowering the beam energy to 5 MeV and counting elastically scattered deuterons with the 45° and 66.8° telescopes. Hence, solid angles were identical for the excitation function and the target thickness measurement.

Cross-sections for 5-MeV deuteron elastic scattering at these angles were obtained from optical model calculations. (These calculations indicated that, at 45° and 66.8°, 5-MeV deuteron elastic scattering cross-sections are within 3% and 15% of purely Coulomb elastic scattering cross-sections, respectively.) Target thicknesses were calculated using these optical model cross-sections, and thicknesses of 288 $\mu g/cm^2$ and 295 $\mu g/cm^2$ were obtained from the 45° and 66.8° data, respectively.

No evidence of a $^{64}Zn(d,^6Li)$ peak was seen in the 125° telescope, though the ΔE detector was probably too thick for such a peak to have been detected. In the remaining four telescopes, cross-sections were extracted for the $^{64}Zn(d,^6Li)^{60}Ni(gs)$ reaction, and data for the $^{64}Zn(d,^6Li)$ reaction to the $I^\pi = 2^+$, 1.33 MeV state of ^{60}Ni was obtained 45° and 66.8°. These data presented in Tables A-3(a) and A-3(b).

Table A-1 : Measured Excitation Functions of Cross-sections (in mb/sr) for the $^{36}Ar(d,^{6}Li)^{32}S(gs)$ Reaction. All tabulated cross-sections are for the center-of-mass frame. At E_{lab} = 16.9 MeV, the three laboratory angles correspond to 50.1°, 73.0°, and 130.9° in the center-of-mass frame.

E_{lab} (MeV)	E_{cm} (MeV)	$d\sigma/d\Omega$ @ θ_{lab} = 45°	$d\sigma/d\Omega$ @ θ_{lab} = 66.4°	$d\sigma/d\Omega$ @ θ_{lab} = 125°
15.5	14.675	-------	-------	4.674e-4 9.014e-5
15.6	14.769	-------	-------	2.490e-3 1.656e-4
15.7	14.864	-------	8.350e-3 ± 2.781e-4	2.957e-3 1.770e-4
15.8	14.959	-------	7.521e-3 ± 2.629e-4	2.074e-3 1.556e-4
15.9	15.053	-------	7.621e-3 ± 2.502e-4	1.341e-3 1.267e-4
16.0	15.148	7.436e-3 ± 3.972e-4	7.600e-3 ± 2.480e-4	6.997e-4 1.007e-4
16.1	15.243	8.416e-3 ± 4.292e-4	7.694e-3 ± 2.469e-4	9.306e-4 1.146e-4
16.3	15.432	1.063e-2 ± 4.682e-4	7.552e-3 ± 2.470e-4	9.871e-4 1.154e-4
16.4	15.526	9.783e-3 ± 4.478e-4	7.465e-3 ± 2.408e-4	6.889e-4 1.009e-4
16.5	15.621	9.514e-3 ± 4.433e-4	6.207e-3 ± 2.208e-4	1.179e-3 1.064e-4
16.6	15.716	1.005e-2 ± 4.615e-4	5.695e-3 ± 2.133e-4	1.414e-3 1.340e-4

16.7	15.810	1.241e-2 ± 5.058e-4	5.750e-3 ± 2.153e-4	1.097e-3	1.133e-4
16.8	15.905	1.151e-2 ± 4.912e-4	6.491e-3 ± 2.302e-4	1.033e-3	1.267e-4
16.9	16.000	1.066e-2 ± 4.811e-4	7.786e-3 ± 2.494e-4	1.038e-3	1.304e-4
17.0	16.094	1.064e-2 ± 4.756e-4	7.334e-3 ± 2.435e-4	1.076e-3	1.197e-4
17.1	16.189	1.226e-2 ± 5.086e-4	8.148e-3 ± 2.567e-4	9.405e-4	1.164e-4
17.2	16.284	1.022e-2 ± 4.710e-4	7.208e-3 ± 2.389e-4	1.499e-3	1.382e-4

Figure A-2(a) : Measured Excitation Functions of Cross-sections (in mb/sr) for the $^{40}Ca(d,^{6}Li)^{36}Ar(gs)$ Reaction. The tabulated cross-sections are for the center-of-mass frame.

E_{lab}(MeV)	E_{cm}(MeV)	$d\sigma/d\Omega$ @ θ_{lab} = 45.0°	$d\sigma/d\Omega$ @ θ_{lab} = 64.1°	$d\sigma/d\Omega$ @ θ_{lab} = 83.5°
16.50	15.705	4.173e-3 ± 2.396e-4	-----	1.570e-3 ± 1.402e-4
16.60	15.800	3.633e-3 ± 1.865e-4	-----	1.824e-3 ± 1.248e-4
16.70	15.895	4.859e-3 ± 1.550e-4	3.817e-3 ± 1.912e-4	1.704e-3 ± 8.831e-5
16.80	15.990	3.775e-3 ± 1.279e-4	2.517e-3 ± 1.322e-4	1.793e-3 ± 8.006e-5
16.90	16.085	3.082e-3 ± 1.689e-4	1.227e-3 ± 1.382e-4	-----
16.95	16.133	3.037e-3 ± 1.652e-4	3.614e-3 ± 1.692e-4	1.196e-3 ± 1.005e-4
17.00	16.181	2.864e-3 ± 2.250e-4	3.577e-3 ± 1.455e-4	1.097e-3 ± 9.235e-5
17.05	16.228	3.280e-3 ± 1.705e-4	3.569e-3 ± 1.467e-4	1.290e-3 ± 1.003e-4
17.10	16.276	3.313e-3 ± 1.912e-4	3.721e-3 ± 1.868e-4	1.451e-3 ± 1.077e-4
17.20	16.371	3.435e-3 ± 2.105e-4	3.870e-3 ± 2.152e-4	1.188e-3 ± 1.089e-4

Figure A-2(b) : Continuation of Figure A-2(a).

E_{lab}(MeV)	E_{cm}(MeV)	$d\sigma/d\Omega$ @ θ_{lab} = 103.7°	$d\sigma/d\Omega$ @ θ_{lab} = 125.0°
16.50	15.705	-----	3.407e-4 ± 1.687e-4
16.60	15.800	5.773e-4 ± 9.526e-5	7.055e-4 ± 9.908e-5
16.70	15.895	1.056e-3 ± 7.896e-5	5.313e-4 ± 7.063e-5
16.80	15.990	1.535e-3 ± 7.985e-5	6.353e-4 ± 6.237e-5
16.90	16.085	1.326e-3 ± 1.186e-4	5.673e-4 ± 9.316e-5
16.95	16.133	1.398e-3 ± 9.970e-5	7.745e-4 ± 8.982e-5
17.00	16.181	9.793e-4 ± 8.629e-5	6.698e-4 ± 9.048e-5
17.05	16.228	8.435e-4 ± 9.525e-5	7.687e-4 ± 9.911e-5
17.10	16.276	8.256e-4 ± 9.575e-5	9.610e-4 ± 1.133e-4
17.20	16.371	8.173e-4 ± 1.013e-4	1.163e-3 ± 1.284e-4

Table A-3a : Measured Excitation Functions of Cross-sections (in mb/sr) for the $^{64}Zn(d,^{6}Li)^{60}Ni(gs)$ Reaction. All tabulated cross-sections are for the center-of-mass frame.

E_{lab}	E_{cm}	$d\sigma/d\Omega$ @ $\theta_{lab} = 45°$	$d\sigma/d\Omega$ @ $\theta_{lab} = 66.8°$	$d\sigma/d\Omega$ @ $\theta_{lab} = 86.5°$	$d\sigma/d\Omega$ @ $\theta_{lab} = 106.6°$
16.2	15.70	1.080e-3 ± 1.479e-4	4.786e-4 ± 7.323e-5	1.454e-4 ± 5.826e-5	1.259e-4 ± 7.556e-5
16.3	15.80	1.194e-3 ± 1.440e-4	4.092e-4 ± 7.601e-5	1.050e-4 ± 5.300e-5	2.188e-4 ± 8.668e-5
16.4	15.90	1.348e-3 ± 1.415e-4	5.579e-4 ± 7.180e-5	1.503e-4 ± 5.110e-5	1.924e-4 ± 7.168e-5
16.5	15.99	1.593e-3 ± 1.600e-4	3.813e-4 ± 6.655e-5	2.258e-4 ± 5.338e-5	7.825e-5 ± 6.731e-5
16.6	16.09	1.526e-3 ± 1.683e-4	4.432e-4 ± 7.182e-5	1.862e-4 ± 5.074e-5	7.855e-5 ± 6.367e-5
16.7	16.19	1.580e-3 ± 1.645e-4	4.225e-4 ± 6.711e-5	1.580e-4 ± 5.562e-5	1.060e-4 ± 7.032e-5
16.8	16.28	1.581e-3 ± 1.594e-4	5.441e-4 ± 7.303e-5	1.840e-4 ± 6.261e-5	2.014e-4 ± 8.385e-5
16.9	16.38	1.894e-3 ± 1.719e-4	5.101e-4 ± 7.542e-5	2.503e-4 ± 6.195e-5	1.271e-4 ± 7.110e-5
17.0	16.48	2.074e-3 ± 1.773e-4	5.636e-4 ± 7.743e-5	3.423e-4 ± 6.319e-5	3.129e-4 ± 8.026e-5
17.1	16.57	2.189e-3 ± 1.960e-4	4.608e-4 ± 7.549e-5	1.630e-4 ± 5.765e-5	2.120e-4 ± 7.877e-5
17.2	16.67	2.129e-3 ± 2.131e-4	5.374e-4 ± 8.899e-5	1.835e-4 ± 6.194e-5	2.966e-4 ± 8.534e-5
17.3	16.77	2.602e-3 ± 2.238e-4	4.399e-4 ± 9.332e-5	2.039e-4 ± 6.933e-5	2.968e-4 ± 9.481e-5

Table A-3b : Measured Excitation Functions of Cross-sections (in mb/sr) for the $^{64}Zn(d,^{6}Li)$ Reaction Forming the $I^{\pi} = 2^{+}$, 1.33 MeV First Excited State of ^{60}Ni. The tabulated cross-sections are for the center-of-mass frame.

E_{lab}	E_{cm}	$d\sigma/d\Omega$ @ 45°	$d\sigma/d\Omega$ @ 66.8°
16.2	15.70	4.612e-4 ± 1.273e-4	2.233e-4 ± 6.396e-5
16.3	15.80	2.238e-4 ± 1.154e-4	2.311e-4 ± 6.065e-5
16.4	15.90	5.610e-4 ± 1.185e-4	1.377e-4 ± 5.081e-5
16.5	15.99	4.920e-4 ± 1.250e-4	2.040e-4 ± 6.064e-5
16.6	16.09	5.166e-4 ± 1.362e-4	2.708e-4 ± 6.882e-5
16.7	16.19	4.976e-4 ± 1.275e-4	2.810e-4 ± 6.500e-5
16.8	16.28	5.868e-4 ± 1.354e-4	3.877e-4 ± 7.351e-5
16.9	16.38	4.183e-4 ± 1.352e-4	3.490e-4 ± 6.752e-5
17.0	16.48	5.518e-4 ± 1.396e-4	4.217e-4 ± 7.207e-5
17.1	16.57	4.359e-4 ± 1.415e-4	4.653e-4 ± 7.915e-5
17.2	16.67	6.396e-4 ± 1.708e-4	1.615e-4 ± 8.929e-5
17.3	16.77	5.087e-4 ± 1.829e-4	4.970e-4 ± 1.018e-4

Appendix B

Sources of the $^{64}Zn(\vec{d},d)$ Cross-section Normalization Error; Thicknesses of the ^{64}Zn Targets

As discussed in Chapter 5, our measured $^{64}Zn(d,d)$ cross-sections were almost certainly too large by a factor of about two. However, we believe that we know the correct normalization of these data from comparisons with elastic scattering cross-sections measured by [Chi74] and with cross-sections calculated assuming the global optical model potentials of [Dae80]. Thus, as far as the $^{64}Zn(\vec{d},d)$ data are concerned, uncovering the sources of this normalization error is desirable but probably not critical. Unfortunately, this normalization error casts doubts on the normalization of the measured $^{64}Zn(d,^{6}Li)$ cross-sections, because thicknesses of the targets used in the $^{64}Zn(\vec{d},^{6}Li)$ experiments were determined relative to the thickness of the target employed in the $^{64}Zn(\vec{d},d)$ experiment.

Below, possible sources of the $^{64}Zn(d,d)$ cross-section normalization error are discussed, and the determinations of the various target thicknesses are detailed. We conclude that the evidence, though far from definitive, suggests that an incorrect target thickness caused the $^{64}Zn(d,d)$ cross-section normalization error. In doing so, we decide the normalization of the $^{64}Zn(\vec{d},^{6}Li)$ cross-sections.

Possible Sources of the $^{64}Zn(d,d)$ Cross-section Normalization Error

An expression for the $^{64}Zn(d,d)$ cross-section in terms of various quantities measured during that experiment is :

$$\frac{d\sigma}{d\Omega} = \frac{160\ (L + R + U + D)\ \cos\theta_T\ A\ Z_B}{6.023\ \Omega\ TTHI\ BCIS\ BCI\ (4 - P_{zz}\ A_{zz})}, \qquad (B.1)$$

where L, R, U, and D are the number of counts, after corrections for dead times, in the left, right, up, and down detectors for a given spin direction and spin state, and P_{zz} is the tensor polarization of this beam state. The target angle was θ_T, the target mass number was A (= 64), the charge state of the beam was Z_B (= 1), the solid angle in milli-steradians of a single telescope was Ω, the target thickness in $\mu g/cm^2$ was TTHI, the number of pulses in thousands from the Brookhaven current integrator was BCI, and the scale in nanoamperes of this integrator was BCIS. Of these various terms, the only ones which could have conceivably been incorrect by a factor of two at all angles are the target thickness and the BCI. Underestimating the BCI by a factor of two could have produced the bogus cross-section normalization. For example, some of the current integration slits could have been disconnected from the integrator or grounded. However, no such malfunctions were discovered during or after the experiment. Hence, we are inclined to believe that the target thickness must have been in error.

Thickness of ZZ97

The thickness of ZZ97, the target used in the $^{64}Zn(\vec{d},d)$ experiment, was determined in two steps. First, its thickness relative to a target labelled JB1 was established by counting the elastic scattering of 16.4 MeV deuterons at a scattering angle of 40° for a fixed amount of beam current on both targets. This determination of relative thickness should have been highly accurate since the two measurements were taken within a few minutes of one another using identical slit settings to define the beam and using the same pair of symmetrically placed detectors and collimators. Also, at that beam energy and scattering angle the ^{64}Zn peak was well resolved from other peaks in the spectrum. The target ZZ97 was found to be thicker than JB1 by a factor of 1.16. This number is plausible because the two targets were produced during the same evaporation and were

located diagonally adjacent to one another on the same carbon foil slide. (The target production process is detailed in Chapter 3.) Secondly, in July 1986, the thickness of JB1 was measured using symmetrically placed detectors at 70°, 80°, and 90° and a beam of doubly-charged, 5-MeV α-particles. Optical model calculations indicate that the elastic scattering of doubly-charged α-particles at 5 MeV is purely Coulomb at all angles, thus allowing the target thickness to be determined from an equation similar to (B.1). Thicknesses of 158, 156, and 157 $\mu g/cm^2$ were obtained at the three angles, implying a thickness of 183 $\mu g/cm^2$ for ZZ97. This measurement appears to have been a good one. The energy, charge state of the beam, target angle, BCI scale, and solid angle were carefully checked during the experiment. Alpha particles scattered off C and O were well separated from those scattered off ^{64}Zn. Aluminum nuclei were also present, and the Al and ^{64}Zn peaks could not be distinguished. However, the Al layer was too thin, $\approx 4\ \mu g/cm^2$, to have significantly affected the measured thickness. A factor of two underestimation, if there were one, in the thickness of JB1 must have resulted from overestimating the collected beam charge. One possible mechanism concerns an in-house delay box through which the BCI pulses were often sent before they were counted by scalers. This delay box sometimes double-pulsed when the widths of its output pulses were set too narrow.

Thicknesses of Targets Utilized in the $^{64}Zn(\vec{d},^{6}Li)$ Experiments

The thickness of G44, the target used in the FEB86 $^{64}Zn(\vec{d},^{6}Li)$ run, was determined to be 1.05 times the thickness of ZZ97 by counting 16.4 MeV elastically scattered deuterons at 50°. As with the measurement of the relative thicknesses of JB1 and ZZ97, this determination should have been very reliable, and it is believable because G44 and ZZ97 were produced during the same evaporation and floated from adjacent positions on the slide. For the MAY86 $^{64}Zn(\vec{d},^{6}Li)$ run, the thickness of target X, relative to that of ZZ97, was determined by a somewhat more questionable procedure. In back-to-back

runs, the two targets were placed in a 16.4 MeV deuteron beam for a measured number of BCI pulses, and, in each of the six telescopes, the total number of counts per BCI in a region of the 2D spectrum dominated by ^{3}He- and α-particles were compared for the two targets. Hence, relative target thicknesses were determined from relative, combined (d,^{3}He) and (d,α) count rates. The thickness of target X was found to be 1.70 ± 0.07 times that of ZZ97, where 0.07 is the average deviation of the ratios obtained at different angles. The questionable aspect of this determination is that it included ^{3}He- and α-particles scattered off all nuclei in the targets, not just ^{64}Zn. Layers of Al and Cu were present in ZZ97 and X, respectively, but were too thin, 4.0 $\mu g/cm^2$ and 3 $\mu g/cm^2$, respectively, to have affected the count rate. Nearly equal ratios were obtained at six different angles, implying that if C and O contaminants were significant, they must have been present in proportion to the ^{64}Zn nuclei, since one would not expect ^{64}Zn(d,^{3}He) and ^{64}Zn(d,α) to have the same angular dependence as ^{12}C,^{16}O(d,^{3}He) and ^{12}C,^{16}O(d,α). Though dubious, the method appears to have worked, since the MAY86 (25°-75°) cross-sections are consistent with the FEB86 (30°-80°) cross-sections.

As discussed above, though the measured thickness of ZZ97 was 183 $\mu g/cm^2$, a thickness of 350 $\mu g/cm^2$ would give the correct ^{64}Zn(d,d) cross-section. Depending on which value of the ZZ97 thickness is accepted, these determinations yield thicknesses of either 192 $\mu g/cm^2$ or 368 $\mu g/cm^2$ for G44 and either 311 $\mu g/cm^2$ or 595 ug/cm^2 for X.

Some additional information is available regarding the thicknesses of G44 and X. The slide from which X was taken was weighed before and after the ^{64}Zn evaporation, and the average thickness evaporated onto the slide was found to be 692 $\mu g/cm^2$. This crude determination thus supports the higher target thickness figures. Secondly, (d,^{6}Li) cross-sections at 45° and 65°-70° taken in the FEB86 and MAY86 experiments were compared with the (d,^{6}Li) cross-sections at 45° and 66.8° measured in April, 1984. (Acquisition of the April, 1984 data is described in Appendix A.) Though the April, 1984

cross-sections suggest a thickness of ZZ97 somewhere between the two values considered here, they are significantly closer to the cross-sections obtained assuming the higher values of target thicknesses. (Table B.1)

angle	state	$d\sigma/d\Omega$ (1986)	$d\sigma/d\Omega$ (1984)	ratio
45°	gs	1.185 ± 0.024	1.47 ± 0.15	1.24 ± 0.13
45°	2+	0.376 ± 0.014	0.61 ± 0.13	1.63 ± 0.35
66.8°	gs	0.400 ± 0.017	0.43 ± 0.08	1.07 ± 0.21

Table B.1 : Comparison of the 1984 and 1986 $^{64}Zn(d,^{6}Li)^{60}Ni$ Cross-section Measurements. The laboratory frame cross-sections measured during the FEB86 and MAY86 $^{64}Zn(\vec{d},^{6}Li)$ experiments under the assumption that ZZ97 was 350 $\mu g/cm^2$ thick are compared with those determined during the excitation function measurements of April, 1984. The 1986 66.8° cross-section was obtained by an extrapolation of the values at 65° and 70°. All cross-sections are for E_d = 16.4 MeV except the 1984 66.8° point, which is for E_d = 16.3 MeV.

Summary

An error in the measured thickness of the target ZZ97 was identified as the most probable (and one of the few possible) sources of the normalization error in the $^{64}Zn(\vec{d},d)$ cross-section measurement. The measured thickness of ZZ97 was 183 $\mu g/cm^2$, whereas a thickness of 350 $\mu g/cm^2$ would give the correct $^{64}Zn(d,d)$ cross-section. The determination of the ZZ97 target thickness was described. Though the measurement appears to have been carefully performed and accurate, one possible source of error, a double-pulsing delay box, was noted. Determinations of the thicknesses of targets G44 and X, the two targets employed in the $^{64}Zn(\vec{d},^{6}Li)$ experiments, relative to the thickness of ZZ97 were detailed. Depending on the accepted value of the ZZ97 thickness, these

determinations yield thickness of either 192 $\mu g/cm^2$ or 368 $\mu g/cm^2$ for G44 and either 311 $\mu g/cm^2$ or 595 ug/cm^2 for X. The thicker values are supported by a crude thickness measurement performed while producing target X and by the consistency of the resulting FEB86 and MAY86 $^{64}Zn(d,^{6}Li)$ cross-sections with those obtained during the excitation function measurements of April, 1984. The $^{64}Zn(d,^{6}Li)$ cross-sections presented in this thesis assume the thicker values for the targets G44 and X.

Appendix C

Tables of Measured Angular Distributions

Compiled below are angular distributions of cross-sections and analyzing powers measured at TUNL for the ^{64}Zn(d,^{6}Li), ^{64}Zn(d,d), and ^{60}Ni(^{6}Li,^{6}Li) reactions. All tabulated cross-sections are for the center-of-mass frame.

Table C-1 : Measured Cross-sections and Analyzing Powers for the $^{64}Zn(d,^{6}Li)^{60}Ni(gs)$ Reaction at E_{lab} = 16.4 MeV. These data were measured in February and May of 1986.

Angle (cm)	Cross-section (mb/sr)		Ay		Ayy		Axx	
26.5	4.279e-4	1.584e-5	0.0359	0.0772	-0.1436	0.1068	-0.2658	0.0905
31.8	8.686e-4	2.995e-5	0.1099	0.0545	-0.4787	0.0938	0.0803	0.0801
37.0	1.205e-3	2.329e-5	-0.1144	0.0415	-0.2607	0.0586	0.1536	0.0400
42.3	1.504e-3	3.376e-5	-0.2037	0.0338	-0.2360	0.0567	0.1881	0.0518
47.5	1.090e-3	2.203e-5	-0.3775	0.0435	0.0231	0.0566	0.2542	0.0412
52.7	7.525e-4	2.433e-5	-0.5351	0.0518	0.1697	0.0765	0.1475	0.0777
57.9	4.425e-4	1.280e-5	-0.3971	0.0660	0.2281	0.0801	0.1770	0.0606
63.1	3.287e-4	1.458e-5	-0.0687	0.0690	-0.0844	0.1090	0.1766	0.1032
68.2	3.885e-4	1.630e-5	-------	-------	-------	-------	0.4640	0.0690
73.3	3.796e-4	1.323e-5	-0.3542	0.0535	-0.0433	0.0854	0.4381	0.0750
78.4	3.551e-4	1.127e-5	-0.5727	0.0699	0.2301	0.0853	0.2398	0.0662
83.5	3.119e-4	1.556e-5	-0.6178	0.0802	0.5791	0.1066	0.0898	0.1282

Table C-2 : Measured Cross-sections and Analyzing Powers for the $^{64}Zn(d,^{6}Li)^{60}Ni(2^{+},1.33\ MeV)$ Reaction at E_{lab} = 16.4 MeV.

These data were measured in February and May of 1986.

Angle (cm)	Cross-section (mb/sr)		Ay		Ayy		Axx	
26.6	6.799e-4	1.923e-5	-0.0522	0.0615	-0.0574	0.0822	-0.1869	0.0661
31.9	7.139e-4	2.653e-5	-0.1645	0.0539	-0.3101	0.0908	-0.0730	0.0928
37.1	5.635e-4	1.649e-5	-0.1431	0.0647	-0.0478	0.0855	0.0035	0.0642
42.4	4.951e-4	2.298e-5	-0.0399	0.0703	-0.1219	0.1134	-0.1154	0.1159
47.6	3.442e-4	1.287e-5	-0.1496	0.0831	-0.0187	0.1099	-0.2189	0.0874
52.8	3.536e-4	1.917e-5	-0.2045	0.0868	0.0622	0.1273	0.3679	0.1288
58.0	2.666e-4	1.038e-5	-0.2768	0.0893	-0.0059	0.1171	-0.0723	0.0860
63.2	2.166e-4	1.311e-5	-0.3226	0.1029	-0.3665	0.1632	0.0955	0.1384
68.4	1.664e-4	1.090e-5	--------	--------	--------	--------	0.1000	0.1200
73.5	1.223e-4	8.265e-6	-0.3559	0.1133	0.0979	0.1668	-0.0453	0.1614
78.6	9.130e-5	6.731e-6	-0.1793	0.1668	0.1380	0.2112	0.4807	0.1403
83.7	7.327e-5	9.583e-6	-0.2684	0.2094	0.3009	0.2873	0.5201	0.3138

Table C-3 : Measured Cross-sections and Analyzing Powers for $^{64}Zn(d,d)^{64}Zn$ Elastic Scattering at E_{lab} = 16.4 MeV.

These data were measured in February, 1986.

Angle (cm)	Cross-section (mb/sr)		A_y		A_{yy}		A_{xx}	
20.6	2.731e+3	7.078e+0	-0.0026	0.0043	0.0044	0.0060	-0.0195	0.0049
25.8	7.343e+2	1.660e+0	0.0062	0.0037	0.0024	0.0052	-0.0134	0.0042
30.9	3.607e+2	9.634e-1	-0.0094	0.0044	0.0083	0.0059	-0.0185	0.0052
36.0	2.443e+2	7.071e-1	-0.0264	0.0052	0.0214	0.0068	-0.0030	0.0052
41.2	1.215e+2	4.480e-1	-0.0399	0.0062	0.0315	0.0081	-0.0276	0.0072
46.3	4.657e+1	2.532e-1	-0.0349	0.0096	0.0429	0.0125	-0.0199	0.0099
51.4	2.284e+1	8.536e-2	-0.0432	0.0068	0.0000	0.0089	-0.0459	0.0080
56.5	1.938e+1	6.297e-2	0.0247	0.0058	-0.0123	0.0079	-0.0082	0.0068
61.6	1.570e+1	6.520e-2	0.0758	0.0077	-0.0238	0.0100	-0.0166	0.0087
66.6	1.034e+1	4.326e-2	0.0635	0.0075	0.0059	0.0100	-0.0109	0.0088
71.7	6.702e+0	3.540e-2	-0.0560	0.0096	0.0364	0.0126	-0.0219	0.0111
76.8	4.761e+0	2.532e-2	-0.2491	0.0114	0.1358	0.0126	-0.0052	0.0111
81.8	3.057e+0	1.906e-2	-0.2921	0.0138	0.2023	0.0153	-0.0847	0.0139
86.8	1.742e+0	7.302e-3	-0.0876	0.0084	0.1262	0.0106	-0.0947	0.0092
91.8	1.137e+0	8.041e-3	0.2905	0.0149	-0.1506	0.0185	0.0087	0.0149
96.8	1.077e+0	5.964e-3	0.2875	0.0114	-0.3102	0.0157	0.0606	0.0111

101.8	1.232e+0	7.146e-3	-0.0103	0.0105	-0.1078	0.0149	0.0540	0.0121
106.8	1.197e+0	5.264e-3	-0.2771	0.0099	0.1314	0.0110	-0.0067	0.0092
111.7	9.038e-1	3.532e-3	-0.4568	0.0102	0.3112	0.0095	-0.0610	0.0088
116.6	5.433e-1	3.621e-3	-0.5536	0.0176	0.5127	0.0173	-0.1100	0.0138
121.6	2.735e-1	1.963e-3	-0.3721	0.0146	0.4822	0.0162	-0.1087	0.0168
126.5	1.849e-1	2.071e-3	0.2391	0.0220	-0.3547	0.0331	0.0802	0.0215
131.4	2.396e-1	1.606e-3	0.3385	0.0128	-0.7738	0.0208	0.2363	0.0131
136.3	3.248e-1	2.422e-3	0.1149	0.0140	-0.5351	0.0238	0.2051	0.0137
141.2	3.639e-1	2.189e-3	-0.1036	0.0105	-0.1673	0.0152	0.0842	0.0122
146.0	3.540e-1	2.169e-3	-0.2810	0.0129	0.1624	0.0143	-0.0192	0.0130
150.9	3.074e-1	2.130e-3	-0.3461	0.0142	0.4889	0.0156	-0.1945	0.0160
155.8	2.409e-1	1.925e-3	-0.2668	0.0158	0.7171	0.0179	-0.3702	0.0199
160.6	1.908e-1	1.483e-3	0.0178	0.0142	0.7871	0.0180	-0.6177	0.0213
165.5	1.641e-1	1.360e-3	0.3991	0.0170	0.5924	0.0179	-0.7551	0.0238

Table C-4 : Measured Cross-sections and Analyzing Powers for $^{64}Zn(d,d')^{64}Zn(2^+, 0.998\ MeV)$ Scattering at E_{lab} = 16.4 MeV. These data were measured in February, 1986.

Angle (cm)	Cross-section (mb/sr)		A_y		A_{yy}		A_{xx}	
20.6	7.968	1.492e-1	-0.0365	0.0304	0.0218	0.0410	-0.0329	0.0365
25.8	8.449	1.280e-1	0.0252	0.0263	0.0253	0.0350	0.0247	0.0271
30.9	5.929	1.122e-1	0.0350	0.0304	0.0231	0.0408	-0.0906	0.0381
36.0	4.580	9.256e-2	-0.0071	0.0349	-0.0673	0.0481	0.0188	0.0361
46.3	3.998	7.351e-2	-0.1292	0.0327	0.0843	0.0418	-0.0383	0.0338
51.4	2.388	2.459e-2	-0.1340	0.0190	0.0425	0.0245	-0.0553	0.0219
56.5	1.195	1.448e-2	-0.0563	0.0220	0.1556	0.0283	-0.0643	0.0259
61.6	1.463	1.901e-2	0.0644	0.0237	0.0568	0.0308	0.0130	0.0270
66.6	1.918	1.811e-2	-0.0052	0.0165	-0.0301	0.0227	0.0051	0.0197
71.7	1.944	1.877e-2	-0.1271	0.0177	0.0267	0.0230	-0.0063	0.0202
76.8	1.434	1.349e-2	-0.2895	0.0182	0.0866	0.0220	-0.0539	0.0201
81.8	7.574e-1	9.100e-3	-0.4499	0.0244	0.2400	0.0281	-0.1156	0.0272
86.8	4.911e-1	3.871e-3	-0.2833	0.0161	0.3243	0.0188	-0.0085	0.0166
91.8	5.112e-1	5.325e-3	-0.0499	0.0194	0.1311	0.0249	-0.1244	0.0236
96.8	6.190e-1	4.379e-3	0.0091	0.0135	0.0168	0.0178	0.0000	0.0149
101.8	6.155e-1	5.000e-3	-0.1084	0.0150	-0.0548	0.0203	0.0580	0.0170
106.8	5.434e-1	3.474e-3	-0.2709	0.0132	-0.0013	0.0163	0.0532	0.0131

111.7	4.220e-1	2.347e-3	-0.4163	0.0122	0.1335	0.0135	0.0211	0.0122
116.6	3.213e-1	2.684e-3	-0.5121	0.0201	0.3314	0.0211	-0.0438	0.0171
121.6	2.503e-1	1.867e-3	-0.4038	0.0152	0.4052	0.0170	-0.1192	0.0175
126.5	2.027e-1	2.168e-3	-0.2628	0.0233	0.2767	0.0273	-0.1357	0.0227
131.4	1.964e-1	1.402e-3	-0.0786	0.0136	0.0910	0.0176	-0.0570	0.0161
136.3	1.966e-1	1.827e-3	0.0079	0.0191	0.0184	0.0252	-0.0875	0.0191
141.2	1.952e-1	1.600e-3	-0.0081	0.0143	0.0412	0.0195	-0.0321	0.0174
146.0	1.880e-1	1.574e-3	-0.0860	0.0153	0.0731	0.0199	0.0021	0.0176
150.9	1.856e-1	1.598e-3	-0.2143	0.0158	0.0337	0.0206	0.0910	0.0175
155.8	1.677e-1	1.529e-3	-0.3384	0.0179	0.0256	0.0218	0.1931	0.0179
160.6	1.526e-1	1.256e-3	-0.4095	0.0169	0.0946	0.0192	0.1581	0.0164
165.5	1.325e-1	1.184e-3	-0.4518	0.0188	0.2757	0.0201	0.0218	0.0188

Table C-5 : Measured Cross-sections for $^{60}Ni(^{6}Li,^{6}Li)^{60}Ni$ Elastic Scattering at E_{lab} = 14.8 MeV. The data were measured in April, 1987. Shown also are cross-sections divided by the Rutherford cross-section.

θ_{lab}	θ_{cm}	$d\sigma/d\Omega$ (mb/sr)	$\frac{d\sigma/d\Omega}{(d\sigma/d\Omega)_{Ruth}}$
20.2	22.2	3.691e+4 ± 2.213e+2	1.004 ± 0.0060
25.2	27.6	1.559e+4 ± 6.182e+1	0.999 ± 0.0039
30.2	33.1	7.749e+3 ± 4.947e+1	1.010 ± 0.0064
35.2	38.5	4.275e+3 ± 1.262e+1	0.999 ± 0.0029
40.2	43.9	2.589e+3 ± 1.120e+1	1.001 ± 0.0043
45.2	49.3	1.704e+3 ± 9.323e+0	1.021 ± 0.0055
50.2	54.6	1.168e+3 ± 7.409e+0	1.024 ± 0.0064
55.2	60.0	8.459e+2 ± 2.946e+0	1.047 ± 0.0036
60.2	65.2	5.988e+2 ± 5.284e+0	0.999 ± 0.0088
65.2	70.4	4.482e+2 ± 2.292e+0	0.979 ± 0.0050
70.2	75.6	3.323e+2 ± 2.641e+0	0.928 ± 0.0073
75.2	80.8	2.381e+2 ± 6.802e-1	0.831 ± 0.0023
80.2	85.9	1.804e+2 ± 5.947e-1	0.769 ± 0.0025
85.2	90.9	1.407e+2 ± 5.300e-1	0.718 ± 0.0027
90.2	95.9	1.081e+2 ± 4.675e-1	0.651 ± 0.0028
95.2	101.0	8.541e+1 ± 3.992e-1	0.599 ± 0.0028
100.2	105.9	6.740e+1 ± 3.654e-1	0.541 ± 0.0029
105.2	110.8	5.494e+1 ± 3.257e-1	0.499 ± 0.0029
110.2	115.6	4.413e+1 ± 3.008e-1	0.447 ± 0.0030

115.2	120.5	3.699e+1	±	2.660e-1	0.416	±	0.0029
120.2	125.2	3.082e+1	±	2.612e-1	0.379	±	0.0032
125.2	129.9	2.709e+1	±	2.312e-1	0.361	±	0.0030
130.2	134.6	2.259e+1	±	2.269e-1	0.324	±	0.0032
135.3	139.4	2.000e+1	±	4.178e-1	0.306	±	0.0064
140.3	144.0	1.743e+1	±	4.582e-1	0.282	±	0.0074
145.3	148.6	1.496e+1	±	3.656e-1	0.254	±	0.0062
150.2	153.0	1.430e+1	±	2.942e-1	0.253	±	0.0052
155.2	157.6	1.272e+1	±	2.786e-1	0.233	±	0.0051
160.2	162.1	1.227e+1	±	2.746e-1	0.231	±	0.0051
165.2	166.6	1.233e+1	±	2.760e-1	0.237	±	0.0053

Table C-6 : Measured Cross-sections for $^{60}Ni(^{6}Li,^{6}Li)^{60}Ni(2^{+}, 1.33\ MeV)$ Scattering at E_{lab} = 14.8 MeV. The data were measured in April, 1987.

θ_{lab}	θ_{cm}	$d\sigma/d\Omega$ (mb/sr)
40.3	44.1	5.524e+0 ± 6.960e-1
45.3	49.4	2.186e+0 ± 8.647e-1
50.0	54.4	2.685e+0 ± 4.902e-1
55.2	59.9	8.957e-1 ± 1.537e-1
60.0	65.0	1.139e+0 ± 2.115e-1
65.0	70.2	5.717e-1 ± 1.509e-1
70.0	75.4	6.826e-1 ± 1.866e-1
75.2	80.8	6.776e-1 ± 4.500e-2
80.2	85.9	5.509e-1 ± 4.394e-2
85.2	90.9	5.591e-1 ± 3.999e-2
90.2	95.9	5.993e-1 ± 3.971e-2
95.3	101.1	5.233e-1 ± 3.578e-2
100.2	105.9	5.663e-1 ± 4.073e-2
105.3	110.9	6.353e-1 ± 3.956e-2
110.2	115.6	4.507e-1 ± 4.060e-2
115.2	120.4	6.449e-1 ± 3.624e-2
120.2	125.2	5.760e-1 ± 3.942e-2
125.2	129.9	7.217e-1 ± 3.774e-2
130.2	134.6	6.559e-1 ± 4.205e-2
135.3	139.4	6.958e-1 ± 1.518e-1

145.8	148.6	6.782e-1 ± 1.517e-1
150.3	153.2	6.296e-1 ± 8.729e-2
155.3	157.7	6.227e-1 ± 8.721e-2
160.2	162.1	5.819e-1 ± 5.980e-2
165.2	166.6	6.445e-1 ± 6.311e-2

References

Ajz88 F. Ajzenberg-Selove, Nucl. Phys. **A490** (1988) 1.

Ama79 H. Amakawa, S. Yamaji, A. Mori, and K. Yazaki, Phys. Lett. **82B** (1979) 13.

Ana80 N. Anantaraman, H. W. Fulbright, and P. M. Stwertka, Phys. Rev. C**22** (1980) 501.

ARI01 The Arizona Carbon Foil Company, Tuscon, Arizona, 85711.

Bla52 J. M. Blatt and V. F. Weisskopf, Theoretical Nuclear Physics (1952), John Wiley and Sons, New York, p. 103.

Bud78 A. Budzanowski, H. Dabrowski, L. Freindl, K. Grotowski, S. Micek, R. Plaeta, A. Strzalkowski, M. Bosman, P. Leleux, P. Macq, J. P. Meulders, and C. Pirart, Phys. Rev. C**17** (1978) 951.

Chi74 J. D. Childs, W. W. Daehnick, and M. J. Spisak, Phys. Rev. C**10** (1974) 217.

Chu78 W. Chung, J. van Hienen, B. H. Wildenthal, and C. L. Bennett, Phys. Lett. **79B** (1978) 381.

Cle89 H. Clement, private communication.

Cle85 H. Clement, Deuteron Involving Reactions and Polarization Phenomena, edited by Y. Aoki and K. Yagi, World Scientific, Singapore (1985) p.104.

Cle74 T. B. Clegg, G. A. Bissinger, T. A. Trainor, Nucl. Instrum. and Methods **120** (1974) 445.

Coo84 J. Cook, Nucl. Phys. **A417** (1984) 477.

Coo83 J. Cook and K. W. Kemper, Phys. Lett. **123B** (1983) 5.

Coo82a J. Cook, K. W. Kemper, and M. F. Vineyard, Phys. Rev. **C26** (1982) 486.

Coo82b J. Cook, Nucl. Phys. **A388** (1982) 153.

Dae80 W. W. Daehnick et al., Phys. Rev. **C21** (1980) 2253.

Del72 R. M. DelVecchio and W. W Daehnick, Phys. Rev. **C6** (1972) 2095.

Ent86 R. Ent, H. P. Block, J. F. A. van Hienen, G. van der Steenhoven, J. F. J. van den Brand, J. W. A. den Herder, E. Jans, P. H. M. Keizer, L. Lapikas, E. N. M. Quint, P. K. A. de Witt Huberts, B. L. Berman, W. J. Briscoe, C. T. Christou, D. R. Lehman, B.E. Norum, and A. Saha, Phys. Rev. Let. **57** (1986) 2367.

Esk88 A. Eskandarian, D. R. Lehman, and W. C. Parke, Phys. Rev. **C38** (1988) 2341.

Fia73 S. Fiarman and W. E. Meyerhof, Nucl. Phys. **A206** (1973) 1.

Ful79 H. W. Fulbright, Ann. Rev. Nucl. Part. Sci. **29** (1979) 161.

Gam60 J. L. Gammel, B. J. Hill, and R. M. Thaler, Phys. Rev. **119** (1960) 267.

Gil65 Gilbert and Cameron, Canadian Journal of Physics **43** (1965) 1446.

Gri70 J. A. R. Griffith, M. Irshad, O. Karban, and S. Roman, Nucl. Phys. **A146** (1970) 193.

Gle83 N. K. Glendenning, Direct Nuclear Reactions (1983), Academic Press, New York.

Gol74 D. A. Goldberg, S. M. Smith, G. F. Burdzik, Phys. Rev. **C10** (1974) 1362.

Gom85 J. Gomez-Camacho, M. Lozano, and M. A. Nagarajan, Phys. Lett. **161B** (1985) 39.

Hae67 W. Haeberli, Ann. Rev. Nucl. Sci. **17** (1967) 373.

Has67 A. Hasegawa and S. Nagata, Prog. Theor. Phys. **38** (1967) 1188.

Jac79 W. W. Jacobs, E. J. Ludwig, J. E. Wilkerson, H. E. Conzett, P. Von Rossen, and R. M. Larimer, Bull. Am. Phys. Soc. **24** (1979) 839.

Jam75 F. James and M. Roos, Comp. Phys. Comm. **10** (1975) 343.

Jan80 J. Janecke, F. D. Becchetti, and D. Overway, Nucl. Phys. **A343** (1980) 161.

Jen83 B. Jenny, W. Gruebler, V. Konig, P. A. Schmelzbach, and C. Schweizer, Nucl. Phys. **A397** (1983) 61.

Kub72 K. -I. Kubo and M. Hirata, Nucl. Phys. **A187** (1972) 186.

Leh86 D. R. Lehman and W. C. Parke, Few Body Systems **1** (1986) 193.

Leh85 D. R. Lehman and W. C. Parke, Phys. Rev. **C31** (1985) 1920.

Leh82 D. R. Lehman and M. Rajan, Phys. Rev. **C25** (1982) 2743.

Leo87 W. R. Leo, Techniques for Nuclear and Particle Physics Experiments (1987), Springer-Verlag, New York.

Mer70 E. Merzbacher, Quantum Mechanics (1970), John Wiley and Sons, New York.

Mac78 M. H. MacFarlane and S. C. Pieper, Argonne National Laboratory report ANL-76-11 Rev. 1, unpublished; revised by R. P. Goddard, 1980, unpublished.

McA86 T. L. McAbee, Ph. D. dissertation, University of North Carolina, 1986, (unpublished), available from University Microfilms International, 300 N. Zeeb Rd., Ann Arbor, Michigan 48106.

McI67 L. C. McIntyre and W. Haeberli, Nucl. Phys. **A91** (1967) 382.

Mer85 A. C. Merchant and N. Rowley, Phys. Lett. **150B** (1985) 35.

New74 H. W. Newson, E. G. Bilpuch, F. O. Purser, J. R. Boyce, and T. B. Clegg, Nucl. Instrum. and Methods **122** (1974) 99.

Nis84 H. Nishioka, J. A. Tostevin, R. C. Johnson , and K. I. Kubo, Nucl. Phys. **A415** (1984) 230.

Nis83 H. Nishioka, J. A. Tostevin, and R. C. Johnson, Phys. Lett. **124B** (1983) 17.

Nis82 H. Nishioka, R. C. Johnson, T. A. Tostevin, and K. -I. Kubo, Phys. Rev. Lett. **48** (1982) 1795.

Ohl73 G. G. Ohlsen and P. W. Keaton, Jr., Nucl. Inst. and Meth. **109** (1973) 41.

Ohn84 H. Ohnishi, M. Tanifuji, M. Kamimura, Y. Sakuragi, and M. Yahiro, Nucl. Phys. **A415** (1984) 271.

Ort83 EG&G Ortec : Radiation Detection, Measurement, and Analysis, 1983.

Pal84 G. Palla and W. Oelert, Phys. Rev. **C30** (1984) 1331.

Par84 W. C. Parke and D. R. Lehman, Phys. Rev **C29** (1984) 2319.

Pie85 D. Pierce, J. E. Bowsher, H. J. Karwowski, E. J. Ludwig, T. C. Spencer, private communication.

RAI75 M. RAI, D. R. Lehman, and A. Ghovanlou, Phys. Lett. **59B** (1975) 327.

Roo77 P. G. Roos, N. S. Chant, A. A. Crowley, D. A. Goldberg, H. D. Holmgren, and R. Woody III, Phys. Rev. **C15** (1977) 69.

Rus83 K. Rusek, Z. Moroz, R. Caplar, P. Egelhof, K. -H. Mobius, E. Steffens, I. Koenig, A. Weller, and D. Fick, Nucl. Phys. **A407** (1983) 208.

Sak87 Y. Sakuragi, Phys. Rev. **C35** (1987) 2161.

Sak86 Y. Sakuragi, M. Yahiro, and M. Kamimura, Prog. Theor. Phys. Suppl. **89** (1986) 136.

Sat83 G. R. Satchler, Direct Nuclear Reactions (1983), Oxford University Press, New York.

Sat79 G. R. Satchler, Phys. Lett. **83B** (1979) 284.

Sat78 G. R. Satchler and W. G. Love, Phys Lett. **76B** (1978) 23.

Sat60 G. R. Satchler, Nucl. Phys. **21** (1960) 116.

Sch72 P. A. Schmelzbach, W. Gruebler, V. Konig, and P. Marmier, Nucl. Phys. **A184** (1972) 193.

Tag87 Y. Tagishi, Y. Aoki, M. Kurokawa, T. Murayama, T. Sakai, M. Takei, M. Tomizawa, and K. Yagi, Phys. Rev. **C35** (1987) 1153.

Tag85 Y. Tagishi, Deuteron Involving Reactions and Polarization Phenomena, edited by Y. Aoki and K. Yagi, World Scientific, Singapore (1985) p.79.

Tho88 I. J. Thompson, Computer Physics Reports **7** (1988) 167.

Tho81 I. J. Thompson and M. A. Nagarajan, Phys. Lett. **106B** (1981) 163.

Ton80 S. A. Tonsfeldt, Ph. D. dissertation, University of North Carolina, 1980, (unpublished), available from University Microfilms International, 300 N. Zeeb Rd., Ann Arbor, Michigan 48106.

Tos88 J. A. Tostevin, private communication.

Tos87 J. A. Tostevin, private communication.

Tos86 J. A. Tostevin, private communication.

Tro74 W. Trombik, K. A. Eberhard, G. Hinderer, H. H. Rossner, A. Weidinger, and J. S. Eck, Phys. Rev. **C9** (1974) 1813.

Ume84 K. Umeda, T. Yamaya, T. Suehiro, K. Takimoto, R. Wada, E. Takada, S. Shimoura, A. Sakaguchi, S. Murakami, M. Fukada, and Y. Okuma, Nucl. Phys. **A429** (1984) 88.

Var86 R. L. Varner, Ph. D. dissertation, University of North Carolina, 1986, (unpublished), available from University Microfilms International, 300 N. Zeeb Rd., Ann Arbor, Michigan 48106.

Ver87 S. P. Van Verst, D. P. Sanderson, K. W. Kemper, D. Shapira, R. L. Varner, and B. Shivakumar, Phys. Rev. **C36** (1987) 1865.

Wei76 W. Weiss, P. Ebelhof, K. D. Hildenbrand, D. Kassen, M. Makowska-Rzeszuto, D. Fick, H. Ebinghaus, E. Steffens, H. Amakawa, and K. -I. Kubo, Phys. Lett. **61B** (1976) 237.

Yam85a T. Yamaya, J. I. Hirota, K. Takimoto, S. Shimoura, A. Sakaguchi, S. Kubono, M. Sugitani, S. Kato, T. Suehiro, and M. Fukada, in Proceedings of the Sixth International Symposium on Polarization Phenomena in Nuclear Physics, Osaka, 1985, edited by M. Kondo, S. Kobayashi, M. Tanifuji, T. Yamazaki, K. -I. Kubo, and N. Onishi, J. Phys. Soc. Jpn. Suppl. **55** (1986) 730.

Yam85b T. Yamaya, T. Suehiro, S. Kato, J. I. Hirota, K. Takimoto, S. Shimoura, A. Sakaguchi, S. Kubono, M. Sugitani, and M. Fukada, in Proceedings of the Sixth International Symposium on Polarization Phenomena in Nuclear Physics, Osaka, 1985, edited by M. Kondo, S. Kobayashi, M. Tanifuji, T. Yamazaki, K. -I. Kubo, and N. Onishi, J. Phys. Soc. Jpn. Suppl. **55** (1986) 732.